KAUNAS UNIVERSITY OF TECHNOLOGY

MANTAS VAITIEKŪNAS

DEVELOPMENT AND INVESTIGATION OF THE METHOD FOR THE FACIAL BONES SEGMENTATION IN COMPUTED TOMOGRAPHY DATASETS

Doctoral dissertation
Technological Sciences, Electrical and Electronics Engineering (T 001)

2021, Kaunas

This doctoral dissertation was prepared at Kaunas University of Technology, Biomedical Engineering Institute during the period of 2015–2021.

Scientific Supervisor:

Assoc. Prof. dr. Darius JEGELEVIČIUS (Kaunas University of Technology, Technological Sciences, Electrical and Electronics Engineering – T 001).

Doctoral dissertation has been published in:
http://ktu.edu

Editor:

Armandas Rumšas (Publishing Office “Technologija”)

KAUNO TECHNOLOGIJOS UNIVERSITETAS

MANTAS VAITIEKŪNAS

VEIDO KAULŲ SEGMENTAVIMO KOMPIUTERINĖS TOMOGRAFIJOS DUOMENŲ RINKINIUOSE METODO SUKŪRIMAS IR TYRIMAS

Daktaro disertacija
Technologijos mokslai, elektros ir elektronikos inžinerija (T 001)

2021, Kaunas

Disertacija rengta 2015–2021 metais Kauno technologijos universiteto Biomedicininės inžinerijos institute.

Mokslinis vadovas:

doc. dr. Darius JEGELEVIČIUS (Kauno technologijos universitetas, technologijos mokslai, elektros ir elektronikos inžinerija – T 001).

Interneto svetainės, kurioje skelbiama disertacija, adresas:
http://ktu.edu

Redagavo:

Armandas Rumšas (leidykla „Technologija“)

Contents

List of terms and abbreviations

1D – One dimensional
2D – Two dimensional
3D – Three dimensional
AAPM – American Association of Physicists in Medicine
ALARA – As low as reasonably achievable
AMFPI – Active matrix flat panel imager
ASD – Average symmetric surface distance
BMD – Bone material density
CBCT – Cone beam computed tomography
CNN – Convolutional neural network
CoP – Coronal plane
CT – Computed tomography
DFT – Discrete Fourier transform
DICOM – Digital imaging and communications in medicine
DQE – Detective quantum efficiency
DSC – Dice similarity coefficient
EBM – Electron beam melting
ESF – Edge spread function
FA – Facial asymmetry
FBP – Filtered back projection
FDK – Feldkamp, Davis and Kress
FH – Frankfort plane
FOV – Field of view
FPI – Flat panel imager
FT – Fourier transform
FWHM – Full width at half maximum height
GMM – Gaussian mixture model
HCA – Histogram cluster analysis
HD – Hausdorff distance
HMH – Half maximum height
HU – Hounsfield unit
ICC – Intraclass correlation coefficient
IEC – International Electrotechnical Commission
LSF – Line spread function
MAP – Maximum a posteriori probability
MRI – Magnetic resonance imaging
MSD – Mean surface distance
MSP – Midsagittal plane
MSSD – Maximum symmetric surface distance
MTF – Modulation transfer function
NIST – National Institute of Standards and Technology
NPS – Noise power spectrum
PCA – Principal component analysis

PSF – Point spread function
RMS – Root mean square
RMSD – Root mean square symmetric surface distance
ROI – Region of interest
SLM – Selective laser melting
SLS – Selective laser sintering
SNR – Signal noise ratio
SSM – Statistical shape model
STL – Stereolithography
TFT – Thin film transistor
TMJ – Temporomandibular joint
VOE – Volumetric overlap error
VSP – Virtual surgical plan

ACKNOWLEDGMENTS

I would like to express my deep and sincere gratitude to my supervisor dr. Darius Jegelevičius for guiding my research. I am extremely grateful to medical doctor Simonas Grybauskas for his participation, guidance, support and help in writing and improving scientific papers and the generation of new scientific ideas. I would also like to thank dr. Andrius Sakalauskas for his active support and participation in co-authoring scientific papers.

My special gratitude is dedicated to my wife, Justina Geltytė, for her support, care and motivation have deeply inspired me. Also, I am grateful to my parents and sister for their support and understanding.

INTRODUCTION

Relevance of the Research

Computer-aided three dimensional (3D) processing of medical images is becoming an important way to reduce the time of pathology diagnosis, to confirm an accurate treatment plan, or to evaluate the postoperative follow-up (1). 3D segmentation is one of the most important steps in medical image processing (2). This is important in many different disciplines of medicine (3 – 5). With the increasing amount of medical data through the use of various imaging modalities (X-ray, magnetic resonance imaging (MRI), nuclear medicine, ultrasound), the time to segment selected volume of an anatomical region should be reduced. There are a variety of different software packages that can segment selected anatomical regions. However, segmentation is usually based on manual segmentation, where the final result depends on the experience of the user. For this reason, time and experience are the most important factors affecting the quality of segmentation (6, 7). The same reason is relevant in dentistry, especially, in oral and maxillofacial surgery, orthognathic surgery and orthodontics, where the accuracy of facial bones segmentation is important to ensure the accurate diagnosis of facial asymmetry (8), to prepare an accurate virtual surgical plan (VSP) (9), or to successfully follow the patient's condition during (10) or after treatment (11). In the last decade, Cone Beam Computed Tomography (CBCT) has become the most popular imaging modality due to its lower radiation dose and shorter acquisition time compared to conventional multislice CT. However, the images of CBCT are usually noisy and have beam hardening artefacts. The technical parameters of CBCT also affect the ability to correctly display Hounsfield units (HU) of head tissues (immediately after surgery when soft tissue edema is present) in contrast to the conventional CT (12, 13). These disadvantages also affect the image quality and the accuracy of bone segmentation (14). For these reasons, 3D VSP and evaluation of postoperative follow-up must be performed by using segmentation by highly experienced surgeons.

Unfortunately, currently, there are no accurate and reliable methods to perform segmentation automatically, rapidly, and accurately that can be applied in clinical practice. Wang *et al*. published three studies dedicated to fully automated bone segmentation using CBCT images (6, 15, 16). In the studies of 2013 (6) and 2014 (15), the principle of the automatic method was patch-based sparse representation. A patient-specific atlas (probability map) with a sparse label fusion strategy from the conventional CT atlases was used as a first estimation. Then, a convex segmentation framework was used to obtain the final result. The presented method resulted in accurate segmentation, but the main limitation of this method was the computational time (about 5 h (15)). In addition, the variety of CBCT datasets (patients with metallic implants, metallic plates, and various facial asymmetries) in their studies was low. Data collection from CT, with the objection to obtain more variety of atlases, is complicated in terms of bioethics requirements. In a study from 2016 (16), the same authors also proposed a new automatic method that used the random forest.

The multiclass classifier was used to create probability maps for each region of interest (the mandible, the maxilla, and the background). The results of the method were almost the same as in the previous study (15), but they also suffered from some similar limitations: the limited amount of CBCT data and also the relatively high computational time of segmentation (20 min). Minnema *et al*., 2018 (17) proposed a fully automatic method based on the convolutional neural network (CNN). The fully automatic CNN was able to accurately segment the skull. However, the efficiency of the method was evaluated only with CT datasets which are much less noisy compared to CBCT datasets. The variety of segmented anatomical regions could also be increased. Gollmer *et al*., 2012 presented a fully automatic method for mandible segmentation. In this research, segmentation was based on the idea of using the statistical shape model (SSM). The method showed accurate results, however, like the previous authors, the researchers also tested the algorithm with only six CBCT datasets (18). Fan *et al*., 2019 (19) proposed an automatic method for mandible segmentation. In their study, the marker-based watershed transform method was used. The authors performed accurate and sufficiently fast (12–14 min per dataset) segmentation on 20 CBCT datasets. Segmentation errors were obtained mainly in the three basic regions – around the wisdom teeth, condyles and dental enamel. The reasons for the segmentation errors were the different (greater) or equal intensity of the selected basic markers (the mandible and the background). Performing manual processing in these regions was recommended. Eijnatten *et al*., 2018 (20) performed a literature review of different bone segmentation methods. The authors found that global thresholding is the most commonly used method for bone segmentation. However, a limitation of this method is that it requires manual post-processing.

Scientific-technological questions

The scientific-technological questions that are being resolved in this thesis are:

How can segmentation of facial bones be performed independently of the operator's influence on the segmentation result?

How can automatic segmentation of facial bones be as accurate as the one performed by an experienced operator and be performed within a significantly lower amount of time and without the use of large computer computing resources?

Working Hypothesis

It is possible to perform automatic segmentation of facial bones independently of the operator's influence and the variability of the segmentation result.

It is possible to apply automatic segmentation in order to reduce the time required to prepare a VSP and evaluate the condition of the facial bones.

Research Object

The research is based on the development and investigation of the methods for automatic segmentation of facial bones in CBCT datasets (pre- and post-operative) in accordance with the preparation of 3D VSP and monitoring of facial bones during the treatment.

The Aim of the Research

To develop and investigate the automatic method for facial bones segmentation in cone beam computed tomography datasets (CBCT).

The Objectives of the Research

1. To investigate the distribution of volumetric elements (voxels) in the preoperative and postoperative CBCT datasets by Hounsfield units (HU).
2. To develop an automatic method to perform the segmentation of facial bones in CBCT dataset.
3. To investigate the influence of the 3D sliding window on the segmentation results.
4. To investigate and evaluate the efficiency of the proposed automatic method for facial bones segmentation by using clinical CBCT datasets.

Scientific Novelty

In this doctoral thesis, an automatic method for facial bones segmentation in the CBCT dataset was developed. The segmentation of facial bones is automated by using locally assessed distribution of voxel intensities. Three basic elements are used to implement the automatic segmentation: a 3D sliding window, a histogram filter, and thresholding based on Otsu's method. The 3D window allows finding optimal thresholds based on Otsu's method in the local volumes of the analyzed CBCT dataset. Accordingly, the influence of the operator on the result of facial bones segmentation is reduced. Fast and efficient segmentation of facial bones is achieved by using CBCT datasets with different quality – obtained before orthognathic surgery and one week after orthognathic surgery, when the patient's soft tissue is most swollen.

Practical value of the work

- The developed automatic method could serve as a tool for various software products to perform facial bones segmentation.
- It could also be used for inexperienced operators (doctors, medical engineers) automatically to obtain bone segments for performing VSP or assessing bone changes after surgery.

- The automatic method for facial bones segmentation reduces the time to perform the segmentation. The method does not require access to a computer with high computing power.

The statements presented for defense

1. Local thresholding can be used to find optimal thresholds when analyzing CBTC datasets. Segmentation becomes more objective and independent of the operator's experience. Local thresholding is less time consuming compared to with manual or semi-automatic segmentation.
2. A fast and efficient method for the segmentation of facial bones from CBCT datasets has been developed. The volume differences between automatically segmented facial bones and the reference (segmented by an experienced surgeon) were statistically insignificant ($p > 0.05$).
3. The proposed facial bones segmentation method is superior to other automatic methods (Wang *et al*., 2016; Fan *et al*., 2019, van Eijnatten *et al*., 2017) found in the current scientific literature in terms of the segmentation speed and efficiency.

Approbation

In total, the results of the doctoral dissertation have been published in 2 publications: 2 papers have been published in foreign periodic journals referred in the Journals of the Master List of Thomson Reuters Web of Science (with the impact factor). The results were presented in 3 international scientific conferences held in Finland (Tampere) and in Lithuania (Vilnius, Kaunas).

Structure and contents of the dissertation

The dissertation consists of an introduction, four chapters, general conclusions, the list of references, and the list of publications of the author. The dissertation is organized as follows:

1. In the first chapter, the clinical significance of segmentation of facial bones is presented. The main applications (evaluation of facial asymmetry, preparation of a virtual surgical plan, fabrication of patient-specific surgical guides, and the further patient's follow-up) of facial bones segmentation were reviewed.
2. In the second chapter, a critical review was carried out in order to analyze the currently existing methods for the automatic segmentation of facial bones from CBCT datasets. The main problems of the reviewed methods were determined. The main factors affecting the quality of the CBCT dataset were also reviewed. The histograms of conventional multislice CT and CBCT datasets were analyzed based on the reviewed scientific literature.
3. In the third chapter, experimental investigation of the limitations of CBCT imaging and the evaluation of a reference scanning system were performed.

4. In the fourth chapter, the concept of the proposed automatic segmentation for facial bones from CBCT datasets was proposed. Optically scanned anatomical models (mandibles) were used to evaluate the influence of a 3D sliding window on the segmentation results.
5. In the fifth chapter, investigation of the proposed automatic method for facial bones segmentation was performed with clinical data (forty CBCT datasets were used in the research).
6. General conclusions are presented in the final chapter.

The overall volume of the dissertation is 95 pages, including 64 figures, 13 tables, 23 equations and 161 bibliographic references.

1 CLINICAL SIGNIFICANCE OF FACIAL BONES SEGMENTATION

1.1 Medical background

1.1.1 Anatomy of facial bones

The facial bones are composed of fourteen bones: Nasal {2}, Lacrimal {2}, Inferior nasal concha {2}, Maxilla {2}, Mandible {1}, Vomer {1}, Zygomatic {2}, Palatine {2} (Fig. 1.1).

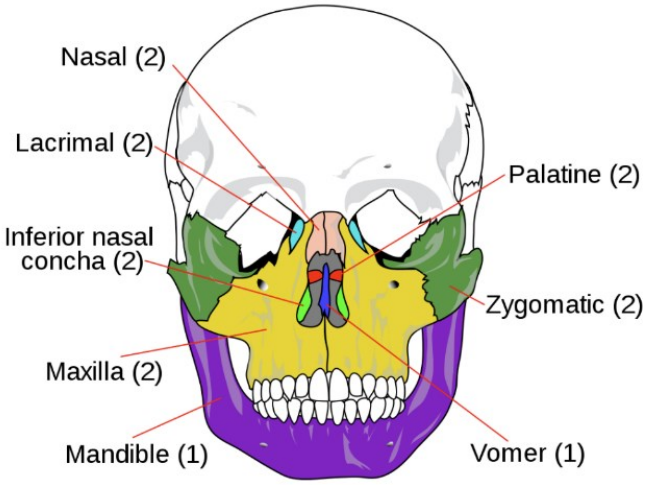

Fig. 1.1. Facial bones (21)

The facial bones form a skeleton which is a structure with bilateral symmetry as it consists of two mirror parts that are roughly symmetric about the vertical plane (22). However, the bilateral face is largely a theoretical concept that rarely exists in living organisms. Right and left differences occur everywhere in the nature where two bilateral parts present in an entity (23).

1.1.2 Facial asymmetries

The etiology of asymmetric face could be divided into three main categories (24 – 26):

1) Genetic or congenital malformations;
2) Environmental factors;
3) Functional deviations.

The most common genetic diseases affecting the asymmetric face are as follows (24 – 27):

- Cleft lip and palate;
- Tessier craniofacial cleft;

- Hemifacial macrosomia;
- Neurofibromatosis;
- Torticollis;
- Craniosynostosis;
- Vascular disorders;
- Osteochondroma;
- Others.

Environmental factors are associated with traumas, infections and habits. If these factors are not treated, then, some kind of diseases will be provoked, e.g., temporo mandibular joint ankylosis, facial trauma, fibrous dysplasia, facial tumors, etc. These diseases are very dangerous for growing children or old people. Damage or inflammation of the trigeminal nerve may lead to an asymmetric face. It is a cause of the loss of muscle function and tone. Injurious habits, such as sucking or chewing, can cause asymmetric face. Functional deviations are related with the size of the teeth and their position in the arches and the position of the dental arches in the upper and lower jaws. It causes the mandible shift during the opening and closing.

The asymmetric face has influence on the quality of life because it can cause physiological, psychological and emotional consequences (28, 29).

Physiological consequences

Performed studies (28 – 30) showed these main physiological consequences caused by facial asymmetries (FAs). People with FAs:

- can feel a headache more frequently than people without FAs;
- are slightly more likely to complain of an upset stomach and other gastrointestinal problems, it can cause nutrition disorders, such as obesity or malnutrition;
- can have trouble in concentrating, feel jittery (symptoms of depression, anxiety), these problems can lead to a physical illness, or to physical distress;
- have more problems with breathing, especially during the sleep – obstructive sleep apnea is the most common symptom which can lead to cardiovascular diseases;
- more often complain about muscle soreness, muscle cramps and muscle aches.

Psychological and emotional consequences

Psychological and emotional consequences are frequent for people with FAs (28, 29, 31, 32). People with FAs:

- have more frequent moods swings, are more depressed;

- can feel less attractive, more often have a lower self-esteem. They can be less sociable. The performed studies (31, 32) showed that female and male subjects with FA can have problems in the mate choices;
- can have higher levels of angriness, they can be more obsessive, far more impulsive and more emotional, less vigorous, less active, they may spend less time making important decisions.

The prevalence of the asymmetric face can range from 21% to 85% (33 – 37). This variation is affected by the sample characteristics of the norm or the kind of asymmetry, the methods and the tools of evaluation and the criteria of symmetry. The purpose of asymmetric face treatment is to help the patient to increase their self-esteem, to positively impact patient's psychological and emotional state of mind, and to eliminate physiological consequences. There are different but related to each other approaches to treatment in order to achieve the above mentioned goals.

1.2 Application of 3D facial bones segmentation

The task of 3D segmentation is to identify volume elements (voxels) which are the regions of interest (ROI) in the selected dataset (38). This is an important step in the current medical image analysis. Accurate segmentation is important in surgical planning and monitoring of the examined anatomical region (2, 39). This is very important and significant in oral and maxillofacial surgery, orthognathic surgery (40), orthodontics (41), in the area of additive manufacturing to fabricate patient-specific guides (42). 3D segmented facial bones can help more completely and precisely evaluate the condition of facial bones, prepare VSP, follow bones changes during or after treatment at different time points, construct drill guides, cutting guides and medical implants (43 – 45). Conventional 2D diagnostic radiographs (submento-vertex projections, posteroanterior radiography) have limitations, such as projection and identification errors in asymmetry diagnosis or performing an accurate treatment plan (Fig. 1.2) (46, 47).

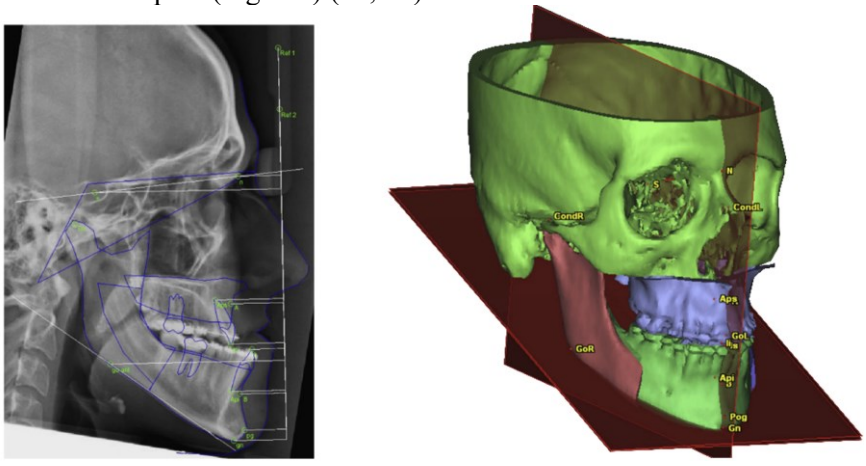

Fig. 1.2. 2D conventional cephalometric analysis (on the left side), 3D cephalometric analysis (on the right side) (47)

Cephalometric analysis on 3D model is denoted by obvious advantages. It can enable to more accurately evaluate the main distances between anatomical regions, can help to simulate the surgery before entering the operating room also evaluate the results after the surgery (47, 48).

1.2.1 Application of segmented facial bones for the evaluation of bone condition

Teeth are a part of the face, teeth are not a part of facial bones; however, the 3D segmentation of teeth is also important in the dental practice. Dental asymmetry can be caused by such local factors as early loss of the primary teeth, congenitally missing teeth, and such habits as thumb sucking. Lack of exactness in genetic expression affects the teeth on the right and left sides, causing asymmetries in mesio-distal crown diameters (24). The 3D segmentation of teeth is needed to determine the targeted orthodontic treatment planning and simulation, oral and maxillofacial surgery, dental implants. There are two main technologies in order to acquire 3D teeth models: intraoral/extraoral (desktop) scanning, and 3D segmentation from the CT/CBCT dataset. Intraoral and extraoral technologies enable to obtain the surface geometry of anatomical regions. It is a conventional way; however, it cannot enable to provide information about the roots of teeth, or to evaluate the density of teeth (Fig. 1.3) (49, 50).

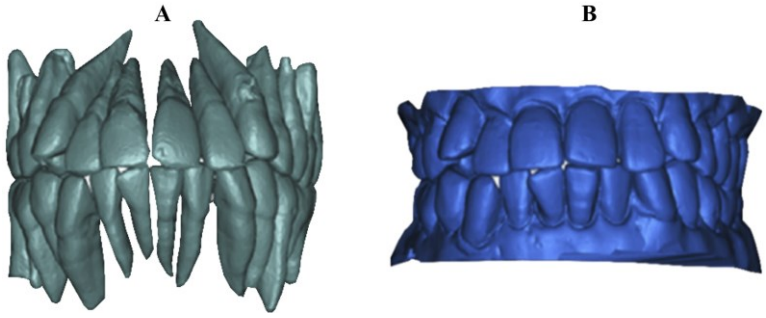

Fig. 1.3. 3D teeth models: **A** – segmented by the global thresholding method from CBCT dataset; **B** – scanned with intraoral scanner (50)

The quality of segmented teeth crowns from a CBCT dataset is lower comparing with intraoral/extraoral scanning. By combining the 3D segmentation technique with the intraoral/extraoral technique and applying the 3D superimposition method, the most accurate results can be achieved (50, 51). 3D positions of the whole teeth including their roots which were segmented from the CBCT dataset and dental crowns scanned with a consecutive intraoral scanner can be evaluated after superimposition (Fig. 1.4). This representation of teeth is useful in the clinical practice when teeth have metallic braces which can create metallic artefacts in the CBCT dataset. Due to this reason, accurate evaluation of an individual tooth or all the teeth can be performed.

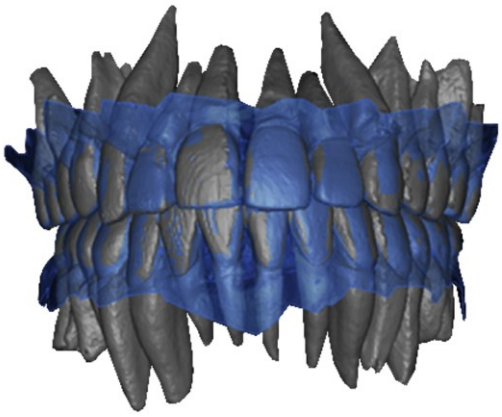

Fig. 1.4. Superimposed segmented teeth from CBCT dataset and scanned teeth by using intraoral scanner (50)

The surface of the crown is selected as the reference area for superimposition. The presented results are useful in orthodontic, implantology practices, oral and maxillofacial surgery. The positions and condition of the teeth roots can be evaluated very accurately by 3D segmentation results. The further treatment can be prescribed (50, 51).

3D segmentation of facial bones can help to evaluate skeletal asymmetry more precisely. Skeletal asymmetry is classified into three main classes: Class I, Class II and Class III (Fig. 1.5) (52).

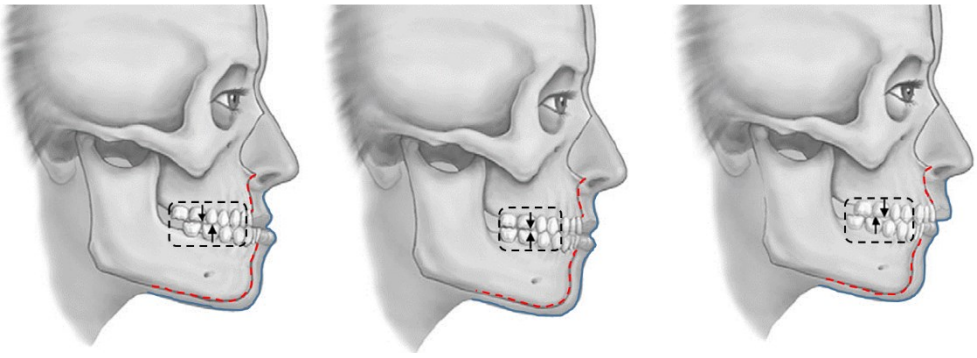

Fig. 1.5. Illustration of Class I, Class II and Class III facial skeletal profiles. Also, the relationship of molars is indicated (arrows) (52)

Class I: the maxillary base is in the normal anteroposterior relationship to the mandibular base. Class II: the mandibular base is posterior (caudal) to the maxillary base because of maxillary prognathism, mandibular retrognathism, or both. Class III: the mandibular base is anterior (ventral) to the maxillary base because of maxillary retrognathism, mandibular prognathism, or both (52). The main protocol in order to evaluate the position and condition of facial bones is the acquisition of CBCT / CT images, 3D segmentation of facial bones, and the evaluation of dental cast models, or 3D segmentation of teeth.

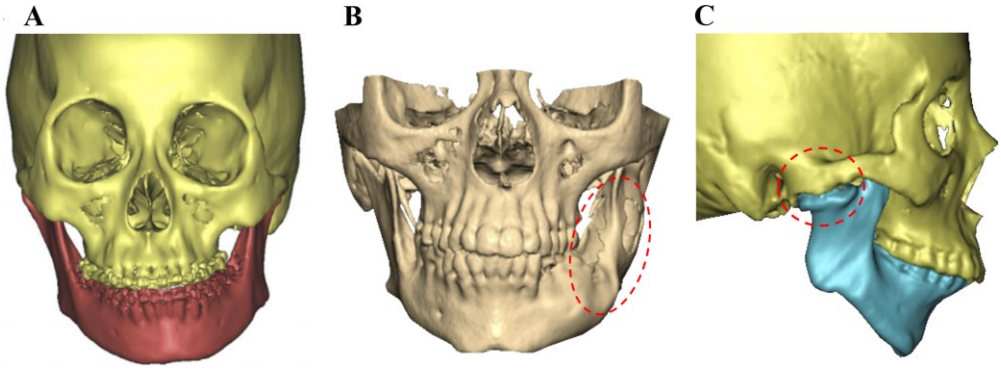

Fig. 1.6. Segmented preoperative facial bones from CT datasets. A – 3D facial bones in order to evaluate skeletal asymmetry (53), B – 3D facial bones in order to evaluate the size of a tumor (54), C – 3D facial bones in order to evaluate the ankylosis of the temporomandibular joint (TMJ) (55)

3D segmentation of facial bones can expand the opportunities to perform accurate analysis and diagnosis of various clinical cases (Fig. 1.6 A, B, C), evaluate the position of teeth before the surgery (Fig. 1.6 A), evaluate the size of a bone defect affected tumor (Fig 1.6 B), or evaluate the condition of TMJ ankylosis before the surgery (Fig. 1.6 C). Accurate segmentation of facial bones provides for more accurate diagnosis and ensures a decrease of the time of treatment (54).

1.2.2 Application of segmented facial bones for the preparation of VSP

Accurate analysis and performed accurate 3D segmentation of facial bones are critical procedures in order to get the best results of the prescribed treatment and to improve the appearance and the quality of life of patients who undergo oral and maxillofacial, orthognathic surgeries (56). The 3D data can enable to get more detailed information about the facial bones. Due to this reason, diagnosis becomes more accurate (57). Segmented 3D facial bones are necessary used to create 3D cephalometry and perform 3D surgical simulation of the selected bones. 3D cephalometry is created by the reference planes. Most commonly, the following reference planes are selected: Midsagittal (MSP, defined as the plane perpendicular to the FH plane and passing through nasion and basion), Frankfort horizontal (FH, defined as the plane passing through the bilateral orbitale and the right porion) and Coronal (CoP, defined as the plane passing through the right porion and perpendicular to the FH plane and MSP) (Fig.1.7). Despite these reasons, the orientation of the reference planes depends on the quality of 3D segmentation. The

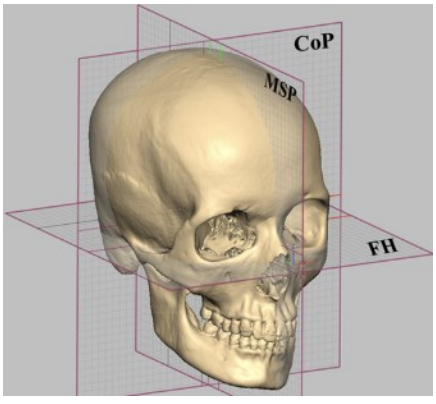

Fig. 1.7. Reference planes (MSP, FH and CoP) for accurate head orientation performance (58)

reference planes are also used to perform the accurate orientation of the head. This is the most important factor for 3D analysis and the performance of VSP (58 – 61). VSP is performed by the translation and rotation of the selected anatomical segment or segments (proximal segments, maxillary segments, mandible body, chin), and also the maxillomandibular complex (Fig. 1.8).

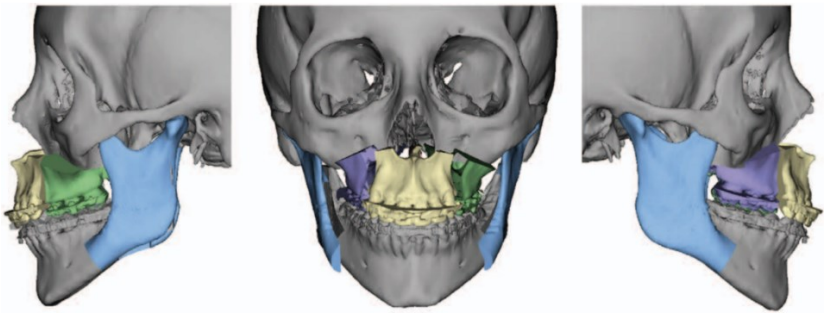

Fig. 1.8. Three-piece Le Fort I and bilateral sagittal split osteotomy (BSSO) for the final position of facial bones (62)

VSP could be implemented by the most popular software packages: Mimics (63), Dolphin imaging (64), NemoFab (65).

1.2.3 Application of segmented facial bones for the fabrication of patient-specific surgical guides

The application of patient-specific surgical guides can improve the accuracy of the surgery (66, 67).

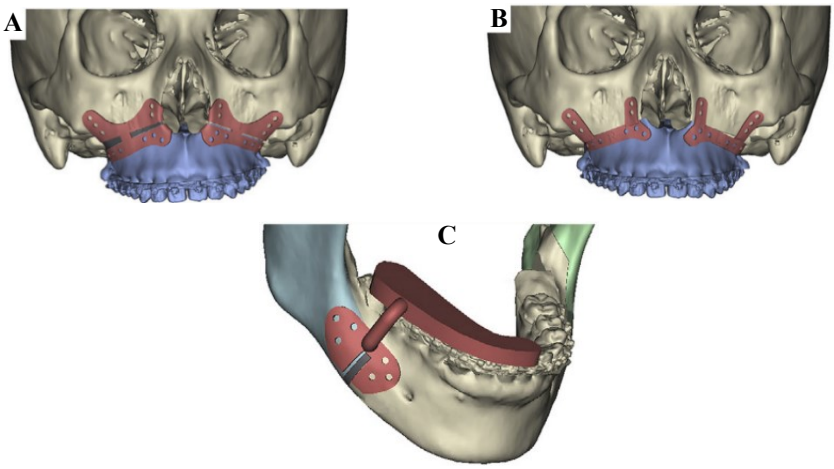

Fig. 1.9. A – The cutting guides (red plates) designed by the planned cutting of osteotomy and ostectomy. **B** – The custom plates (red plates) designed to fit the bony surface above the Le Fort I osteotomy line. **C** – The cutting guide (red plate) designed by the panned cutting of osteotomy and ostectomy (69)

The quality of facial bones segmentation influences the accuracy of patient-specific guides and the success of the surgery (68). The application of patient-specific surgical guides is important in oral and maxillofacial, orthognathic (69, 70), and craniomaxilofacial surgery (67, 71).

Patient-specific guides are designed individually. The fabrication of guides depends on the segmented facial bones from the CT/CBCT dataset, the patient's pathology and the surgeon's requirements for the design. Patient-specific guides could be fabricated by the technologies of selective laser sintering (SLS) (69), selective laser melting (SLM) (72), electron beam melting (EBM) (69) applied in 3D printing or by using milling machines (73).

1.2.4 Application of segmented facial bones for further patient's follow-up

During the last decade, the evaluation of the treatment results is performed by using 3D segmentation of facial bones and the selected superimposition techniques (74 – 76). Superimposition by using 3D models can provide accurate and reproducible results, while also offering high efficiency and increased post-processing capabilities (77). There are some important factors for obtaining accurate evaluation by using 3D models: to use the same parameters during CBCT scanning, to precisely select a threshold value, or to use an appropriate method of CBCT scan segmentation in order to get an accurate 3D model (78 – 80), to select (a) stable reference anatomical area/s so that to perform the superimposition of a 3D model (81 – 83). It depends on what kind of research is performed. After the implementation of these steps, the process of evaluation becomes accurate and objective.

The implementation of different techniques of superimposition is divided into three main groups: 1. landmark-based, 2. surface-based and 3. voxel-based. The superimposition of 3D models is most commonly implemented by the landmark-based technique (84) or by the surface-based technique (84, 85). The landmark-based superimposition technique is more frequently used to perform the initial superimposition when the position of two 3D models under comparison is very different in the digital space. It is a fairly time-consuming and imprecise technique. The final result of superimposition by the landmark-based technique depends on the quality of the 3D models and the user's experience. The idea of the landmark-based method is to select landmarks on anatomical placements which should be stable (non-operated, not growing). An accurate result is achieved when the positions of the selected pairs of landmarks on 3D models are similar (86).

After the initial superimposition (by the landmark-based technique), the surface-based technique is used to increase the accuracy of superimposition (85). The surface-based technique is semi- or fully automatic. The implementation of the surface-based superimposition technique is the base of the iterative closest point algorithm. The performance of surface-based superimposition is rapid. The accuracy of superimposition by the surface-based technique most often depends on the quality of 3D models and the selected anatomical areas. More complex investigations are needed in the studies of growing anatomical structures in order to get accurate

results of superimposition by using the surface-based technique (86). This is typical for young, growing patients (children) because there is difficulty in finding a stable, non-growing anatomical structure which could be used as a reference for the implementation of the superimposition (87). More complicated cases were solved by (88).

The superimposition by the voxel-based technique is used to evaluate the changes of condyles during orthodontic treatment (89), to follow bone changes after a surgery at different time points, or to evaluate the accuracy of the performed surgery (90 – 93). The reference anatomical structure as in the previously described superimposition techniques must be stable. For the anatomical changes of the mandible, mandibular symphysis is used in order to accurately perform superimposition (89). For the assessment of maxillary changes or for the evaluation of the accuracy of the performed surgery, the cranial base is used as the reference structure (Fig. 1.10) (92).

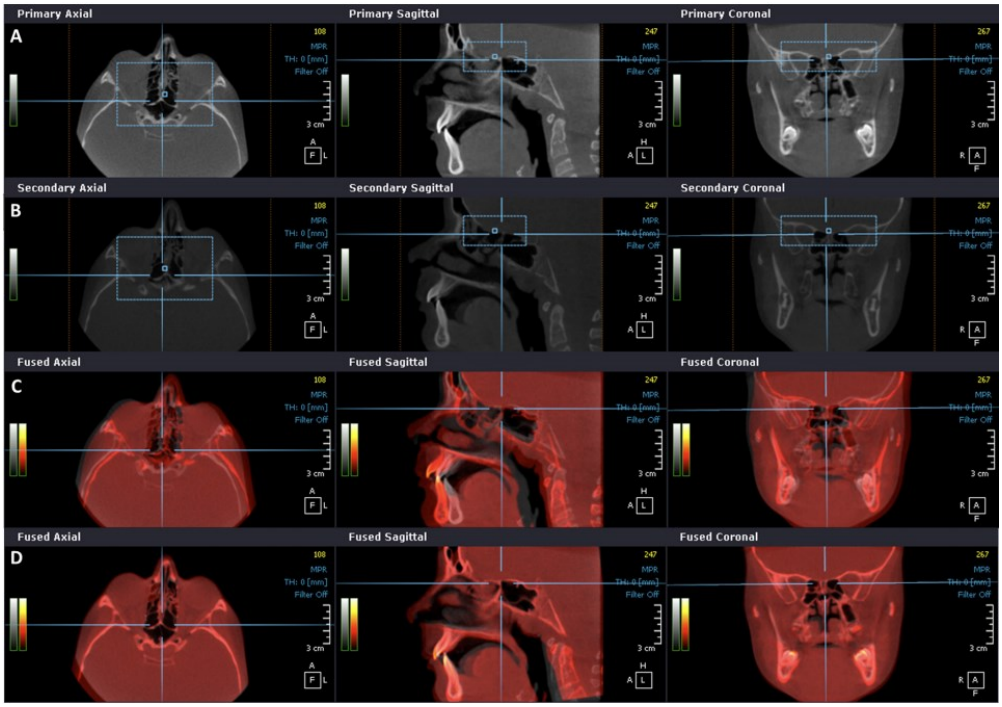

Fig. 1.10. Workflow of voxel-based superimposition. Cranial base (marked on the top blue color dashed rectangle) was selected as the reference anatomical structure in order to superimpose the same patient's CBCT datasets (92)

After the voxel-based superimposition, the 3D segmentation of facial bones is performed. If the superimposition was performed accurately, the segmented bones (3D models) should be in the same position of the 3D space.

The results of the superimposition could be evaluated by the 3D color coded map (Fig. 1.11). The distances between two superimposed 3D models are coded by colors. Each color represents the distance differences by the selected measure of the

International System of Units (SI) (μm, mm or cm). The positive values of the scale represent the regions that are in front of the reference 3D model. The negative values of the scale represent the regions that are behind the reference 3D model. The middle values of the scale represent the regions that have minimal differences between the superimposed 3D models (93, 94).

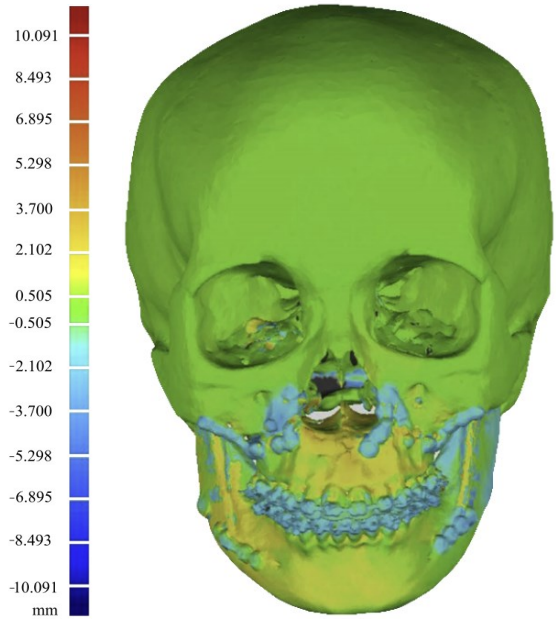

Fig. 1.11. Distance differences between VSP and the surgical result after voxel-based superimposition by the 3D color coded map (units – mm) (93)

The 3D color map helps surgeons perform preoperative evaluation, treatment planning, and the evaluation of the surgical results (58, 94). A 3D color map can be applied after each technique of superimposition for the visualization of surface differences.

1.3 Conclusion of the chapter

1. An asymmetrical face is common in the population. Facial asymmetries can cause physiological, psychological, and emotional consequences. These consequences have an important impact on people's daily lives.
2. 3D segmentation of facial bones helps doctors more accurately evaluate the condition of facial bones, prepare an accurate virtual surgical plan, and follow changes of facial bones during or after the treatment.
3. Accurate 3D segmentation of the facial bones ensures accurate fabrication of the patient-specific surgical guides, which can improve the accuracy of the surgery.

2 OVERVIEW OF EXISTING METHODS FOR THE FACIAL BONES SEGMENTATION IN CBCT DATASET

The main methods for the facial bones segmentation by implementation could be divided into the following: manual segmentation, global thresholding, edge detection, and region growing (20).

2.1 Manual segmentation

The implementation of manual segmentation is based on manually selecting the voxels or the boundary of anatomical regions, and it is most commonly considered as the ground truth (gold standard) method. The accuracy of the proposed new segmentation methods is usually evaluated by comparing the obtained results with the results performed by manual segmentation (95 – 98). The result of manual segmentation basically depends on the experience of the user (a clinical expert, or a medical engineer). The manual segmentation method is considered to be an accurate method, however, looking from the labor costs point of view, it is highly time-consuming (95). The main workflow of the strategy how manual segmentation is performed is presented in Figure 2.1.

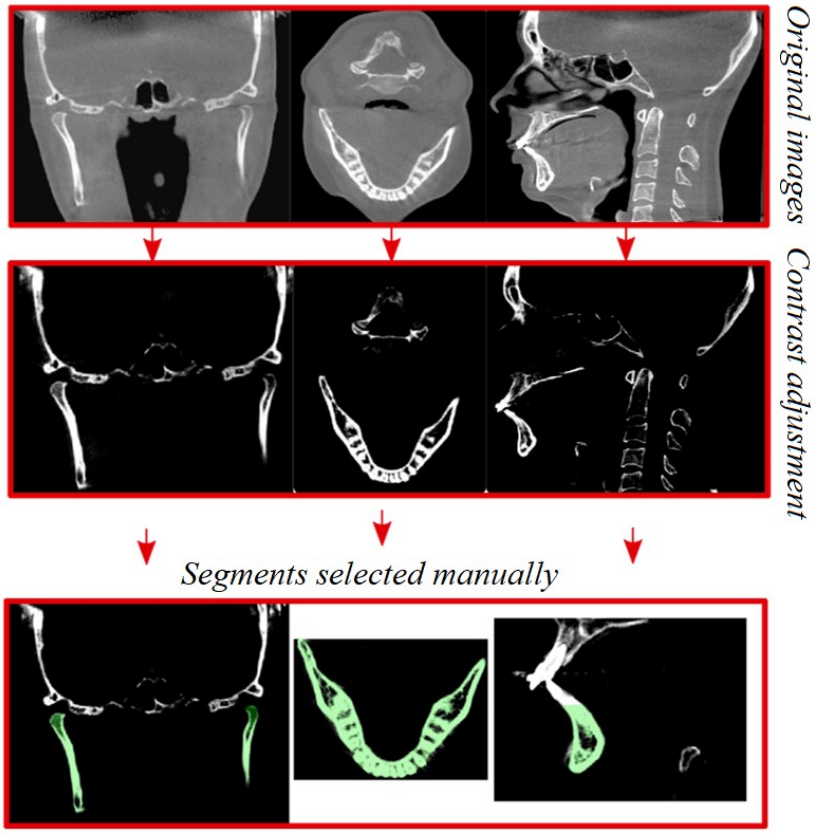

Fig. 2.1. Workflow of manual segmentation by the selected voxels of mandible

Contrast adjustment of images is performed in order to highlight the voxels of the region of interest. Finally, segmentation is done by manually selecting voxels in different views (axial, coronal and sagittal) of CBCT.

2.2 Segmentation by the global thresholding

Most often, manual segmentation is performed by combining the global thresholding method (2.1) by the selected HU (grey level). This is important when certain anatomical regions are lost after global thresholding. Therefore, segmentation is completed by selecting the missed voxels slice-by-slice in the axial, coronal and sagittal views manually (99).

$$g(x,y,z) = \begin{cases} 1 & if \quad f(x,y,z) \geq \theta \\ 0 & else \end{cases}, \tag{2.1}$$

where, *g(x,y,z)* is the matrix of the segmented area, θ is the selected value of the global threshold, *f(x,y,z)* is the original dataset matrix.

The global thresholding method notably and, most commonly, cannot accurately segment the sensitive anatomical areas (condyles and sinuses) or the images in which some kinds of artefacts (metal, beam hardening) or noise (17) are present. In Figure 2.2 A, a mandible is presented which is segmented by the global thresholding technique (selected value 350 HU). The condyles of the mandible are not fully segmented (Fig. 2.2 A). In order to obtain the full segmentation of condyles, manual segmentation is required. The result after manual segmentation is presented in Figure 2.2 B.

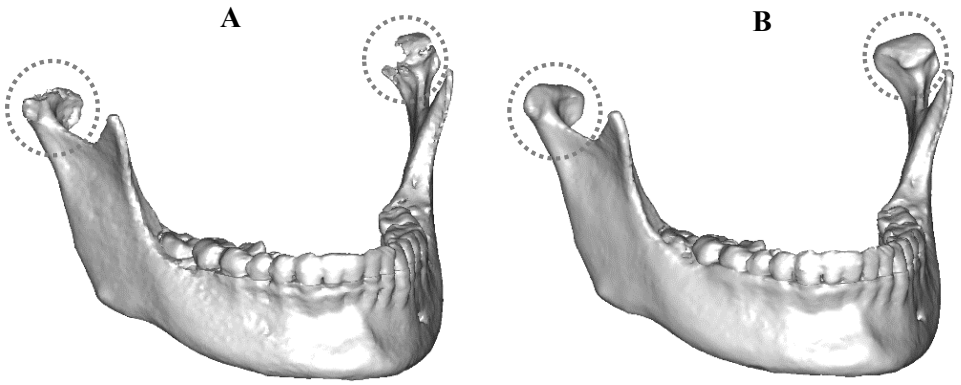

Fig. 2.2. Segmented mandible by using global thresholding (A) and manual segmentation (B) techniques. Dashed circles mark sensitive anatomical areas (condyles) for segmentation

This dual method to perform segmentation is usually used in the clinical practice in order to get an accurate 3D model. However, when applying the global

thresholding method, extensive manual post-processing (manual segmentation) is required (17). This process takes time as well as experience.

The global threshold value could be selected manually by evaluating the histogram of CT/CBCT datasets (100). In Figure 2.3, we present an example which shows what are the differences of the user-selected threshold values when segmenting facial bones by using CBCT and CT datasets.

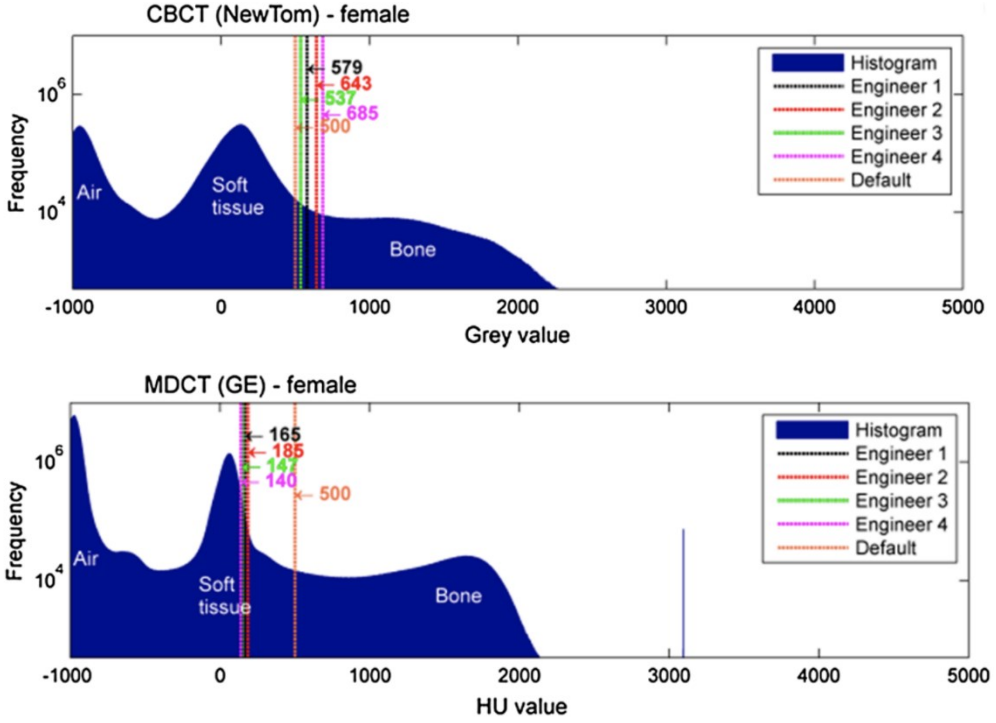

Fig. 2.3. Threshold values (HU) selected by four users in order to segment facial bones (100)

The presented results show that the user-selected grey values were closer to the soft tissue when the objective was to segment bone segments more fully. The performed study showed that there is no single threshold value for all facial bones. The results of segmentation were compared with the results of the optical scanner. The achieved results demonstrated surface inaccuracies ranging from −2.3 to +4.8 mm (CBCT). The final segmentation showed that the result depends on the quality of the data and the experience of the observer. In this study, segmentation was performed by medical engineers. Also, different CBCT, especially the CT device, generates not the same grey values of the investigated anatomical area. Due to this reason, global segmentation becomes more complicated when the threshold is selected manually (100).

Global segmentation could be implemented by adapting automatic methods. One of them is N. Otsu (further referred to as *Otsu's*) method (101) where the optimal threshold value is found from the grey level histogram automatically. The optimal threshold value is found by using the discriminant criterion when trying to

maximize the separability of the resultant classes in the grey level histogram. The basic drawback of this method is that the histogram under analysis must be bimodal, i.e., it should have two expressed peaks of grey levels. This means that the intensity values of the voxels must be divided into two basic classes C0 with the intensity range [1, ..., T] and C1 with the intensity range [T + 1, ..., L] (where L is the upper limit of intensity in the volume), with T representing the threshold optimally separating modes in the bimodal histogram. The number of the voxels with the intensity threshold i is denoted by n_i. The probability of intensity threshold i in the image is (101):

$$p_i = \frac{n_i}{N}, \tag{2.1}$$

N – the total number of voxels. Then, the probabilities that randomly selected voxels belong to one of the classes C0 or C1 are:

$$C_0 : \omega_0(T) = \sum_{i=0}^{T} p_i , \tag{2.2}$$

$$C_1 : \omega_1(T) = \sum_{i=T+1}^{L} p_i . \tag{2.3}$$

The average of classes is defined as:

$$C_0 : \mu_0 = \frac{\sum_{i=1}^{T} i \cdot p_i}{\omega_0(T)}, \tag{2.4}$$

$$C_1 : \mu_1 = \frac{\sum_{i=T+1}^{L} i \cdot p_i}{\omega_1(T)} . \tag{2.5}$$

The intensity average of the total image is defined by:

$$\omega_0\mu_0 + \omega_1\mu_1 = \mu_T , \tag{2.6}$$

$$\omega_0 + \omega_1 = 1 . \tag{2.7}$$

By using discriminant analysis, Otsu's method defines the variance of both classes of the thresholded image as:

$$\sigma_B^2 = \omega_0(\mu_0 - \mu_T)^2 + \omega_1(\mu_1 - \mu_T)^2 \quad . \tag{2.8}$$

Then, the optimal threshold value is calculated by:

$$T^* = Arg \quad Max \quad \{\sigma_B^2(T)\} \\ 1 \le T < L \qquad . \tag{2.9}$$

The histogram of the CBCT dataset is not bimodal, and Otsu's method will not work accurately if we use it to find the accurate threshold value.

According to this, Barandiaran *et al*., 2009 (102) proposed an automatic method for the segmentation of mandibles from CT datasets. These authors used Otsu's method in order to compute the appropriate thresholds. The most accurate segmentation results were achieved by using three threshold classes. A binary image mask was created by computed threshold values by using Otsu's method. The final segmentation was performed by using the region growing method. Twelve different CT datasets were used. The average computational time to perform the segmentation was as little as 10 seconds per dataset. However, any metrics in order to evaluate the accuracy of the segmentation by the using proposed automatic method were not used.

Indraswari *et al*., 2019 (103) proposed automatic segmentation of the mandibular cortical bone in CBCT datasets (Fig. 2.4). The Gaussian mixture model (GMM) for histogram thresholding was used. The proposed method gives the average accuracy, sensitivity, and specificity value of 96.82%, 85.96%, 97.60%, respectively. The segmentation by using the proposed method (GMM) was compared with Otsu's method (101) and histogram cluster analysis (HCA) (104). The achieved results showed that the segmentation results by Otsu's method and HCA are very similar. The authors did not specify how many CBCT datasets were used in their study.

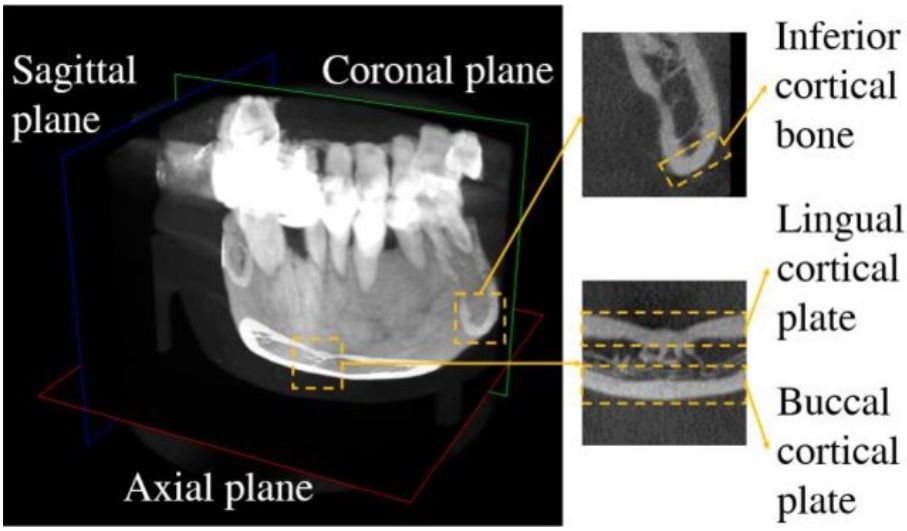

Fig. 2.4 Anatomical regions for segmentation (103)

The authors tested the proposed method with a limited CBCT field of view (FOV). The anterior part of the mandible not involving the whole mandible was used to perform automatic segmentation.

2.3 Segmentation by region growing

The main goal of this region based image segmentation method is to partition an image into regions. The basic steps to implement this method (105) are:

- An initial set of small areas is iteratively merged according to similarity constraints.
- The process is started by choosing an arbitrary seed pixel and comparing it with the neighboring pixels.
- The region is grown from the seed pixel by adding in the neighboring pixels that are similar, thus increasing the size of the region.
- When the growth of one region stops, we simply choose another seed pixel which does not yet belong to any region and start again.
- This process is continued until all the pixels belong to some region.

The region growing method was created to segment regions of interest from 2D images. However, some scientists applied this method for 3D segmentation of a bone (106, 107). Minnema *et al*., 2018 (17) applied the concept of this method in order to create a fully automatic method for bone segmentation by using the convolutional neural network (CNN). CNN was trained with CT datasets acquired by using six different scanners.

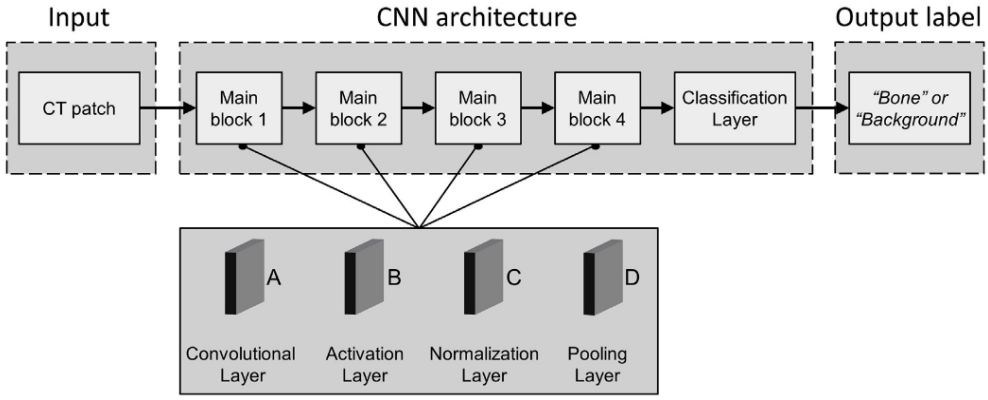

Fig. 2.5. Architecture of the presented method by using CNN with four blocks (17)

All CT scans were normalized by rescaling the voxel values between *0* and *1*. Voxels were used to create 33 × 33 patches centered on each voxel. The created patches contained the intensity values of the surrounding voxels. The patches were then used to train CNN to classify the center voxel of each patch as either 'bone' or 'background'. The achieved results were compared with the 3D models created by an experienced medical engineer. The accuracy of the proposed method was evaluated by Dice similarity coefficient (DSC) (the mean value of DSC = 0.92 ± 0.04) and the mean surface deviation (mean deviation = 0.44 mm ± 0.36 mm). The segmentation of a full CT dataset was approximately an hour. The achieved results showed very high accuracy of segmentation. The study was performed by using CT datasets where the quality of data is higher than the CBCT data. Also, the authors

did not test the proposed method for mandible segmentation. A large amount of data for training is needed.

Wang *et al*. published two studies in 2013 (6) and 2014 (15) to represent a new automatic method for bone segmentation estimating a patient-specific atlas by using the sparse label fusion strategy from spiral CT atlases. The aim of the presented method was to segment separately three anatomical regions: the mandible, the maxilla, and the background from CBCT datasets, and also to separate the mandible from the maxilla. Patient-specific atlases were created by using spiral CT datasets. The authors estimated a patient-specific atlas from spiral CT atlases by using the sparse label fusion strategy. The second step was to integrate an estimated patient-specific atlas into a convex segmentation framework based on the maximum a posteriori probability (MAP) for accurate segmentation (Fig. 2.6).

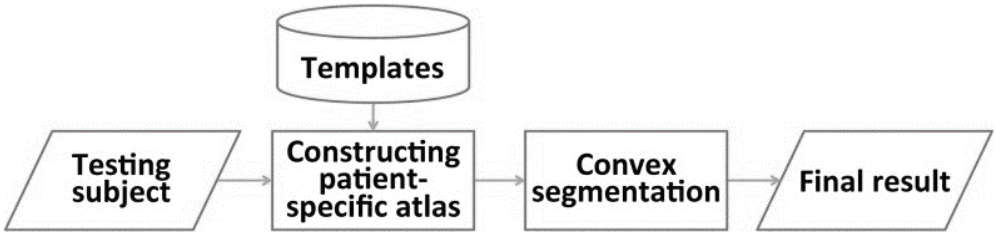

Fig. 2.6. Flowchart of the proposed methods (15)

The authors applied a patient-specific atlas in order to increase the amount of the analyzed information (e.g., the anatomical pattern) about the patient in this study. The results of segmentations were very accurate. The calculated metrics in order to evaluate the method efficiency were: DSC, mean surface distance (MSD), and Hausdorff distance (HD) (Table 2.1).

Table 2.1. The calculated metrics by using the automated segmentation of a CBCT image using spiral CT atlases and convex optimization (6) and automated bone segmentation from dental CBCT images by using patch-based sparse representation and convex optimization (15)

Metrics	**Region of interest**	**Wang *et al*., 2013 (6)**	**Wang *et al*., 2014 (15)**
DSC	Mandible	0.91 ± 0.02	0.92 ± 0.02
	Maxilla	0.87 ± 0.02	0.87 ± 0.02
MSD, mm	Mandible	0.61 ± 0.17	0.65 ± 0.19
HD, mm	Mandible	0.92 ± 0.47	0.96 ± 0.53

When comparing the calculated metrics, the authors showed very similar results of segmentations. However, the automatic segmentation by the proposed method is performed for a long time. The mean time to perform one segmentation is about 5 h (15). Due to this reason, the application of segmentation would be a hard task in the 'real' clinical practice.

The same group of scientists (16) presented a new method for bone segmentation by using the random forest method. The multiclass classifier was used

to create probability maps for each region of interest (the mandible, the maxilla and the background). The achieved results were compared with the ground truth 3D models (segmented by two experienced surgeons). In this study, 30 CBCT datasets were used. The proposed method consists of four main steps: 1) estimation of the initial probability maps with majority voting; 2) extraction of CBCT appearance and context features; 3) training of random forest based classifiers; 4) repeating Steps 2 and 3 until convergence. The method flowchart is presented in Figure 2.7.

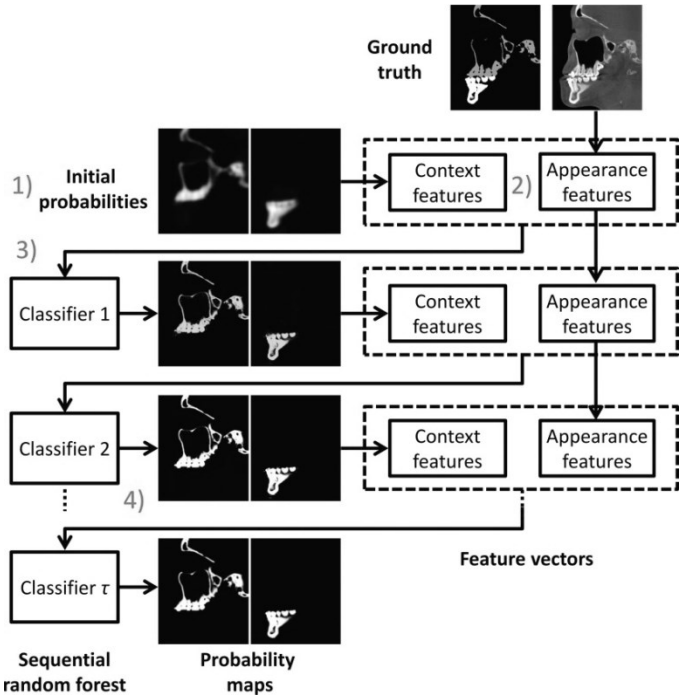

Fig. 2.7. Flowchart of the random forest method with the main steps in order to perform segmentation (16)

In Step 1, experienced surgeons performed segmentations of all CBCT datasets. These results were used to perform initial estimations of probabilities in order to create a base of probability maps for the mandible and the maxilla at each voxel (approximate localization). In Step 2, the features of context and appearance were extracted. It is important for the training of classifiers. For the extraction of the appearance and context features, the authors used Haar-like features. In Step 3, the training of random forest based classifiers was performed. In order to improve the segmentations, classifiers were trained for the complex relationship between the local appearance/context features and the corresponding manual segmentation labels on all the voxels of the training atlases. In Step 4, Steps 2 and 3 are repeated until overlap has been reached. In this step, the training of classifiers is important and consistent. The authors achieved accurate results of segmentation (Table 2.2).

Table 2.2. Calculated metrics by using the proposed methods (16)

Metrics	Region of interest	Wang *et al*., 2016 (16)
DSC	Mandible	0.94 ± 0.02
	Maxilla	0.91 ± 0.03
MSD, mm	Mandible	0.42 ± 0.15
HD, mm	Mandible	0.74 ± 0.25

This proposed method also suffers from some limitations: the limited amount of CBCT data and the noticeable computational time of segmentation (20 min).

Fully automatic segmentation was presented by Fan *et al*., 2019 (19). The idea is to apply the marker-based watershed transform as the base for the region growing method. The proposed method was applied for mandible segmentation from the CBCT dataset (Fig. 2.8).

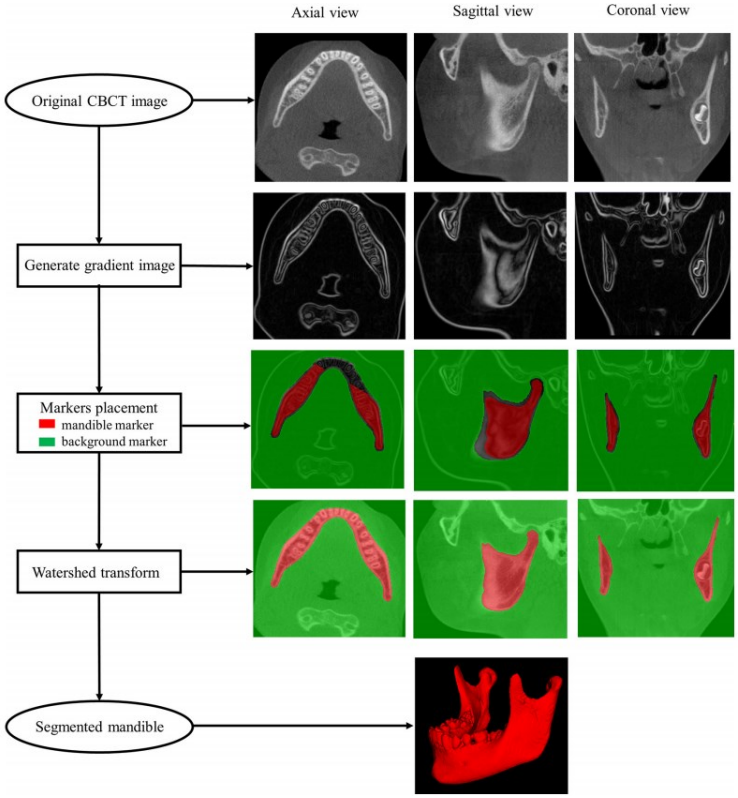

Fig. 2.8. Flowchart of the automatic segmentation method by using marker-based watershed transform (19)

The idea of the proposed method was to divide anatomical regions into the bone area (mandible) and the background (soft tissue and air). First of all, the original matrix of the image was transformed into a matrix of gradient by using the Derivative of Gaussian kernel. Transformation changed the intensity values of the original voxels. The boundaries of anatomical regions became more highlighted. Two markers were used to perform the segmentation. One marker was placed inside

the mandible, whereas the other was placed outside of the mandible. The watershed transform floods the gradient image by dilating the markers simultaneously until colliding at the watershed lines, thus estimating the mandible boundary. The authors used 20 CBCT datasets in order to evaluate the accuracy of the proposed method. DSC was used for the evaluation of segmentation. The mean DSC was 0.97 ± 0.01. The calculated metric showed high accuracy of segmentation. However, some errors of segmentation were around the wisdom teeth, condyles, and the dental enamel. The reasons of segmentation errors were due to the different (bigger or the same) intensity values of the selected markers (the mandible and the background). The accuracy of segmentation of the proposed method depends on the quality of the CBCT dataset in use. It is sensitive to metal artefacts which are very common for patients with orthodontic or craniomaxillofacial anomalies. Manual post-processing editing is recommended.

2.4 Segmentation by the edge

For mandible segmentation, Gollmer *et al*., 2012 (18) proposed to use an SSM. SSM is used to analyze the morphometry of an object. It describes the shape/edge of the object by applying principal component analysis (PCA). SSM is based on a set of landmark points capturing the shape of the object in every image. Thirty cases were used in this study. All the cases were segmented semi-automatically from CT datasets and used for building SSM. The authors tested the proposed method by using six CBCT datasets. They used three approaches to implement SSM: distortion-minimization (*distmin*), the *detcov* cost function, and the *spharm* method. The accuracy of segmentation was evaluated by the following four metrics: the average symmetric surface distance (ASD), the root mean square symmetric surface distance (RMSD), the maximum symmetric surface distance (MSSD), and the volumetric overlap error (VOE). The results are presented in Table 2.3.

Table 2.3. Calculated metrics by using different SMMs (18)

Approach	ASD, mm	RMSD, mm	MSSD, mm	VOE, %
distmin	0.9 ± 0.2	1.4 ± 0.3	9.6 ± 2.5	24.3 ± 0.2
spharm	0.9 ± 0.1	1.4 ± 0.2	10.9 ± 3.7	23.3 ± 0.2
detcov	0.8 ± 0.1	1.2 ± 0.2	10.0 ± 3.2	20.9 ± 3.9

The calculated metrics showed very similar results when using different methods of SMM. Better results are recorded when using the *detcov* cost function evaluating the differences by surface. However, the amount of the training cases is too low in order to get high efficiency of the proposed method and to apply it in clinical practice. SMM is a progressive method in medicine to perform the segmentation of a selected anatomical region; however, the implementation of this method requires sizable training data.

Wallner *et al*., 2019 (169) made profound systematic evaluation by using six methods of segmentation: GrowCut (the implementation of this method is based on region growing), Robust Statistics Segmenter (the implementation of this method is based on the extraction of the analyzing edge of a selected anatomical area), Region

Growing 3D, Otsu & Picking (based on the thresholding of the analyzed anatomical area), Canny Segmentation (based on edge detection by the implementation of the Canny edge detector), and Geodesic Segmenter (based on the level set speed function). Three of them were based on edge extraction, whereas two were based on region growing, and one was based on global thresholding. The anatomical region was the mandible. Ten CT datasets were used in this study. For the implementation of segmentations, open-source software (*Slicer*, *MITK* and *MeVisLab*) was used. The basic metric to evaluate the accuracy of the different methods was: DSC, HD and Pearson's correlation coefficient (r). Comparisons were made between the segmentation algorithms and the ground truth segmentations of the same anatomy performed by two clinical experts. In summary, the segmentation accuracy was highest when using the *GrowCut* (DSC 85.6%; HD 33.5 voxel) algorithm and the Canny (DSC 82.1%; HD 8.5 voxel) algorithm.

2.5 Surface reconstruction

Accurate surface reconstruction from a segmented discrete voxel dataset is a difficult but fundamentally important task (108). The final evaluation of a 3D model after surface reconstruction can be performed.

There are a number of different methods of surface reconstruction. The most popular method is the marching cubes which was presented by Lorensen and Cline, 1987 (109). This method processes segmented data (a dataset of voxels) in order to calculate triangle vertices by using linear interpolation. The main idea of the presented method is to divide the processed dataset (segmented voxels) into a discrete set of cubes. In each cube, the surface intersection is found. The values of each vertex cubes are compared to a given isovalue. The vertices of a cube with values below the surface receive zero and are outside the surface. The surface intersects those cube edges where one vertex is outside the surface (one) and the other is inside the surface (zero). There are 15 main combinations to create a triangulated surface (Fig. 2.9).

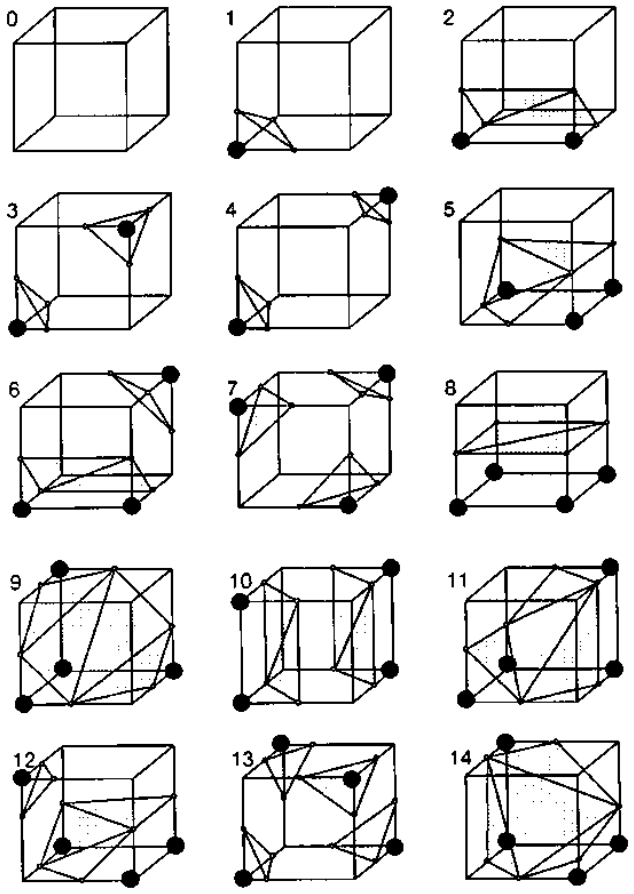

Fig. 2.9. 15 unique combinations of polygons by using marching cubes (109)

The zero (Fig. 2.9; *0*) combination is the simplest of all; the vertex values of the cube are above the selected value, and no triangles are produced.

Different improvements of marching cubes method are performed in order to achieve more accurate results (110 – 112).

Dutailly *et al*., 2009 applied the Half Maximum Height (HMH) algorithm for surface reconstruction (108). The authors reconstructed the surfaces of a segmented mandible, the lower part of a face, and soft tissue. The results were compared with the results by the marching cubes method (Fig. 2.10).

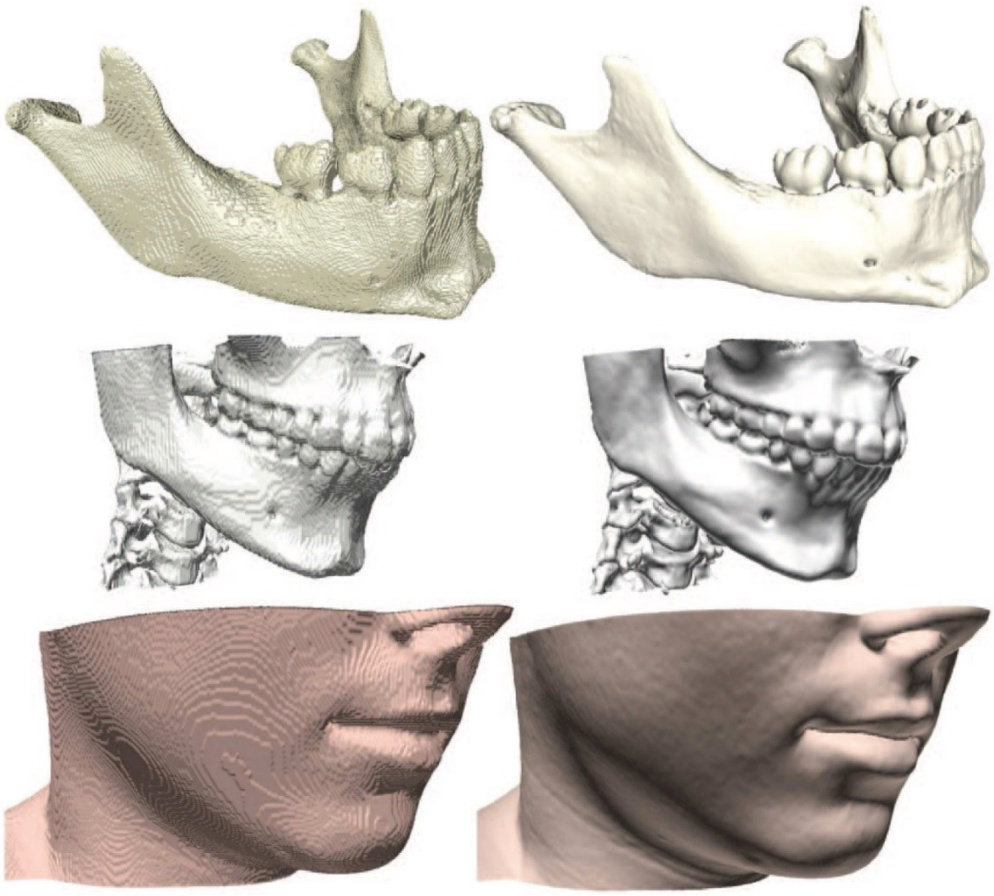

Fig. 2.10. Results of marching cubes reconstruction (left) and HMH reconstruction (108)

The visual results by using the HMH method were better than when applying the marching cubes method. The mandibular condyle width on the left and on the right side, the symphysis height between the two decidual central incisors, the height of the body of the mandible between the two decidual molars on the left and on the right side of the jaw were used as the measurements in order to evaluate the accuracy of the comparable methods. The measurements taken with a caliper with measurements computed on the surfaces extracted both by the original Marching Cube algorithm and by the HMH method were performed. The mean of the absolute error was 0.37 mm for HMH, and 0.57 mm for the marching cubes method (108).

Curless and Levoy, 1996, presented a method for surface reconstruction (113). The implementation of the presented method consists of the cumulative weighted signed distance function. The processed dataset is converted to distance functions. The space efficiency was achieved by the run-length encoding of the volume. The final surface reconstruction was made by adapting the Marching cubes method. The surface was reconstructed by extracting an isosurface from a volumetric grid. The presented method was used to reconstruct the surface during optical scanning.

However, improvement of the presented method is implemented in *Meshlab* software (114) and can be used in order to reconstruct the surface of segmented voxels from CT, CBCT, MRI datasets.

2.6 CBCT imaging technology

CBTC is one of radiographic tools (115). Historically, the first applications of CBCT were intended for angiograms. Today, CBCT is widely used in the practice of dental and maxillofacial radiology. There are two main factors that have played a large role in the rapid adoption of CBCT in dentistry. The first of them is that it is a low-cost and rapid technology compared with the conventional CT. The second aspect is the ability of software engineers to develop multiple dental imaging applications for CBCT with broad diagnostic capability (116, 117). CBCT provides sub-millimeter resolution images of high diagnostic quality coupled with a short scanning time and a reduced radiation dose up to 10–15 times lower than the conventional CT (118).

2.6.1 Imaging geometry of CBCT

The hardware and software of the contemporary CBCT scanners are greatly improved comparing to the first prototype (117).

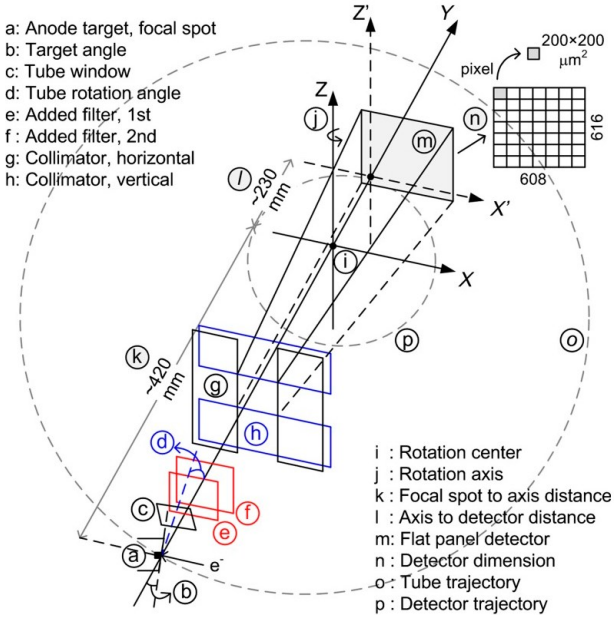

Fig. 2.11. The image acquisition structure of the CBCT system (*Scanora 3D*) (119)

The position of the tube in CBCT is in the direction that the axis of the anode to the cathode lies orthogonally to the longitudinal field of view (FOV). The flat panel detector is with a 608 × 616 array of 200 × 200 µm^2 pixels. The tube is rotated upwards about the anode to the cathode axis by a small angle. There are two filters

which are placed in the beam path, each made of a 0.1 mm flat copper sheet. The source-detector movement follows the step-and-shoot (pulsed) pattern, with the half projections distributed evenly over 360° (119). Also, a lot of clinical CBCT devices use circular gantry rotation with the minimum angular coverage of 180°+ cone angle (120). In CBCT systems, the X-ray beam forms conical geometry between the source and the detector. In the conventional CT, the collimator restricts the X-ray beam to approximately 2D geometry (fan). In the fan-beam single-detector arc geometry, data acquisition requires both rotation and z-direction translation of the gantry to eventually construct an image set composed of multiple axial sections (Fig. 2.12) (121).

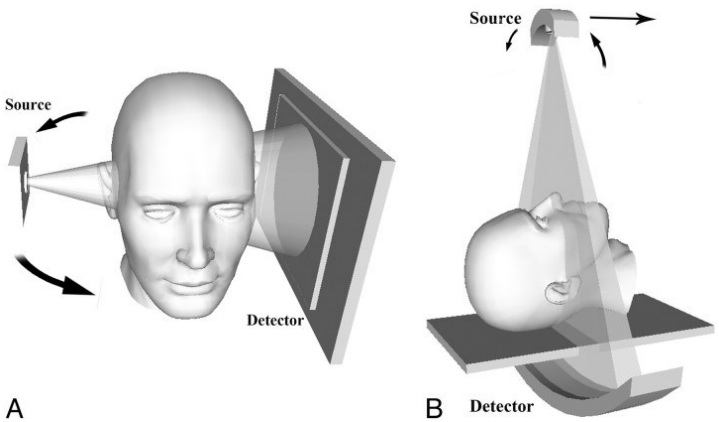

Fig. 2.12. CT acquisition geometries. **A** – geometry of cone beam CT, **B** – geometry of conventional CT (fan beam) (121)

The field of view of commercially available flat panel CBCTs ranges from 8 cm × 5 cm to 23 × 17 cm. It depends on what volume is needed to investigate (e.g., the mandible, the maxilla, or the mandible with the maxilla). Nine different FOVs, which can be selected during the scanning are presented in Figure 2.13 (122).

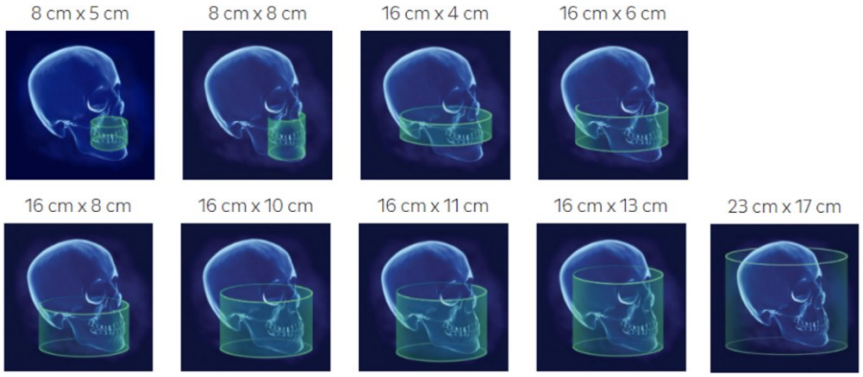

Fig. 2.13. Different sizes of FOVs applicable in *i-CAT FLX V17* CBCT (122)

If the larger FOV is enabled, then, a greater extent of the patient is captured in the image; however, larger FOVs increase the scatter of X-rays. First of all, it affects

the loss of contrast and increases scatter artefacts (cupping, streaks, truncation) (120).

2.6.2 CBCT X-ray detector technologies

X-ray detectors of CBCT devices are mostly used with flat panel imagers (FPIs) that are made with the amorphous silicon (A-Si) thin film transistor (TFT) technology. FPIs consist of a large area of A-Si semiconductors. This technology has been included into large area active matrix flat panel imagers (AMFPIs). There are two principles used in AMFPIs: direct and indirect conversion (120).

Direct conversion detectors

The most commonly used option in all commercial CBCT devices is AMFPIs with direct X-ray conversion. X-ray conversion gain depends on the electric field. The nominal value for energy to generate an electron hole pair is 50 eV. Direct conversion detectors have the ability to make smaller pixels due to its simpler structure. The geometric fill factor of direct AMFPIs is higher {1} than the indirect detector {0.7}. The direct detector uses an X-ray photoconductor to convert X-rays directly to the charge (Fig. 2.14, a) (120).

Indirect conversion detectors

Indirect AMFPIs have been used less frequently than direct conversion detectors. The fill factor depends on the pixel pitch and the design of the TFT array. The indirect method is denoted by a higher X-ray quantum efficiency than direct conversion detectors. The indirect detector uses a phosphor screen or a structured scintillator to convert X-rays to optical photons which are then converted to charge by an integrated photodiode at each pixel (Fig. 2.14, b) (120).

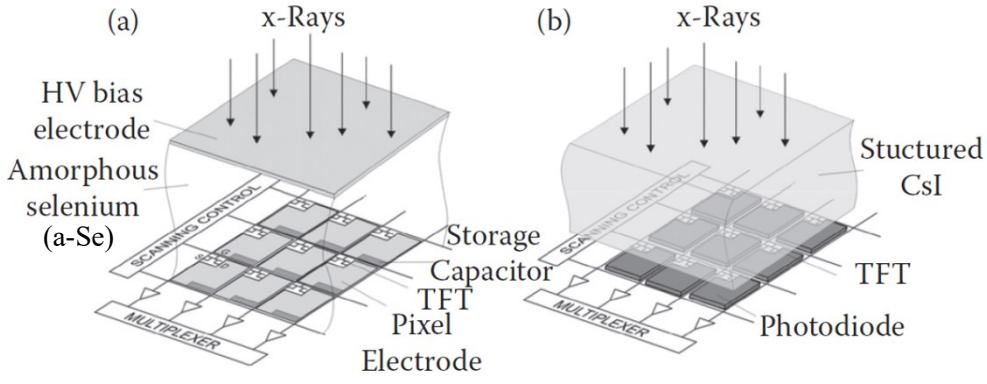

Fig. 2.14. Structure of AMFPIs using direct (a) and indirect (b) X-ray conversion (120)

The detector size ranges from 22 cm × 22 cm up to 43 cm × 43 cm. Detector binning has also been implemented to enable rapid image acquisition in CBCT (120).

2.7 Quality metrics of CBCT images

There are several international standards – the International Electrotechnical Commission (IEC) and the American Association of Physicists in Medicine (AAPM) Task Group that have accepted image quality metrics: the modulation transfer function (MTF), the detective quantum efficiency (DQE) and the noise power spectrum (NPS) (120).

2.7.1 Modulation transfer function (MTF)

MTF is determined by the Fourier transform (FT) of the point spread function (PSF). MTF is measured in orthogonal directions by using FT of the line spread function (LSF) and is the method for the characterization of the spatial response of an imaging system. There are several techniques to obtain the LSF – the fine wire, narrow slits, and the edge phantoms (123). In CBCT devices, the shift-invariance condition is disturbed due to some reasons:

1) digital detectors are undersampled;
2) the projection of an image blur due to the finite focal spot size of the X-ray tube varies with the position of the object plane;
3) the focal spot blur can deteriorate by the focal spot motion during X-ray exposure of the CBCT scan. The MTF values are between *0* and *1*. Also, MTF values are depicted graphically (Fig. 2.15).

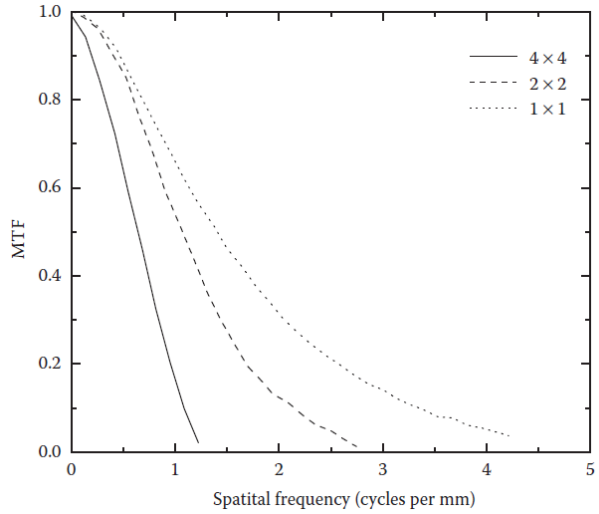

Fig. 2.15. MTF of commercial detectors (120)

Figure 2.15 shows measured MTF with different detector pixel binning. 4 × 4 pixel binning is often used in CBCT image acquisition in order to increase the readout speed. Higher MTF values in the low spatial frequency range are needed to

outline coarse details, while high MTF values in the high frequency range are necessary to portray fine details and sharp edges (120).

2.7.2 Noise power spectrum (NPS)

NPS describes the noise properties of an imaging system. NPS provides information on the noise components for different spatial frequencies. Image blur in an AMFPI detector could lead to the spatial correlation of noise, which results in a high frequency drop of NPS. NPS can be obtained as follows (120, 124):

$$NPS(f_n) = \frac{dxdydz}{L_x L_y L_z} \left\langle \left| DFT(I)_n \right|^2 \right\rangle_{subvolumes} . \tag{2.10}$$

DFT(I) is the Discrete Fourier Transform of zero-mean images (I), f_n is a 3D spatial frequency, dx, dy and dz are the dimensions of the reconstructed voxels, and L_x, L_y, and L_z are the dimensions of the sub-volumes used to estimate the NPS (120, 124).

2.7.3 Detective quantum efficiency (DQE)

DQE is a metric for characterizing the overall efficiency of an X-ray imaging detector. It is defined as the ratio between the signal-to-noise ratio (SNR) squared at the output of the detector and that at the input, which is equal to the number of X-ray photons per unit area (q_0) (120, 121):

$$DQE = \frac{SNR_{out}^2}{q_0} . \tag{2.11}$$

DQE describes the efficiency of the detector in using the incident X-rays, and its upper limit is the quantum efficiency of the detection material (120, 121).

2.7.4 Main factors affecting image quality

Acquisition technique factors, such as peak kilovoltage (kVp), milliamperesseconds (mAs), exert influence on the image quality of CBCT.

The conventional CT is associated with relatively high radiation dose levels. The radiation dose of CBCT is generally lower than for the conventional CT. By the as-low-as-reasonably-achievable (ALARA) principle, the image quality is required to be optimized at reasonably low radiation dose levels (125, 126). The reduction of the dose is very important in order to protect the patient from the unnecessary radiation exposure. By the performed meta-analysis (127), the effective dose levels may range from 5 µSv to 1073 µSv for CBCT. The selected level of the effective dose depends on what size of FOV is used during the scanning. In comparison of conventional CT, the levels of the effective dose could range from 812 µSv to 1892 µSv in the area of the head. Also, a study showed higher spatial resolution of CBCT but lower contrast resolution than the conventional CT (128). One of the main applicable methods to reduce the dose of CBCT is the low tube current-exposure

time (mAs). The low current-exposure time results in a decreased signal-to-noise ratio in the projection images due to fewer incident photons interacting with the detectors (129). The influence of kVp on the image quality is also relevant. A higher kVp value increases the mean energy of the photons in an X-ray beam and the amount of photons. Due to this reason, the optimization of kVp and mAs is required. The changing of mAs or kVp or both is intricate and should be correctly balanced, thus ensuring an adequate image quality by using the lowest possible dose level. mAs and kVp should be determined by the ALARA principle (130, 131).

2.8 Image reconstruction of CBCT

The scanning geometry of CBCT is different from the conventional CT, and the application of the traditional filtered back projection (FBP) cannot be applicable. The filtered back projection algorithm by Feldkamp, Davis and Kress (FDK) for 3D volume reconstruction from cone beam projections is used as one of the most widely used approaches (132). The approach of the FDK algorithm is to apply one-dimensional (1D) filtering on each row of the projection data while assuming that this is the direction parallel to the rotation plane. After that, the back projection is performed by tracing the coordinate of an image pixel back to the X-ray focal spot. The reconstruction is based on pre-weighted filtering and the final back projecting. The pre-weighting is obtained as the cosine of angle ξ between the cone beam ray and the central ray of the projection, which is calculated by (133):

$$\xi = \frac{D}{\sqrt{D^2 + s^s + v^2}}, \tag{2.12}$$

where, D is the distance between the X-ray source and the rotation center, s and v are the coordinates of the flat detector (Fig. 2.16). Assuming that the gathered projection data on (s, v) for projection angle β is $p(s, v, \beta)$, the projection data after pre-weighted filtering can be expressed as (133):

$$\tilde{p}(s,v,\beta) = \left(\xi \cdot p(s,v,\beta)\right) \times h(s), \tag{2.13}$$

where, $h(s)$ is the ramp filter. The final reconstruction of the voxel is represented as (133):

$$f(x,y,z) = \int_0^{2\pi} \frac{1}{U(x,y,\beta)^2} \cdot (\tilde{p}(s,v,\beta)) d\beta, \tag{2.14}$$

where, $U(x,y,\beta) = D + x \cdot \sin\beta - y \cdot \cos\beta$.

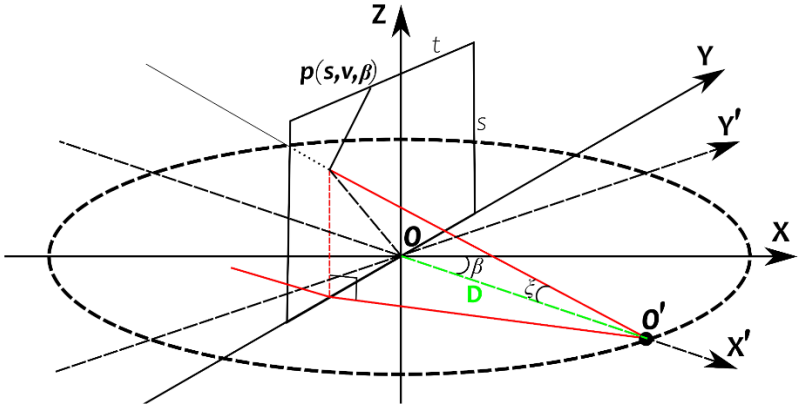

Fig. 2.16. Geometric coordinates of a scanning track for cone beam CT (133)

The reconstruction accuracy of CBCT is limited by the maximal cone angle range, most often, CBCT is designed with a cone angle range within ±15 degrees. Also, due to the approximation nature of the FDK reconstruction, the reconstructed CBCT image pixel values are typically less reliable than the traditional Hounsfield Unit (HU) values from the conventional (fan beam) CT images (133).

2.8.1 Hounsfield units

The smallest element in the CBCT dataset is the voxel. Each voxel has a value in Hounsfield units (HUs). Hounsfield units are characterized as a linear transformation of X-ray attenuation coefficients of a material with the reference material – water. HUs are calculated by the following equation (134):

$$HU_{material} = 1000 \times \frac{\mu_{material} - \mu_{water}}{\mu_{water}}, \tag{2.15}$$

where, $\mu_{material}$ are the linear attenuation coefficients of the material, and μ_{water} are the linear attenuation coefficients of the reference material.

The values of HUs for conventional CT scanners are presented in Table 2.4.

Table 2.4. Typical HU values in CT images (134)

Material	*HU value*	*Notes*
Air	–1000	In vacuum as well for all practical effects
Fat	–100	
Water	0	Distilled, at standard temperature and pressure
Muscle	+40	
Blood	+40	
Bone	>400	Spans over a large range, to ~1200, and occasionally more
Aluminum	2640	At 60 keV

In Table 2.5, we present the values of μ for materials and tissues at photon energies used in medical radiology.

Table 2.5. Values of μ (in cm^{-1}) for materials with various photon energies (134)

Material	*40 keV*	*60 keV*	*80 keV*	*100 keV*
Fat	0.228	0.188	0.171	0.160
Water	0.268	0.206	0.184	0.171
Cortical bone	1.280	0.604	0.428	0.356
Aluminum	1.535	0.750	0.545	0.460
Titanium	10.050	3.480	1.840	1.235

The presented μ values are from the National Institute of Standards and Technology (NIST) tables of X-ray mass attenuation coefficients. The HU values depend on the energy of X-ray photons. Figure 2.17 shows the dependency of HU values for aluminum on different X-ray energies (134).

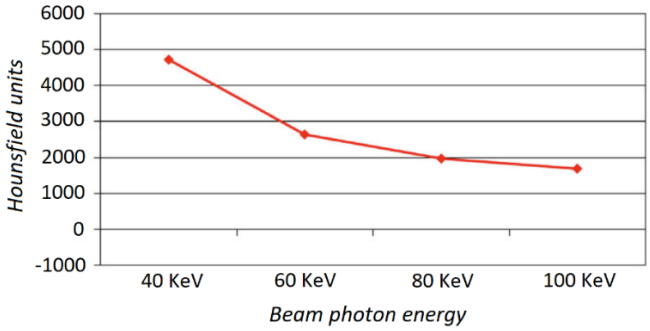

Fig. 2.17. HU values for aluminum with different energies of X-ray (134)

All the presented HU values are calculated from the values of linear attenuation reported in the NIST tables of X-ray mass attenuation coefficients. HU values of some actual materials in dentistry using different X-ray energies are presented in Figure 2.18 (134).

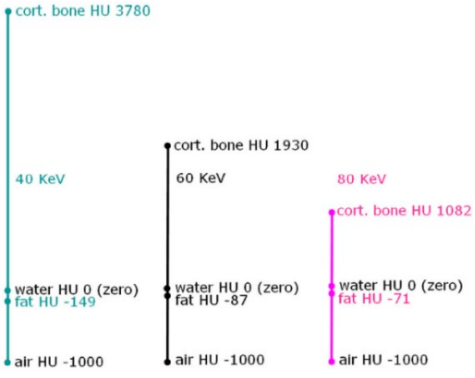

Fig. 2.18. HU values for some tissues and materials at three different X-ray beam energies (40, 60 and 80 keV) (134)

The HU value of water is always 0 HU, and the HU value of air is always –1000 HU based on Equation (2.15). The biggest differences of HU values then compare the bone by using different X-ray beam energies (Fig. 2.18) (134). The materials that absorb more X-rays have a higher HU value. For example, the HU value of the bone is higher than the HU value of a soft tissue (fat, muscles, liver). HU values can be used to quantify the bone material density (BMD). The bone density measurements using CBCT in clinical applications would yield an accurate value. It requires high stability and reliability of grey values and consistent correlation between the grey value and the density.

Misch, 1999 (135) performed a study and suggested a classification of the bone density by HU: D1 bone >1250 HU; D2 bone, 850–1250 HU; D3 bone, 350–850 HU; D4 bone, 150–350 HU; D5 bone, <150 HU. D1 means a dense cortical bone which is found in the mandible. D2 is found in the cortex with the trabecular bone pattern, and this is the most common bone density in the mandible. D3 is found in a thin cortex and a fine trabecular bone pattern, and this is the most common bone density found in the maxilla. D4 is a fine trabecular bone found in the posterior maxilla. D5 is a very soft bone which is usually consistent with sinus graft augmentation.

Later study performed by Norton *et al*., 2001 (136) divided the density of the bone into four main ranges by HU: Q1 – the anterior mandible >850 HU, Q2 – the posterior mandible/anterior maxilla, 500–850 HU, Q3 – the posterior maxilla, 1–500 HU, Q4 – tuberosity region, 0 HU.

Naitoh *et al*., 2004 (137) showed that the facial bones voxel values obtained from CBCT datasets are not absolute. The same group of authors, i.e., Naitoh *et al*., 2009 (138) performed a study in order to evaluate the voxel intensity values in the facial bones by using CBCT datasets.

Aranyarachkul *et al*., 2005 (139) evaluated densities in different areas of jaws (the mandible and the maxilla) by HU. The maximum value was found to be 1143 HU, whereas the minimum value was 80 HU. The reviewed articles showed the ranges of facial bones by HU in CT/CBCT datasets.

Liang *et al*., 2010 (140) performed a study to compare the geometric accuracy of 3D surface model reconstruction between five CBCT scanners and on the conventional CT scanner. The reference 3D model (a dry human mandible) was obtained with a high resolution optical scanner. The mean deviation was 0.137 mm for the conventional CT, the mean deviation for all CBCTs was 0.211 mm. The results showed higher segmentation accuracy of the conventional CT compared to CBCT. The main reason was the higher inherent contrast between the bone and the soft tissue in conventional CT images.

Silva *et al*., 2012 performed a study which showed that the HU values were higher compared with the conventional CT, and also the contrast between the bone and the soft tissue was higher in the conventional CT images (Fig. 2.19) (141).

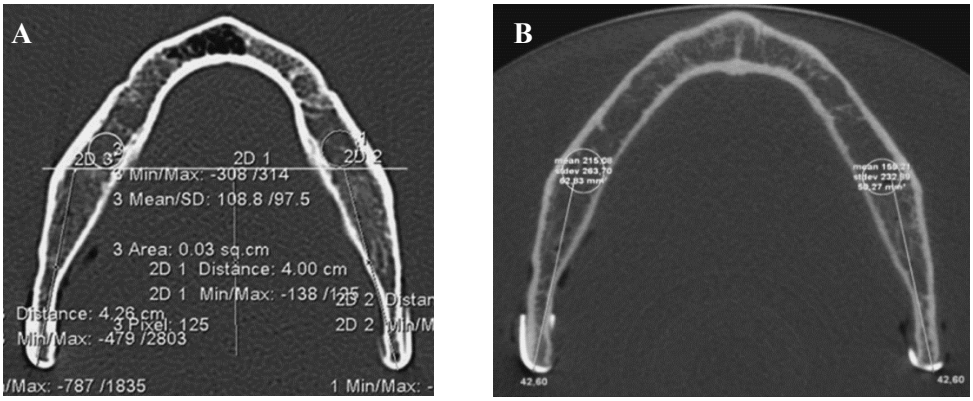

Fig. 2.19. Axial images of a scanned mandible with conventional CT (A) and CBCT (B) (141)

The reviewed studies (135 – 141) showed that there is no absolute value by which one could define the density value by the HU of facial bones. Also, the contrast resolution is lower in comparison with the conventional CT. Due to this reason, the segmentation of facial bones depends on the quality of the CBCT dataset and the experience of the observer who performs the segmentation. Manual segmentation is a time consuming global thresholding method, with which, the result of the segmentation depends on the selected value or several values by HU and is not accurate. Therefore, an automatic and objective method is needed to perform fast and accurate segmentation of facial bones.

2.9 Summary of the methods for facial bones segmentation

Manual segmentation is the most accurate method currently used in practice. Habitually, in order to create a ground truth (reference) model for comparative assessment, manual slice-by-slice segmentation is applied. However, manual segmentation is usually tedious and time consuming. The result of 3D segmentation depends on the experience of the operator.

Global thresholding is the most commonly used method in clinical practice. It is a fast method. The results of 3D segmentation depend on the quality of the dataset. Global thresholding is implemented by the same threshold value over the entire dataset. However, the density/quality of facial bones is different. For this reason, accurate 3D segmentation of all facial bones by the global thresholding method is difficult to implement.

Segmentation by the edge requires that the specialist should have a parameterized model created by an experienced operator. The accuracy of 3D segmentation depends on the training set and on the quality of the dataset. Segmentation by edge is more applicable for 2D segmentation. Also, segmentation by edge is sensitive to noise in the image.

3D segmentation by region growing allows accurate 3D segmentation to be performed. The main difference between the region growing and the global thresholding methods is the ability to perform segmentation more locally by using

the region growing method. This means that the segmentation result does not depend on a single value. However, the region growing method is sensitive to artefacts and noise. It works most accurately when there is a strong contrast between the region being extracted and the background. For this reason, the use of the region growing method for the facial bones segmentation in CBCT datasets is complicated, and it does not provide a way to obtain an accurate 3D segmentation result.

2.10 Conclusions of the chapter

1. The automatic methods for facial bones segmentation showed promising results and the possibility of applying them in clinical practice after certain improvements. The main disadvantages of the reviewed automatic segmentation methods are the long implementation of the segmentation, the methods were tested or trained with a limited amount of data (by using CNN), or there was limited variability of the CBCT datasets. More reliable methods are needed for clinical practice in order to perform accurate, objective, and automatic segmentation.
2. The imaging technology of CBCT is important and useful in clinical practice, however, it has important limitations due to the drawbacks of the scanning technology. These limitations have influence on the quality of the images, and, consequently, on the quality of segmentation.
3. The density of facial bones expressed by HU can be wide [0–1250 HU], and the boundary between the facial bones and the background are not clear. For these reasons, segmentation of facial bones becomes more complicated.

When summarizing the findings from literature, the objectives for the study are: 1) to investigate the distribution of voxels in the preoperative and postoperative CBCT datasets by HUs. It is very important to evaluate what are the main differences between the CBCT datasets obtained before (one week) and after (up to one week) the orthognathic surgery. According to the performed literature review, 2) to develop an automatic method for the segmentation of facial bones in a CBCT dataset which reduces the operator's influence on the segmentation result. In addition, automatic segmentation could save the operator's (surgeon, orthodontist, etc.) time in performing the virtual surgical plan and evaluating the condition of the facial bones. It is thus necessary 3) to determine the parameters of the developed method that control the quality of segmentation, and 4) to investigate and evaluate the efficiency of the proposed method for the segmentation of facial bones when using clinical CBCT datasets.

3 EXPERIMENTAL INVESTIGATION OF CBCT IMAGING LIMITATIONS AND DETERMINATION OF A REFERENCE SCANNING SYSTEM

In relation to the previous studies discussed in Chapter 2, it has been determined that CBCT images are noisier than the traditional CT images. Also, the density of the facial bones by HU is within a fairly wide range. There is no clear threshold that can separate the bone area from the soft tissue. Only an experienced physician is able to analyze a CBCT dataset and select the appropriate threshold. This chapter presents the results of experimental investigation performed with the aim to determine the spatial resolution of a CBCT device (i-CAT FLX V17, Imaging Sciences International, USA) (142) used in the dental practice and in the further study. Also, the reference scanning system evaluation is presented. The result of the reference scanning system gives an opportunity to accurately evaluate 3D segmentation results.

3.1 Evaluation of spatial resolution of CBCT device i-CAT FLX V17

The spatial resolution of the system is defined as the ability to visualize and distinguish small objects. Low spatial resolution results in the blurred and enlarged edges of regions in images thus directly affecting the accuracy of the measurements. The spatial resolution of a CBCT system is determined by many factors, such as the detector element size, the focal spot size, the reconstructed voxel size, and a smoothing filter (143).

Experimental *in vitro* investigation of CBCT device i-CAT FLX V17 used for scanning in the private clinic of Orthognathic Surgery of Simonas Grybauskas was performed. The experiments presented in this chapter were performed while maintaining acquisition parameters close to the default settings used in routine clinical CBCT scanning of the patient's head before and after orthognathic surgery. The acquisition parameters of CBCT are presented in Table 3.1.

Table 3.1. Acquisition parameters of CBCT

Tube voltage (kV)	120
Tube Current (mA)	5
X-ray source to sensor distance (mm)	71.4
Exposure time (s)	7
Degrees of rotation (º)	Single 360 degree rotation
Detector array size	768 (rows) × 768 (columns)
Cone angle (º)	±10
Reconstructed matrix size	768 × 768 × 576
Reconstructed volume size (mm)	230 × 230 × 173
Reconstructed voxel size (mm)	0.3 × 0.3 × 0.3
Reconstruction algorithm	FDK

After CBCT scanning, reconstructed datasets were exported in the DICOM (digital imaging and communications in medicine) format. The obtained CBCT datasets consisted of 567 reconstructed images in the axial view, 768 reconstructed images in the coronal view, and 768 reconstructed images in the sagittal view.

For the spatial resolution, a dry mandible from Lithuanian University of Health Sciences (LUHS), Institute of Anatomy was used. The experimental setup is presented in Figure 3.1.

Fig. 3.1. Dry mandible and mandible immersed into a degassed distilled water tank prepared for scanning with CBCT

The investigation was performed in two stages. Firstly, only the dry mandible was scanned with CBCT, and, secondly, the dry mandible was immersed into a degassed distilled water tank and scanned with the same acquisition parameters of CBCT. The positioning of the mandible in each stage was the same: the mandible was centered and was facing straight forward. Figure 3.2 presents a few images obtained during the investigation.

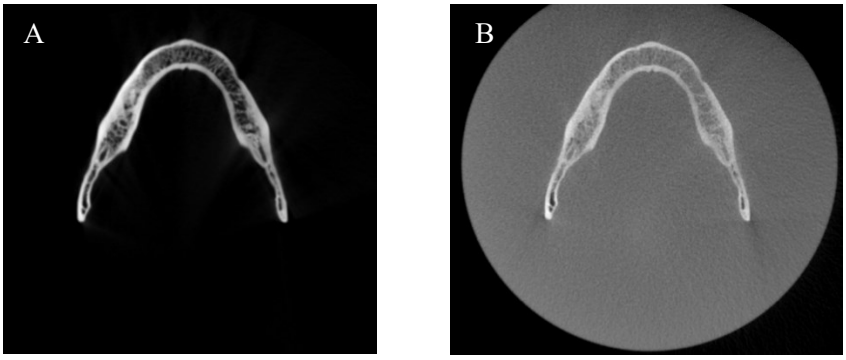

Fig. 3.2. Axials views of reconstructed CBCT images (A – mandible scanned without water, B – immersed into distilled water)

Distilled water was used to imitate the properties of a soft tissue. The spatial resolution was evaluated at full width at half maximum height (FWHM) of the line spread function (LSF). The calculation of LSF begins with the determination of the

region of interest (ROI). The ROI was determined at the same axial slice of both (A and B) obtained CBCT datasets. Accordingly, the B CBCT dataset was superimposed by the A CBCT dataset. The voxel-based technique was used for the implementation of superimposition (89). The position of the B CBCT dataset was changed by the A CBCT dataset. ROI was determined as the buccal shelf region of the mandible (Fig. 3.3).

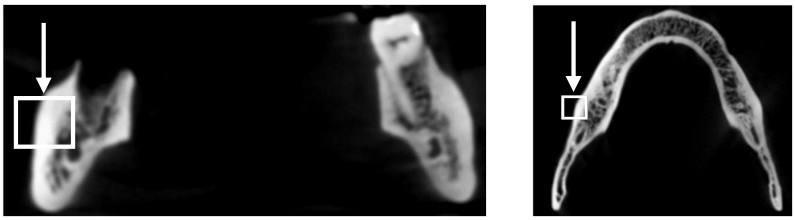

Fig. 3.3. A – coronal slice, B – axial slice of CBCT dataset with determined ROI (the buccal shelf region)

This anatomical region was selected for its anatomical features. The cortical bone thickness is the greatest (144), and the contrast between the soft tissue and the bone is the most obvious in CBCT images. The ROI was 16 × 16 pixels. Then, the pixels were averaged along the y-direction in order to obtain the edge spread function (ESF) profile of the pixel values. The averaged ESF curve is then differentiated so that to obtain the LSF curve. Next, the LSF curve was zeroed and normalized. The results are presented in Figure 3.4.

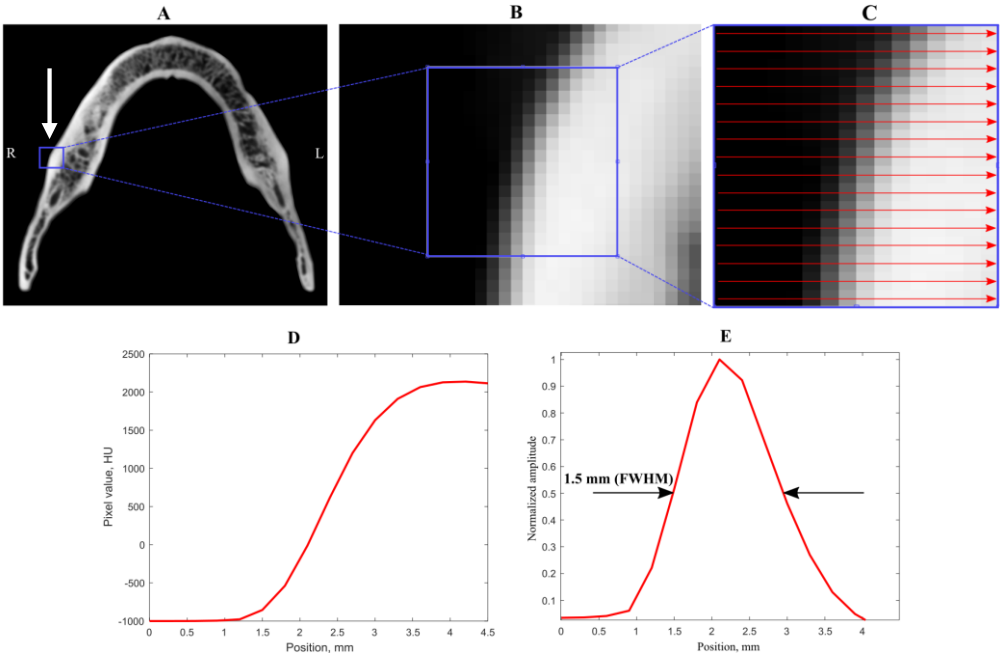

Fig. 3.4. Processes for calculating FWHM. A – axial slice of CBCT dataset. B – determined ROI, C – projections used to calculate ESF, D – calculated ESF, E – calculated and normalized LSF

By the calculated FWHM, the spatial resolution was approximately 1.5 mm. It is a 3-times lower resolution in comparison with the theoretical resolution (0.3 mm) of the CBCT device in use in this research. The same procedure was performed in order to calculate the spatial resolution when the dry mandible was immersed into distilled water. The results are presented in Figure 3.5.

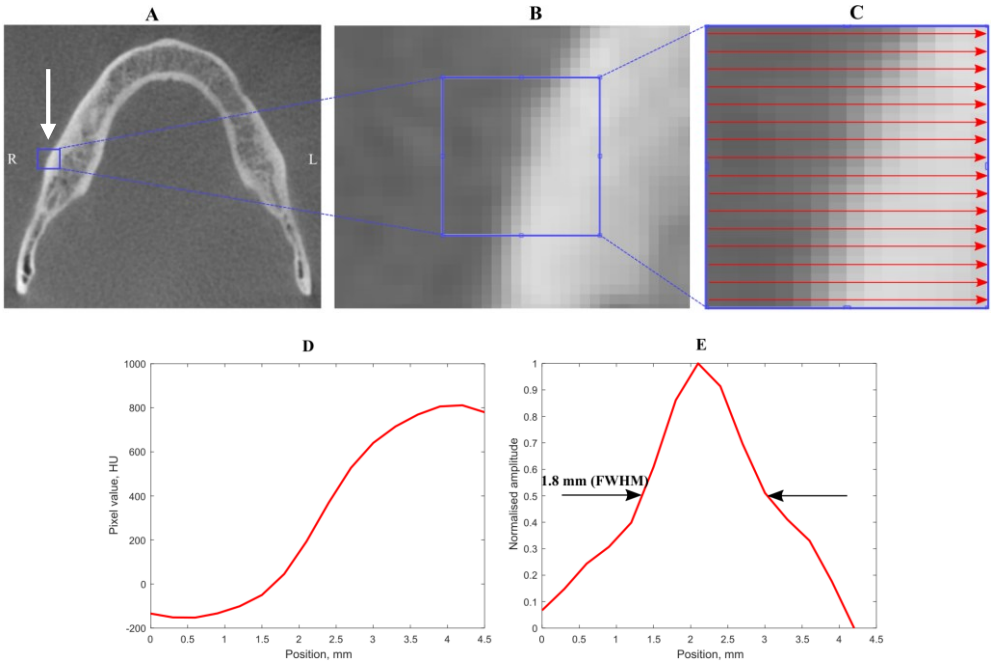

Fig. 3.5. Processes for calculating FWHM. A – axial slice of CBCT dataset. B – determined ROI, C – projections used to calculate ESF, D – calculated ESF, E – calculated and normalized LSF

The spatial resolution decreased by approximately 0.3 mm. Distilled water had an effect on the absorption of X-rays. Distilled water affected the spatial resolution. It corresponds to about one pixel.

The investigated spatial resolution of the CBCT device (i-CAT FLX V17) is about 5–6 pixels in the selected ROI. However, the spatial resolution could be affected and reduced in *in vivo* researches. A larger number of anatomical regions (muscles, skin, fibers, saliva, etc.) are involved in real clinical situations. In addition, the bone density is not the same in different areas of the mandible. For these reasons, the edge between the bone and the soft tissue is not clear and sharp. This also affects the quality of 3D segmentation.

3.2 Evaluation of the reference scanning system

The same dry mandible was used to determine a reference scanning system. The reference scanning system is required to obtain a reference 3D model. By the reference 3D model, the results of segmentation can be evaluated more accurately.

From this point of view, the use of a coordinate measuring machine (CMM) was chosen due to the possibility of accurate 3D measurement. In order to obtain a true linear measurement value when using CMM, 3 reference balls were attached to the mandible, and 3 linear measurements – AB, BC, and AC – between the balls were performed (Fig. 3.7). *Mitutoyo Crysta Apex S* (Mitutoyo America Corporation, USA) (145) was used in this research. The declared accuracy of CMM is defined as the maximum permissible error (MPE): (1.7+3L/1000) μm. 1.7 μm is the maximum permissible probing error. L is the selected measuring length (in mm). The flowchart of all the research is presented in Figure 3.6.

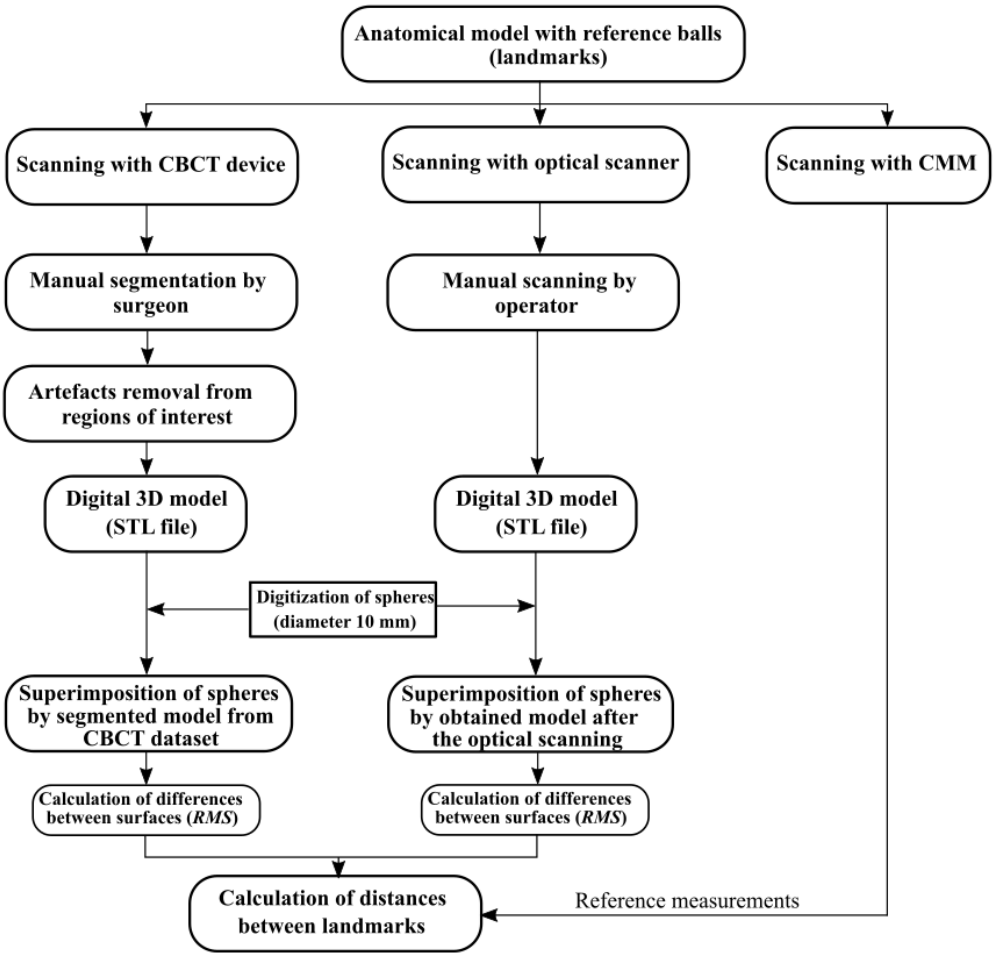

Fig. 3.6. Flowchart of research in order to determine the most accurate scanning system

Three reference balls were put on the top of the left and right condyles and at the center of mandibular incisors. This triangle is established as the Bonwill's triangle (146) (Fig. 3.7).

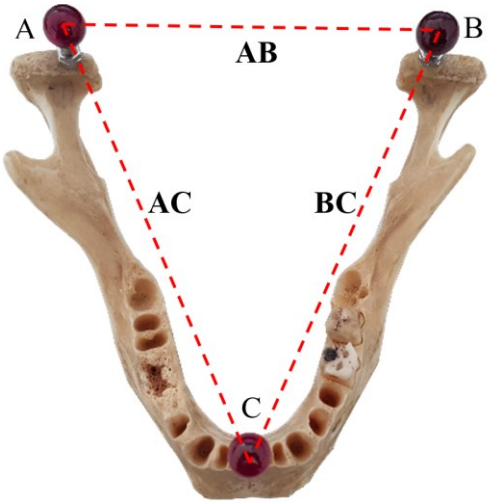

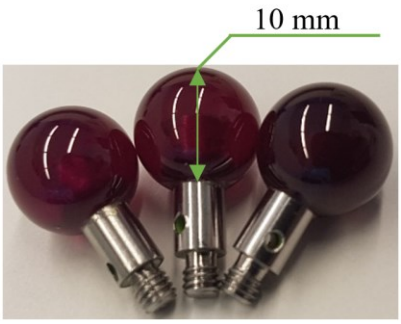

Fig. 3.7. Prepared mandible with reference balls (diameter of spheres – 10 mm) for measurements

After CMM measurements, the mandible with reference balls was scanned optically – by using a handheld optical scanner *Handy Scan 700* (Creaform, USA) (147). The declared accuracy of the scanner is 30 μm, the volumetric accuracy is 20 μm + 60 μm/m. First of all, the portable optical scanner was calibrated according to the protocol of the selected manufacturer. Scanning was performed by one experienced user. The digital 3D model was saved in the stereolithography (STL) file format (Fig. 3.8).

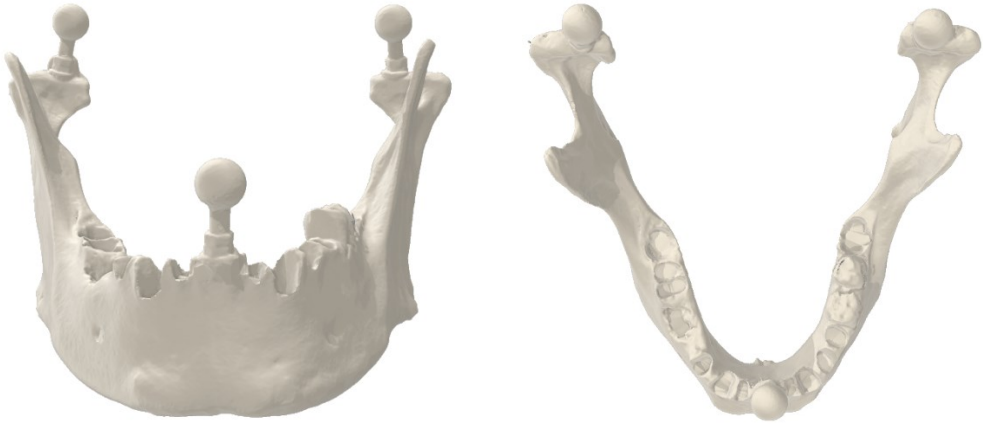

Fig. 3.8. 3D model obtained after optical scanning

The achieved result showed a high visual quality of the digital 3D model by using optical scanning.

The same anatomical model with the reference balls was scanned with a CBCT device (i-CAT FLX V17). The acquisition parameters of CBCT were the following: the size of an isotropic voxel – 0.3 mm, FOV was 230 mm × 170 mm, the

time of exposure was 7 s, the tube voltage was 120 kV with the tube current 5 mA. The selected acquisition parameters were used the same as in the usual scanning of the patient's head before or after the orthognathic surgery. The anatomical model was segmented manually by one experienced surgeon. However, in the place of reference balls, metal artefacts (the red arrows) and geometrical distortions were obtained and were seen after the initial (the global segmentation method was applied) segmentation (Fig. 3.9).

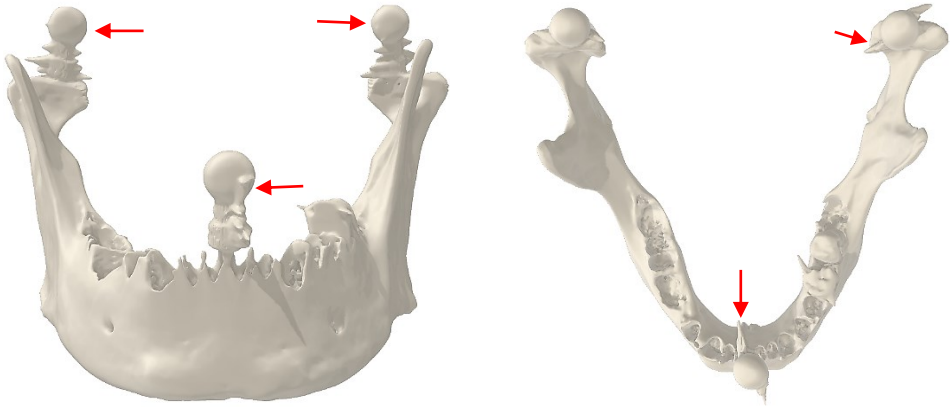

Fig. 3.9. Segmented anatomical model from different points of view (CBCT dataset)

The surface of the segmented anatomical model was evaluated slice by slice in the original CBCT images (Fig. 3.10).

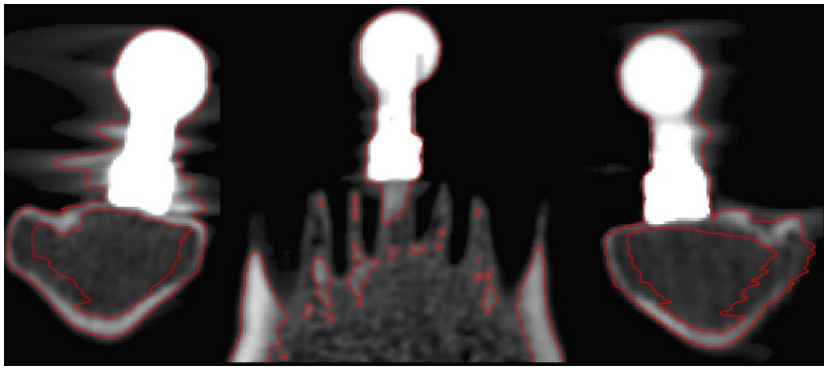

Fig. 3.10. Segmented anatomical model from different points of view (top), below – the surfaces of the segmented anatomical model and the reference balls in CBCT images (bottom)

Metal artefacts were removed manually by an experienced surgeon (Fig. 3.1). In order to increase the accuracy of measurements, three digital spheres were designed. The diameter of the digital spheres was set the same as the original spheres of the reference balls (the upper part) – 10 mm. Digital spheres were automatically superimposed by the surface-based method (148) by using *Geomagic Control X* (Version 2018.1.1, 3D Systems, USA) software (149). The results are presented in Figure 3.11.

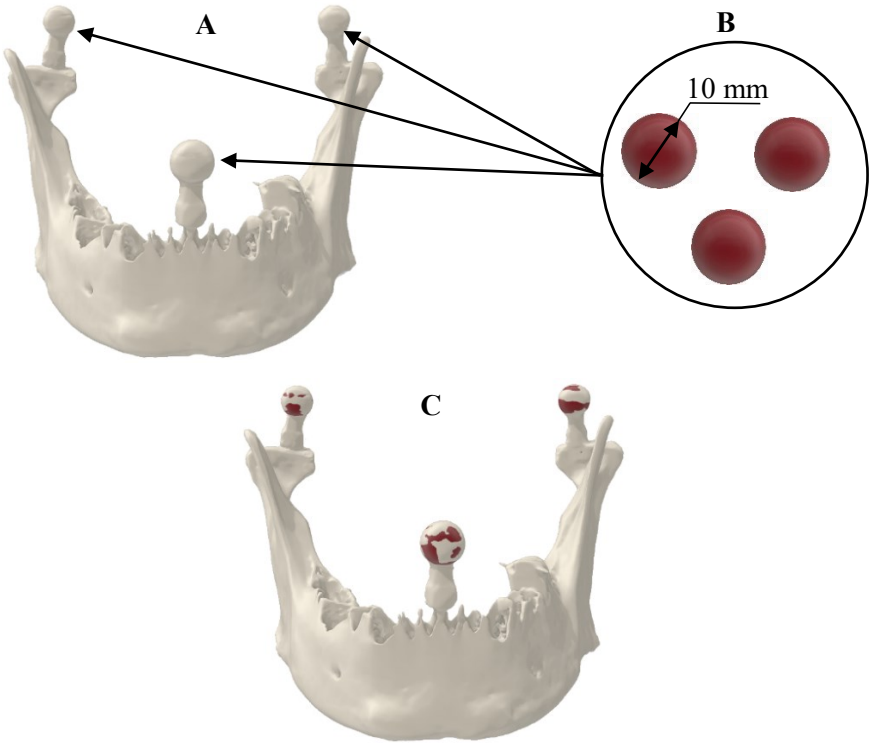

Fig. 3.11. A – Processed anatomical model, **B** – digital spheres with a diameter of 10 mm, **C** – superimposed spheres by the processed anatomical model

The differences between the superimposed surfaces were calculated. The root mean square (RMS) of the intersurface distance was used to evaluate the reconstructed outer surface mismatch.

$$RMS = \frac{1}{\sqrt{n}} \cdot \sqrt{\sum_{x,y,z=1}^{n} (a_{x,y,z} - b_{x,y,z})^2} \tag{3.1}$$

where, $a_{x,y,z}$ represents the coordinates of the optically scanned model outer surface point, $b_{x,y,z}$ – the coordinates of the outer surface point created with the proposed method, n is the number of all the points measured in each analysis.

The same workflow of research was performed with the optically scanned anatomical model and digitally created spheres. The calculated results are presented in Table 3.2.

Table. 3.2. RMS values according to differences between surfaces of spheres

Measuring body	**CBCT**	**Optical scanner**
	RMS, mm	
A	0.151	0.041
B	0.114	0.043
C	0.111	0.055

The larger intersurface distances after the superimposition were calculated between the outer surface of the segmented spheres (CBCT) and designed digitally. Compared to the results obtained with the optical scanner, the differences were about 2 times larger. The distances between the centers of the spheres were calculated. The results are presented in Table 3.3.

Table. 3.3. Distances between the centers of the spheres

Device	Distances, mm		
	AB	**BC**	**AC**
CMM (reference)	**88.278**	**107.012**	**110.867**
Optical scanner	88.397	107.046	110.890
CBCT	88.438	106.896	110.923

The achieved results showed that the 3D model obtained by optical scanning was more accurate than the 3D model segmented from the CBCT dataset. For this reason, an optical scanning system (Handy Scan 700, Creaform, USA) was used to obtain a reference 3D model.

3.3 Acquisition of optical mandible surface scans

Three mandibles (Fig. 3.12 A, B, C) from LUHS, the Institute of Anatomy were scanned with an optical scanner (*Handy Scan 700*, Creaform, USA).

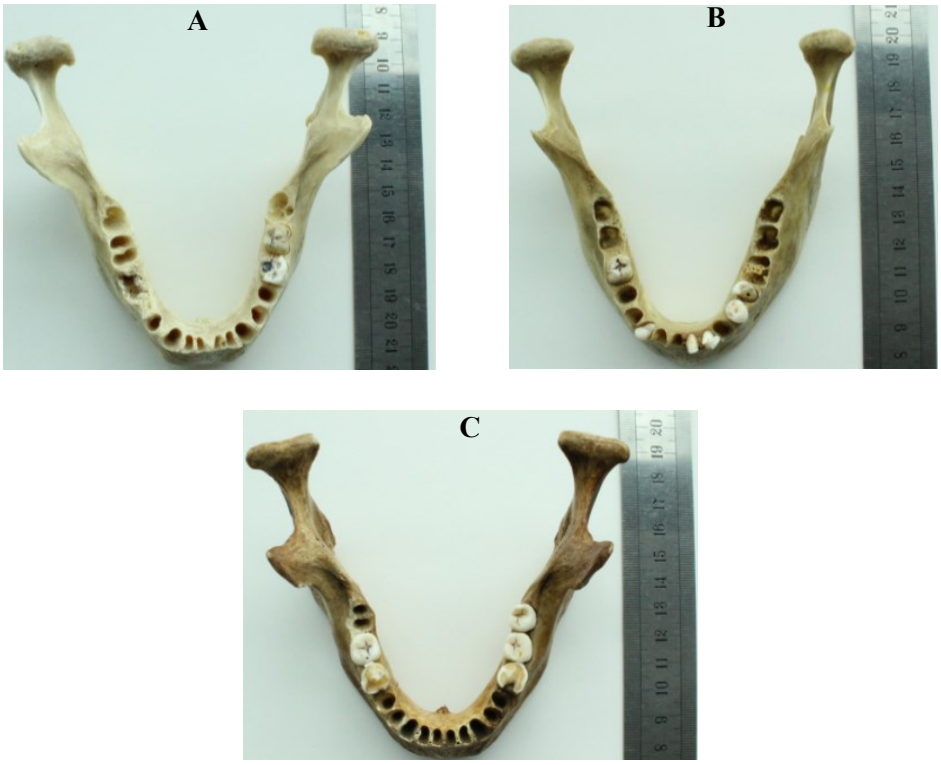

Fig. 3.12. Three mandibles (A, B, and C) prepared to scan optically

The obtained digital 3D models were saved in the STL (Standard Triangulation Language) file format (Fig. 3.13).

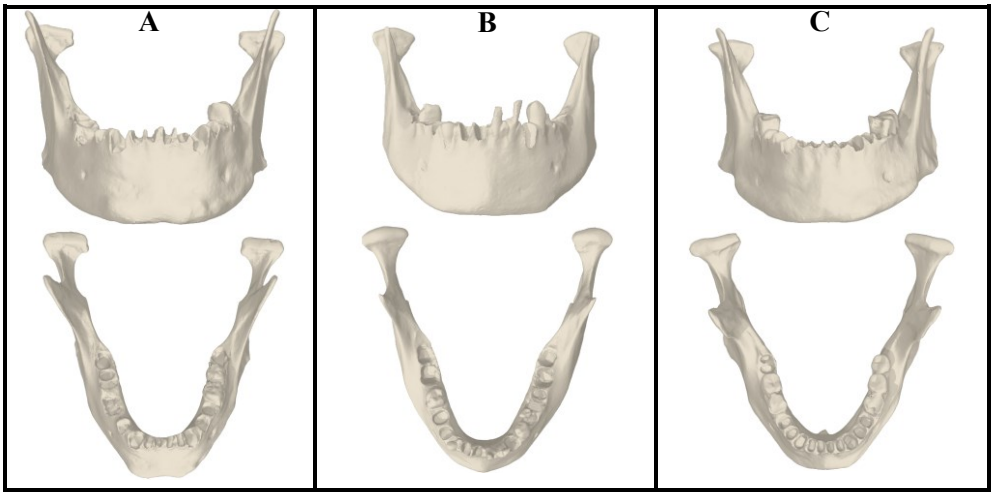

Fig. 3.13. Optically scanned mandibles from different points of view

All the scans were performed by one user on the same day.

3.4 Conclusions of the chapter

1. The investigated spatial resolution of the CBCT device (i-CAT FLX V17) is 5–6 pixels (1.5–1.8 mm) in the selected ROI (the right buccal shelf region). The obtained results showed that the 3D segmentation of a bone can be complicated. Accordingly, a more accurate scanning system is required to obtain a reference 3D model.
2. Measurements with CMM were used to determine the reference scanning system. The performed experiments showed that the outer surface of the 3D model obtained with the optical scanner was more accurate than the outer surface of the 3D model obtained by global segmentation performed in the CBCT dataset. The results of the optical scanner were twice as accurate (the mean distance error – 0.059 mm) in comparison with the results obtained with the CBCT device (the mean distance error – 0.111 mm). The results of the linear measurements also confirmed that the optical scanning system was more accurate than the CBCT. For this reason, optically scanned mandibles were used as reference 3D models in the further study.
3. Two sets of data were created during the experiments. The first set was collected as a reference. Three dry mandibles were scanned with an optical scanner. The second set was collected after scanning mandibles immersed into distilled water with the CBCT device. The acquisition parameters of the CBCT were the same as those used in the practice of orthognathic surgery.

4 PROPOSED METHOD FOR FACIAL BONES SEGMENTATION

4.1 Concept of automatic segmentation of facial bones

In this chapter, a solution of automatic segmentation of facial bones from the CBCT dataset is introduced. Based on the results of the performed literature review and the performed experimental investigation of the CBCT imaging system, the idea of automatic segmentation using locally found optimal thresholds of Otsu's method is proposed. Three main elements were used to perform automatic segmentation of facial bones: the histogram filter, Otsu's method, and the 3D sliding window.

Irrelevant anatomical regions were removed from the processed CBCT dataset by the histogram filter. The task of the filter was to limit the amount of the relevant voxels in the histogram (while leaving the voxels of the soft tissue and the facial bone). The 3D sliding window was used to find optimal thresholds by using Otsu's method in the defined volume of the processed CBCT dataset. The structure of the new automatic method for facial bones segmentation is presented in Figure 4.1.

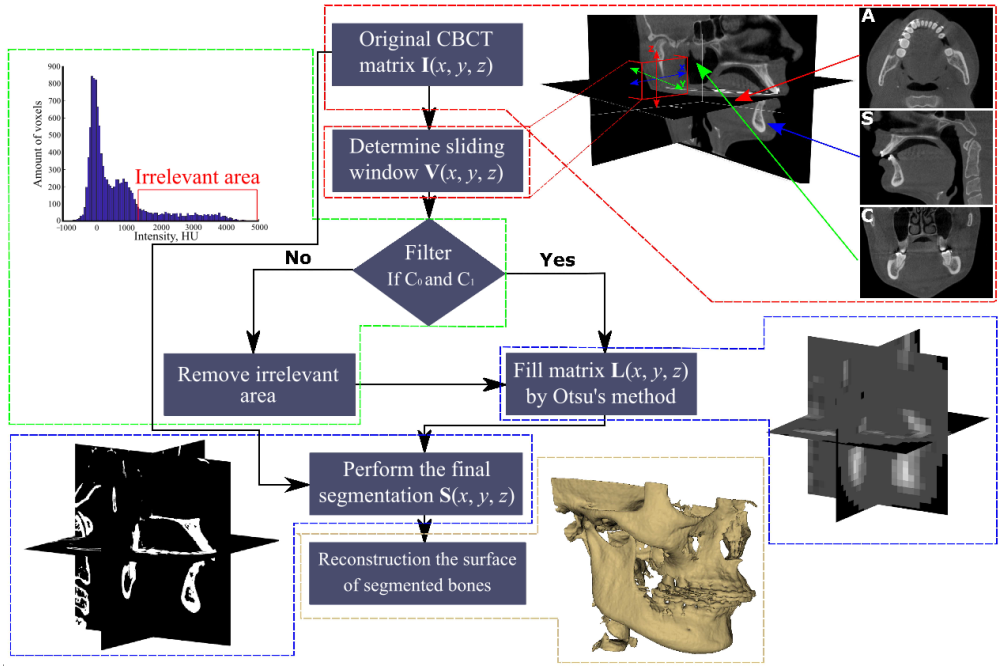

Fig. 4.1. Implementation of segmentation by using the proposed automatic method (150)

4.1.1 Analysis of CBCT histogram

Experimental data. Three mandibles were scanned with a CBCT device (i-CAT FLX V17). CBCT datasets were acquired with a resolution of an isotropic voxel of 0.3 mm, 230 mm × 170 mm FOV, the time of exposure was 7 s, the tube voltage was 120 kV, and the tube current was 5 mA. Mandibles were immersed into a clear plastic container filled with degassed distilled water. Distilled water was used

in order to simulate the properties of a soft tissue as in the previous research (Fig. 4.2).

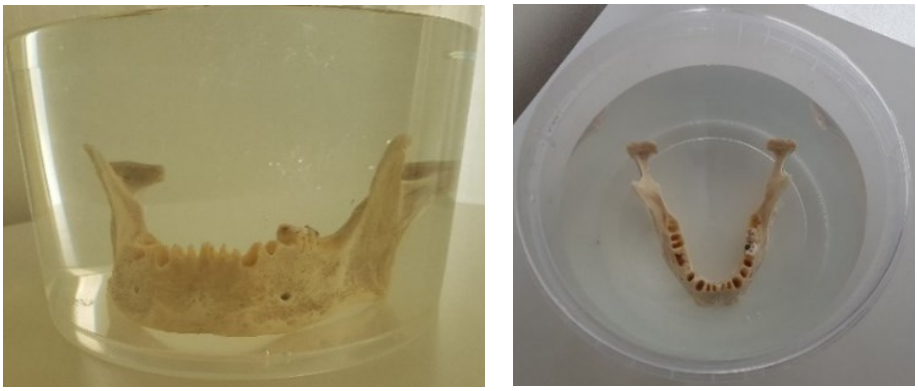

Fig. 4.2. Experimental setup for scanning with i-CAT FLX V17. The mandible is centered and facing straight forward

The size of the reconstructed CBCT dataset (**I**) which was obtained by using the selected parameters was **I** = [768(x) × 768(y) × 576(z)] voxels (Fig. 4.3).

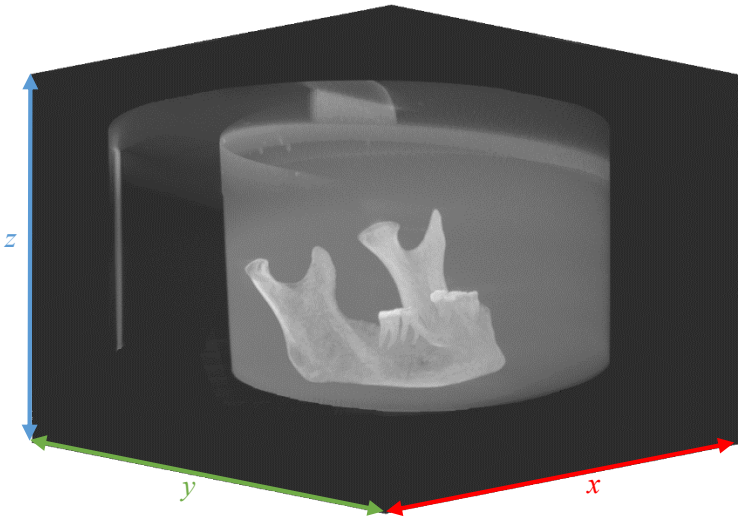

Fig. 4.3. Reconstructed CBCT dataset with the scanned mandible placed in a plastic container and filled with distilled water

The size of the reconstructed CBCT dataset depends on the selected FOV during the scanning. The used FOV was chosen in order to use the same FOV which is used during the scanning of the patient's head before or after the orthognathic surgery. The two other mandibles were scanned with the same CBCT acquisition parameters. Three CBCT datasets were obtained. The first task was to analyze CBCT histograms and to identify the main areas that make up the HU histogram of the CBCT dataset.

Results. The histograms HU distribution in the collected CBCT datasets are presented in Figure 4.4.

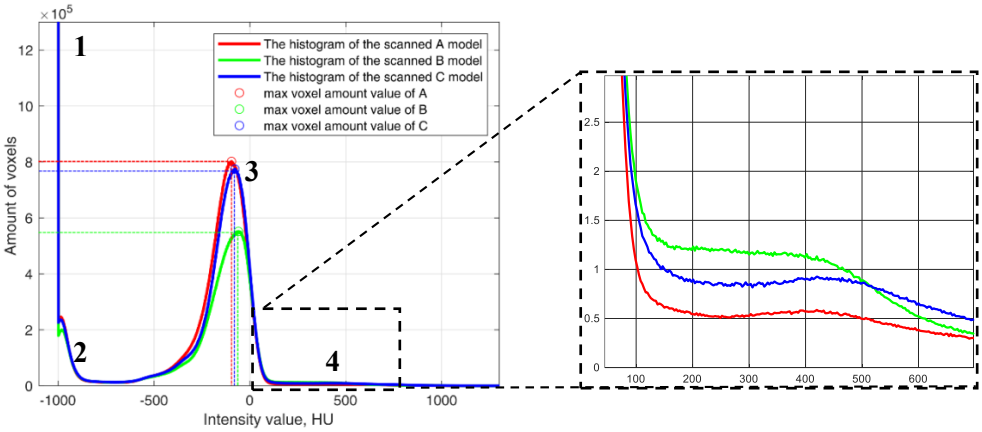

Fig. 4.4. HU distribution of CBCT histograms

The distribution of the voxels according to HU is similar when comparing different CBCT datasets. Three best expressed areas can be seen in the presented histograms. The fourth area (the bone) can be seen when it is zoomed in. Accordingly, the properties of the histogram filter were set. The lower threshold that eliminates the irrelevant anatomical areas (Fig. 4.4 **1** and **2**) is determined by Otsu's method, and the upper threshold value was chosen as the maximum value in the CBCT dataset on the grounds of the fact that the mandibles do not have metal implants and restorative materials. The 3rd and 4th areas (Fig. 4.4) were used to find the optimal threshold values.

4.1.2 Implementation of 3D sliding window for segmentation

The second task was to evaluate the influence of a 3D sliding window for the results of bone segmentation. A 3D sliding window ($\mathbf{V}(x, y, z)$) is used to make the segmentation a local. The optimal threshold values by Otsu's method were found after the filtration of the histogram in a 3D sliding window. The optimal threshold values were found after each shift ($p_{x, y, z}$) of the 3D window. The determined optimal threshold values were saved into the matrix of local thresholds $\mathbf{L}(x, y, z)$. The filled matrix $\mathbf{L}(x, y, z)$ is used to perform the final segmentation. The determined optimal thresholds $\mathbf{L}_{1+i}$ were compared with the original matrix $\mathbf{I}(x, y, z)$ voxels values, and final segmentation is performed by applying:

$$S(x,y,z) = \begin{cases} 0 & if\ I(x,y,z) < L(x,y,z) \\ 1 & otherwise \end{cases}. \qquad (4.1)$$

The 3D sliding window should increase the accuracy of segmentation. The segmentation thus becomes local (Fig. 4.5).

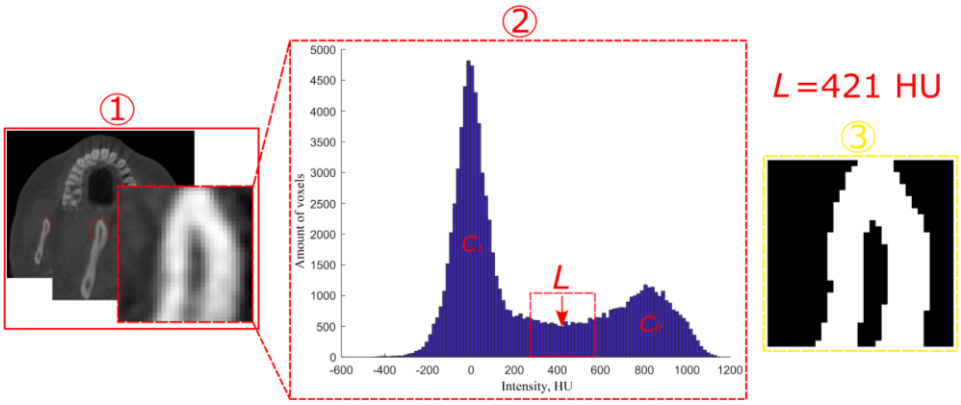

Fig. 4.5. Analysis of histogram **2** in the determined volume of sliding window **1** in order to find optimal threshold value **L** and perform the segmentation of facial bones **3** (150)

The amount of the determined optimal thresholds depends on the size of the volume and the number of shifts of the 3D sliding window. It is an important step to evaluate the influence of the 3D window on the segmentation results. The shift and the volume of the 3D sliding window were evaluated. The implementation of the 3D sliding window is presented in Figure 4.6.

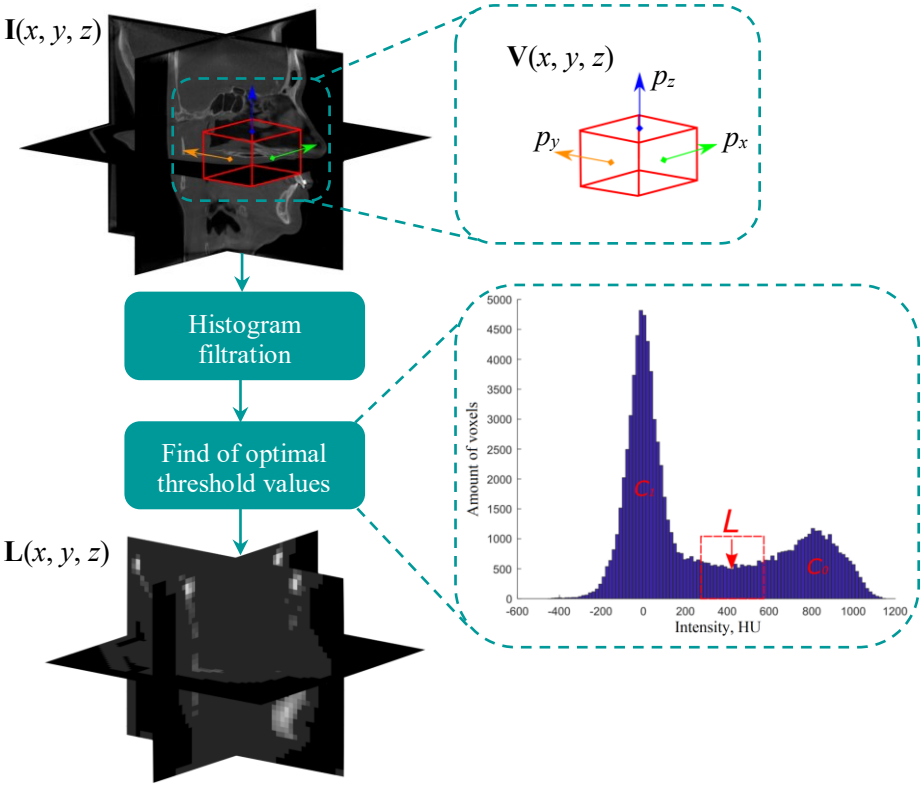

Fig. 4.6. Implementation of 3D sliding window (**V**(*x, y, z*))

The size of the reconstructed CBCT dataset (**I**) is not isotropic; however, by the maximum dimensions (d_{max} = 768 voxels) of CBCT dataset **I**, four different volumes (**V1**, **V2**, **V3**, and **V4**) were used in this research. The sizes of the volumes were isotropic (Fig. 4.7).

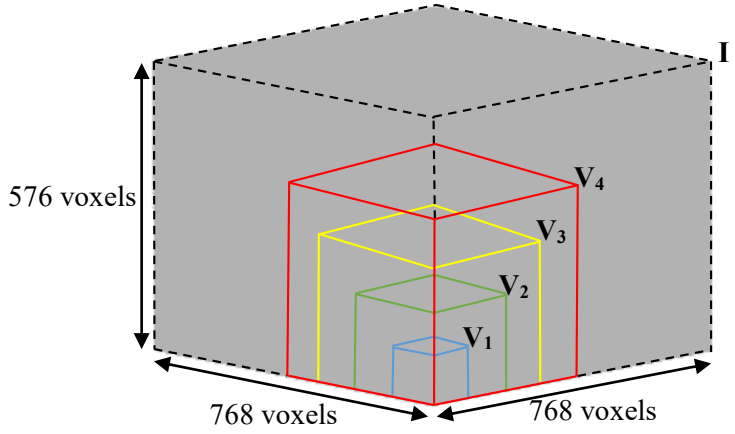

Fig. 4.7. Representation of the selected volumes of 3D window

The selected isotropic volumes of a 3D window in the research were as follows:

V1 = [96 × 96 × 96] voxel = 24 cm³ (13% of d_{max});

V2 = [192 × 192 ×192] voxel = 191 cm³ (25% of d_{max});

V3 = [288 × 288 × 288] voxel = 645 cm³ (38% of d_{max});

V4 = [384 × 384 × 384] voxel = 1529 cm³ (50% of d_{max}).

The shifts (p_x, p_y, p_z) were selected according to the size of the volume (Table 4.1).

Table 4.1. The selected shifts (in voxels and mm) to find the optimal shift of volume. **Values by millimeters (*mm*) were rounded to the nearest integer*

	Shifts (*p*)							
Volumes	10% of V		30% of V		50% of V		100% of V	
	voxels	mm	voxels	mm	voxels	mm	voxels	mm
V1	10	3	29	8	48	14	96	29
V2	19	6	58	17	96	29	192	58
V3	29	9	86	26	144	43	288	86
V4	38	12	115	35	192	58	384	115

Each volume is moved from the beginning of the original matrix **I** of the CBCT dataset. The volumes move in the *x*, *y* and *z* directions. After each segmentation, the 3D surface reconstruction of the segmented voxels was performed. The surface reconstruction is performed by the volumetric reconstruction algorithm (the Visualization and Computer Graphics (VCG) reconstruction filter) by

using the *MeshLab* free software (*Visual Computing Lab of ISTI–CNR*, University of Pisa) (151, 152). The basis of the VCG reconstruction filter is the marching cubes algorithm. The basic parameter for the reconstruction of the 3D surface is the *Voxel Side*. According to the original voxel size (0.3 mm), the *Voxel Side* was chosen equal to the original voxel size. A larger value of the *Voxel Side* may cause a 3D surface that is too smooth, whereas a smaller value of the *Voxel Side* than the original voxel size may cause a sharp, grainy 3D surface in the output (Fig. 4.8). The reconstructed 3D surfaces were saved in the STL file format.

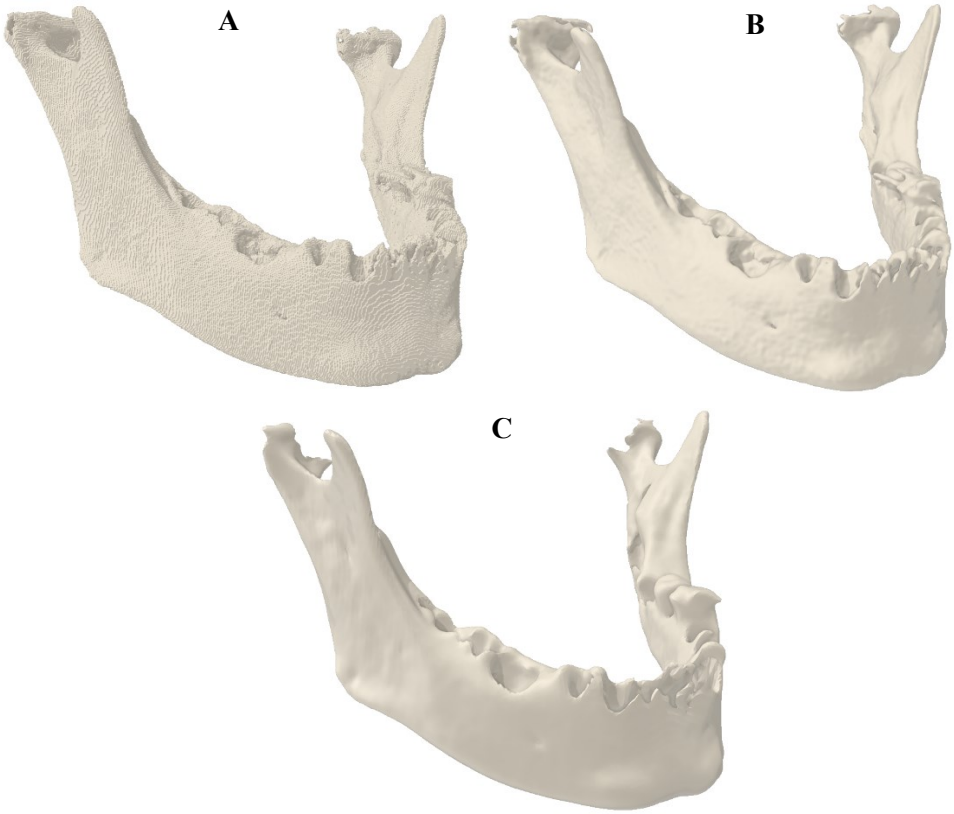

Fig. 4.8. Reconstructed surface of the mandible with different values of *Voxel Side* (A – *Voxel Side* 0.15 mm, B – *Voxel Side* 0.3 mm, C – *Voxel Side* 0.6 mm)

4.1.3 Evaluation of 3D deviation between automatically segmented and optically scanned (reference) outer surfaces

The third task was to superimpose segmented 3D models with the corresponding optically scanned 3D models. The surface-based method (148) was used for superimposition. Superimposition was implemented in the *Geomagic Control X* (Version 2018.1.1) software. After superimposition, the outer surface distances of the 3D models were calculated by RMS. The RMS value showed how two 3D outer surfaces deviated from zero. A low RMS value indicated high 3D

agreement between the two 3D model outer surfaces. The unit of measurement considered for RMS was mm.

Also, the time to perform automatic segmentation after each iteration of segmentation was calculated. The results are presented in Table 4.2.

Table 4.2. Calculated RMS values and segmentation times to evaluate the influence of the 3D sliding window on segmentation results

Models	V, cm³	Shifts, mm							
		100% V		50% V		30% V		10% V	
		RMS, mm	**Time**, s	**RMS**, mm	**Time**, s	**RMS**, mm	**Time**, s	**RMS**, mm	**Time**, s
A	**24**	0.406	9.92	0.338	30.42	0.340	101.88	0.337	1856
	191	0.479	14.54	0.403	33.04	0.368	111.31	0.366	2451
	645	0.501	18.11	0.408	43.57	0.389	118.14	0.377	2541
	1529	**↑0.502**	21.53	0.484	43.06	0.406	133.15	0.398	**↑2813**
B	**24**	0.469	9.53	0.349	23.85	0.359	91.03	0.359	1642
	191	0.413	14.17	0.454	28.38	0.431	99.68	0.426	2063
	645	0.406	15.94	0.427	32.32	0.458	101.89	0.434	2102
	1529	0.451	20.31	0.388	41.15	0.389	138.05	0.452	2165
C	**24**	0.3929	**↓8.80**	0.303	27.12	0.288	90.65	**↓0.286**	1762
	191	0.4021	11.77	0.312	29.85	0.304	109.31	0.304	2389
	645	0.4565	17.89	0.341	41.47	0.311	112.39	0.307	2444
	1529	0.3345	20.51	0.340	42.10	0.319	129.17	0.309	2455

The calculated metrics showed that the minimum values of RMS are found when the volume and shift of the 3D window is minimum; however, the computational time to perform segmentation is the longest. The biggest discrepancies between the 3D surfaces are observed when the volume and shift of the 3D window is the maximum. Despite this, the shortest computational time to perform segmentation is detected when the volume of the 3D window is the minimum, and the shift of the 3D window is the maximum. The mean RMS values of each shift and volume of the 3D window are presented in Figure 4.9.

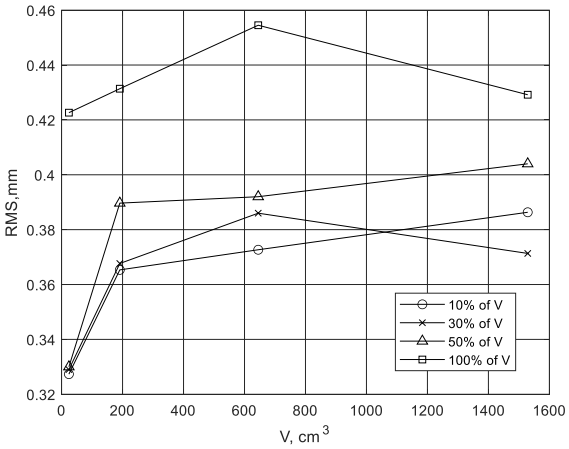

Fig. 4.9. The calculated mean values of RMS by different volumes and shifts of 3D window

The mean computing time to perform segmentations by using different volumes and shifts of a 3D window are presented in Figure 4.10. The logarithmic

scale was applied in the Time axis due to a wide range of the calculated values of time.

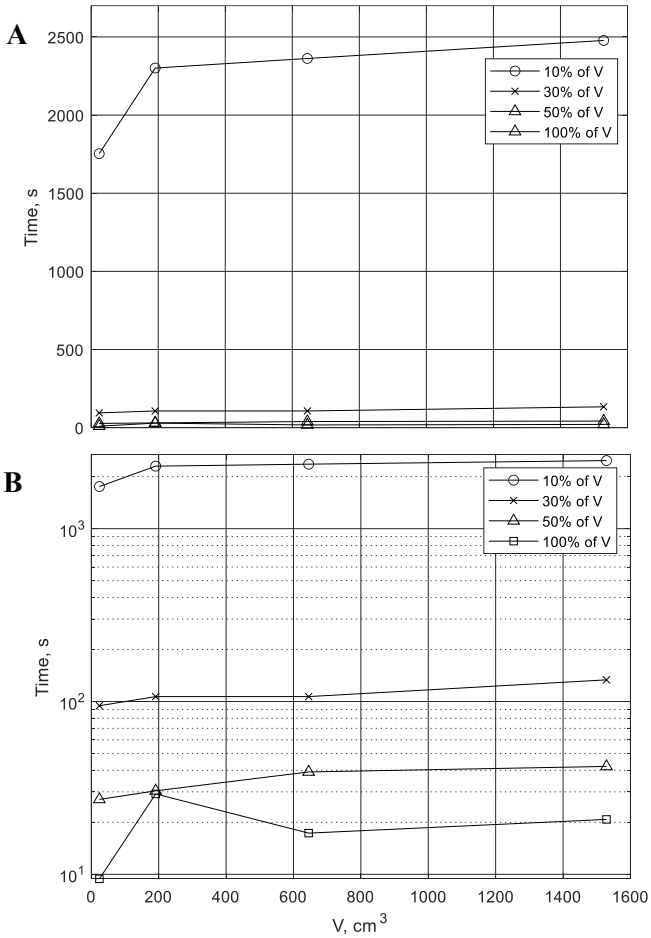

Fig. 4.10. The calculated mean computational times by using different volumes (**V**) and shifts ($p_{x,\,y,\,z}$) of 3D window. **A** – original dependency, **B** – the same dependency with the logarithmic scale

Discussion. The larger differences in the computational time are observed when the shift of the 3D window is the smallest (10% of **V)**. There is approximately a 100-times difference when comparing the computational time when the shifts are 100% of **V** with the shifts equaling 10% of **V**. The evaluation of the calculated RMS values and the computational time has shown that the optimal volume is 191 cm^3, whereas the shift is 50% of the 3D window (which is 29 mm). This decision was made by the comparison of the different calculated mean values of RMS by using different volumes and shifts of the 3D window. The differences in comparing the mean values of RMS when using different volumes and shifts were not significant, but the differences in the segmentation time when using different volumes and shifts

were significant. For these reasons, in the further study, the volume of choice was 191 cm^3, whereas the shift of 29 mm was used.

4.2 Limitations due to the reference models in use

Accurate evaluation of segmentation can be performed by using a cadaver with the soft tissue (100, 153). Dry mandibles without the soft tissue do not provide ideal conditions for evaluating the proposed method. According to the performed previous investigation, distilled water had an effect on the quality of the spatial resolution. In this research, distilled water was also used to simulate the soft tissue. In order to evaluate the proposed automatic method for bone segmentation, only the outer surface distances of the 3D models were calculated. The volumetric differences could be evaluated by using the more accurate scanning technology – micro-CT.

The limitation of this performed research is also the limited amount and variety of the research objects. For this reason, the optimal parameters of the 3D sliding window may vary depending on the size and bone density of the mandible.

4.3 Conclusions of the chapter

1. The analysis performed on CBCT histograms showed that the voxel distribution of the facial bones was not evident. Manual separation (by global thresholding) of the bone region from the simulated soft tissue region is complicated.
2. An automatic method for facial bones segmentation in the CBCT dataset was developed. The implementation of the method is based on the analysis of the CBCT histogram, the filtering of the irrelevant anatomical regions from the CBCT histogram, on the determination of the volume and shift of the 3D window, and on the application of Otsu's method serving the objective of finding the optimal threshold.
3. Experimental investigation was performed in order to evaluate the influence of the 3D sliding window on the segmentation results. Two basic parameters of the 3D window were evaluated: the volume and the shift.
4. The best repeatability of the outer surfaces of the two 3D models is achieved when the volume of the 3D window is 191 cm^3, and the shift of the 3D window is 29 mm. This selection is based on the aggregate estimation of the segmentation time and 3D deviation by calculating RMS between the automatically segmented and the optically scanned (reference) outer surfaces.

5 PERFORMANCE EVALUATION OF THE DEVELOPED METHOD

5.1 Experimental results of the analysis of CBCT histogram

Experimental data. Twenty CBCT datasets were randomly selected from Simonas Grybauskas' Orthognathic Surgery database. Ten CBCT data sets were obtained approximately one week before the surgery (preoperative), and ten – approximately one week after the surgery (postoperative). All the CBCT data sets were anonymized. CBCT datasets were acquired with a CBCT device i-CAT FLX 17 (Imaging Sciences International, USA), the FOV was 230 × 170 mm, the time of exposure was 7 s, the tube voltage was 120 kV with the tube current of 5 mA.

Results. The analysis of the CBCT histogram was performed so that to identify the main areas that make up the HU histogram of the CBCT dataset. In order to analyze the full structure of the histogram, ten randomly selected preoperative and ten postoperative CBCT datasets were used (Fig. 5.1).

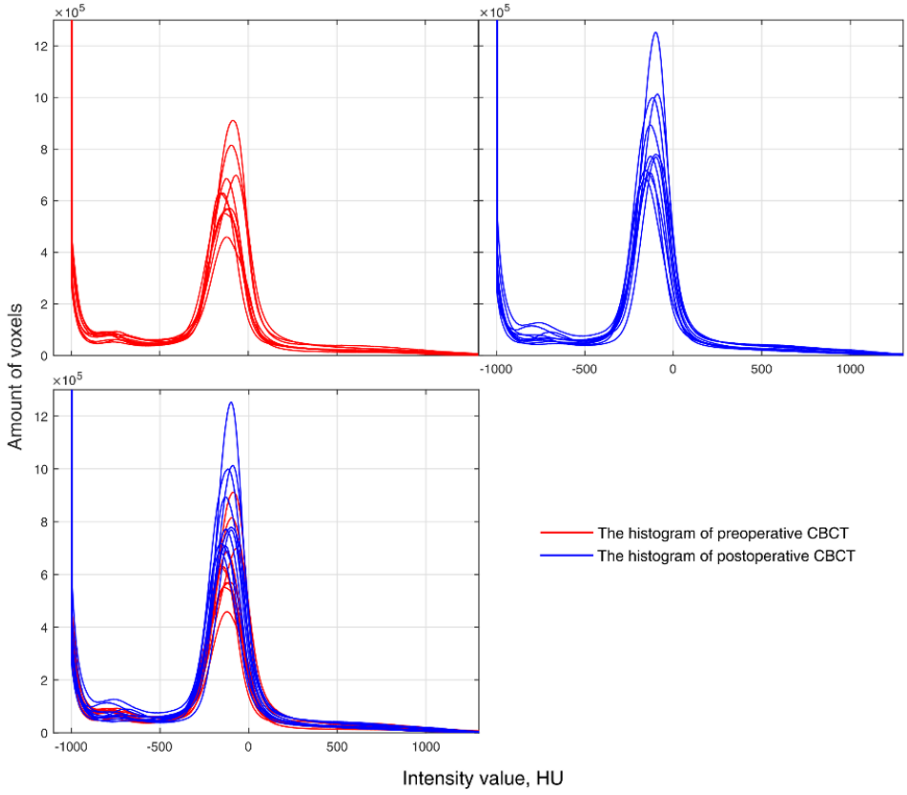

Fig. 5.1. Histograms of HU distribution in the dataset. The red color represents histograms of preoperative CBCT datasets (N=20), the blue color represents histograms of postoperative CBCT datasets (N=20).

Three most expressed areas found in histograms are: air, internal anatomical structures containing air, and the soft tissue. The bone area was not expressed well in all histograms. The clearly visible area (excluding air) was the soft tissue in

preoperative and postoperative histograms. Also, the biggest difference between these areas was seen when comparing preoperative and postoperative CBCT datasets. The statistical difference between the voxel values of the whole HU scope for preoperative and postoperative CBCT was not found (paired *ttest* was used, $p > 0.05$). Then, by comparing the distribution of HU values only in the soft tissue, the statistical difference between the preoperative and the postoperative cases was found (paired *ttest* was used, $p < 0.05$). The amount of voxels was bigger for the postoperative cases in comparison with the amount of voxels in the area of the soft tissue for the preoperative cases. It was determined that the soft tissue was more swollen after the surgery. The mean shape, structure and relation to the anatomic areas of the summarized investigated histogram is presented in Figure 5.2.

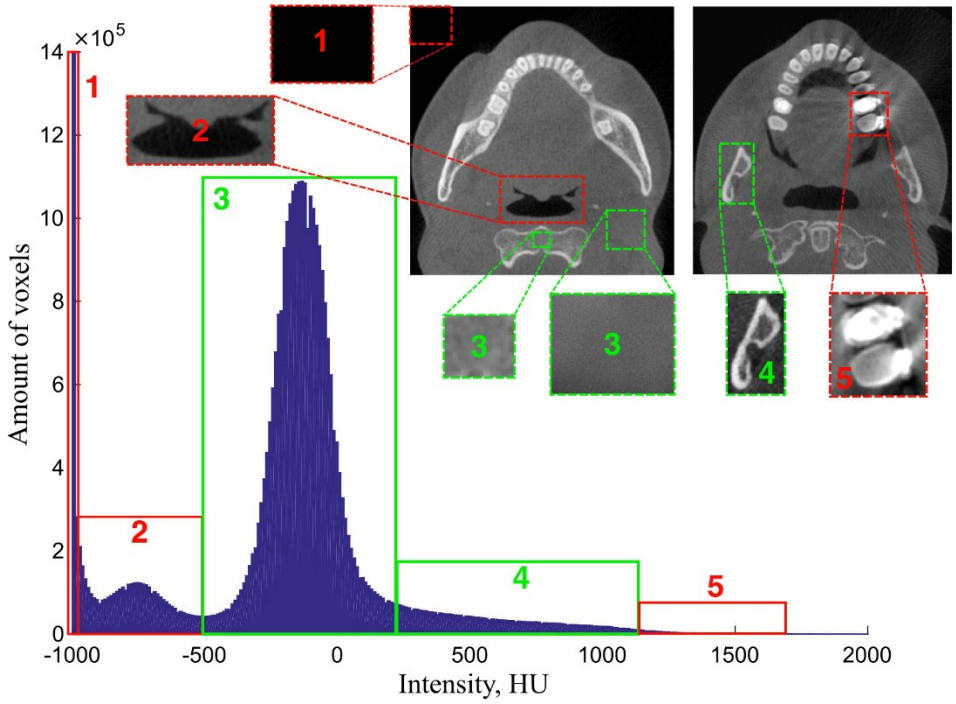

Fig. 5.2. The mean histogram of investigated CBCT datasets (150)

Discussion. When evaluating the reviewed studies (135 – 141) along with the presently performed study, the full structure of a histogram can be divided into the following basic areas: air (Fig. 5.2. – area 1), the internal anatomical structures containing air (Fig. 5.2. – area 2), soft tissue/tuberosity areas (Fig. 5.2. – area 3), facial bones (including the cortical bone, the trabecular bone of the mandible and the maxilla) (Fig. 5.2. – area 4), and metal artefacts and restorative materials (Fig. 5.2. – area 5). However, the distribution of the facial bones voxels and metal artefacts voxels are not Gaussian on a histogram. Only the second and third areas form Gaussian distribution.

In this research, the region of interest is the area of facial bones. By the performed literature review (135 – 141), the voxels intensities distribution of the facial bones in CBCT datasets is relatively wide [0–1250 HU]. In each CBCT dataset, the threshold value can be different. It depends on whatever kind of the CBCT device was used, what is the quality of the bone, etc. For these reasons, the boundary between the soft tissue and the facial bones is not clearly defined. The position of the dashed line in Figure 5.3 can be different in each individual case. Also, an automatic method (Otsu) cannot work accurately when seeking to find the optimal threshold value. However, Otsu's method can be applied to find two optimal thresholds. The first threshold separates the soft tissue from the internal anatomical structures containing air. The second threshold separates the internal anatomical structures containing air.

5.2 Filtration of CBCT histogram

According to the previously presented idea, Otsu's method was used to find two optimal thresholds. The determined thresholds were used for the filtration of the irrelevant anatomical areas from the CBCT histogram. The third threshold was selected based on the findings of the performed literature review. The value of the third threshold was selected to be 1250 HU as justified by the study performed by Misch (135).

The purpose of the filter is to make the analyzed CBCT histogram bimodal. The filtered histogram is presented in Figure 5.3.

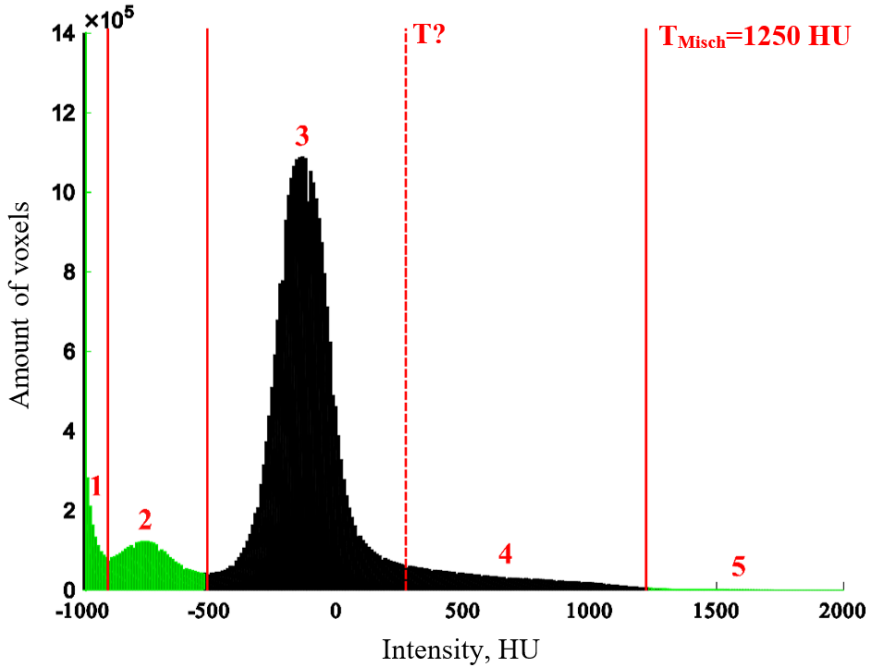

Fig. 5.3. Filtered histogram (the areas selected by the green color were filtered). The one good expressed area (3) is seen after filtration

However, the finding of optimal threshold value after filtration is still complicated. Just one good expressed area (the soft tissue) in the histogram is seen. The overlap of the voxels intensity between the facial bones and the soft tissue is possible. Due to this reason, the reduction of the analyzed volume was used in order to find the optimal threshold value only in the determined volume. In order to segment all the object, the 3D sliding window was used for the implementation of this idea.

5.3 Experimental results of facial bones segmentation

Experimental data. A retrospective study was performed by using forty CBCT datasets from the database of the Orthognathic Surgery clinic of Simonas Grybauskas. Before the study, all the CBCT datasets were anonymized in order to protect the patients' data. Half of them (n = 20) were preoperative (obtained one week before the surgery), whereas the other half (n = 20) were postoperative (obtained about one week after the surgery) scans of the same patient group. All the scans were done by using the i-CAT FLX V17 (Imaging Sciences International, USA) scanner. All the patients undertook double jaws correction. CBCT datasets were acquired with the resolution of an isotropic voxel of 0.3 mm, 230 mm × 170 mm field of view (FOV), the time of exposure was 7 s, the tube voltage was 120 kV, and the tube current was 5 mA. The study framework is presented in Figure 5.4.

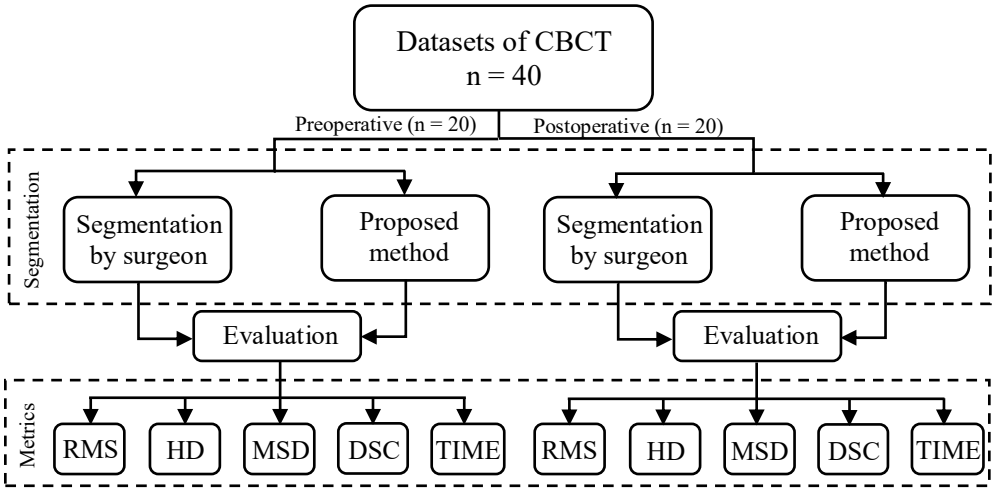

Fig. 5.4. The framework of the current study. The study was performed by using preoperative and postoperative CBCT datasets. Five metrics RMS, HD, MSD, DSC, and computational Time were used to evaluate the efficiency of the proposed method

Performance evaluation. Preoperative and postoperative CBCT datasets were segmented by an experienced oral and maxillofacial surgeon using *ITK-SNAP* software (Version 3.4.0) (154) by selecting the global threshold value for each case individually. The mandible and the lower parts of the skull (including the maxilla, the zygomatic bone) were used to perform the segmentation. Therefore, the above mentioned anatomical regions were selected as the segmentation target while

assessing their importance with regard to the surgery. In order to evaluate the reliability of the surgeon's segmentation, the segmentations were done twice within a two-week interval. For the quantitative evaluation of the reliability, the *Intraclass Correlation Coefficient* (ICC) was used with the two-way mixed model, unit: the single rater and the type of relationship: the absolute agreement method (155) was calculated by:

$$ICC = \frac{MS_R - MS_E}{MS_R + (K-1)MS_E + \frac{k}{n}(MS_C - MS_E)}, \tag{5.1}$$

where, MS_R = mean square for rows, k = number of raters/measurements; MS_E = mean square for error; MS_C = mean square for columns; n = number of subjects. ICC was calculated separately for the preoperative and postoperative cases, and the segmentation thresholds as selected by the surgeon were used for this step. The interpretation of ICC could be defined, and the values lower than 0.5 are indicative of poor reliability, the values between 0.5 and 0.75 indicate moderate reliability, the values between 0.75 and 0.9 indicate good reliability, and the values greater than 0.90 indicate excellent reliability (155). The calculated values of ICC are provided in Table 5.1.

Table 5.1. Results of *Intraclass Correlation Coefficient* (ICC) when using single rater, absolute agreement and 2-way random effects model

	Intraclass Correlation	95 % Confidence Interval		F Test with True Value 0			
		Lower Bound	Upper Bound	Value	df1	df2	Sig
Single measures preoperative	0.985	0.896	0.983	49.03	19	19	0.000
Single measures postoperative	0.931	0.836	0.972	27.43	19	19	0.000

The results show that, in the preoperative data, ICC = 0.958 with 95% confidence interval [0.896 ... 0.983], whereas, in the postoperative data, ICC = 0.931 with 95% confidence interval [0.836 ... 0.972]. The calculated values of ICC show that the level of surgeon reliability is sufficient.

Facial bones segmented by the surgeon were used as reference 3D models in order to evaluate the results achieved by the proposed automatic segmentation.

For the evaluation of the proposed method, five kinds of metrics were used. Based on the intersurface distance evaluation, RMS, Hausdorff distance (HD), and the mean distance were calculated.

1) The RMS of the intersurface distance was used to evaluate the reconstructed surface mismatch (Equation 3.1).

2) The Hausdorff distance (HD) was calculated by:

$$HD = (A, B) = \max\{h(A, B), h(B, A)\}, \tag{5.2}$$

where, $h(A,B)$ stands for the direct Hausdorff distance:

$$h(A,B) = \max_{a_{x,y,x} \in A} \left\{ \min_{b_{x,y,z} \in B} \|a - b\| \right\}, \tag{5.3}$$

3) The mean intersurface distance (MSD) was calculated by:

$$MSD = \frac{1}{N} \cdot \sum_{i=1}^{n} \left(a_{x,y,z} - b_{x,y,z} \right). \tag{5.4}$$

Positive and negative MSD values were calculated as well.

Based on the volume overlap, it is common to use the Dice similarity coefficient (DSC) to measure the proposed automatic segmentation reproducibility (repeatability) (2).

4) DSC was calculated by:

$$DSC = \frac{2|A \cap B|}{\left(|A| + |B|\right)}, \tag{5.5}$$

where, A represents the volume of the reference model, B is the volume of the automatically segmented bone.

An additional metric was calculated to evaluate the speed of segmentation (Time). In this study, a personal computer with the following parameters: processor – Intel(R) Core(TM) i7-4790 CPU @ 3.60 GHz, RAM – 16 GB, system type – 64-bit Windows 10 Operating System was used. The automatic method was implemented by using the *Matlab* (license number – 40875229, Mathworks, USA) software.

The implementation of the proposed method was based on the finding of the optimal threshold by using Otsu's method in a sliding 3D window. The volume (**V** = 191 cm^3) and the shift ($p_{x,\,y,\,z}$ = 29 mm) of the window were set based on the research results with anatomical models as described in the previous chapter.

First of all, each processed histogram of the CBCT dataset was analyzed in order to automatically find thresholds for the filtration of irrelevant areas (air and internal anatomical structures containing air). Otsu's method was applied to implement it. The upper threshold (>1250 HU) for the filtration was selected by using data from Mitch *et al*. (135) classification.

During the second step, the optimal threshold values were found locally in the determined volume of the 3D window after each determined shift. The optimal thresholds were found by Otsu's method.

During the third step, the matrix of local thresholds **L**(x, y, z) was filled in.

Finally, the surface reconstruction of the segmented voxels of facial bones was performed. Segmented facial bones are saved as a surface in the STL file format. The surface reconstruction of facial bones from segmented voxels is performed by the volumetric reconstruction algorithm (Visualization and Computer Graphics (VCG) reconstruction filter) while using the *MeshLab* software (Visual Computing Lab of ISTI–CNR, University of Pisa) (Fig. 5.5).

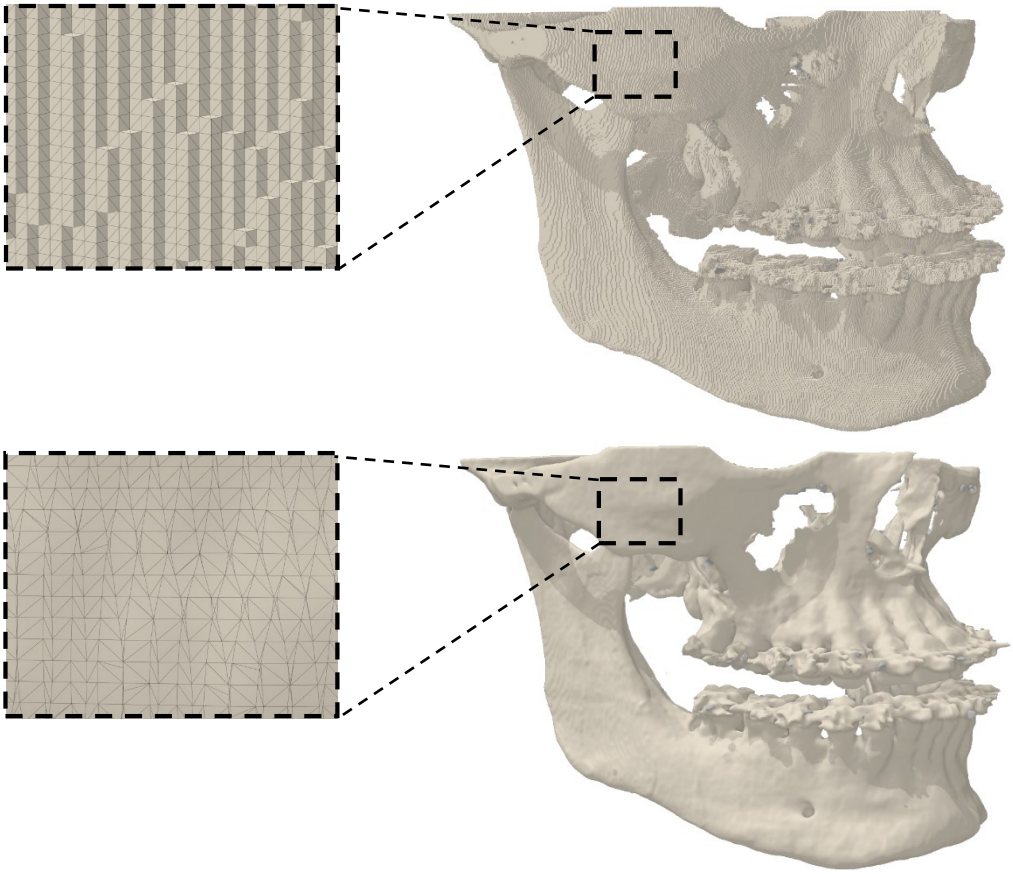

Fig. 5.5. Surface reconstruction of segmented facial bones. The surface of facial bones after segmentation (at the top), the reconstructed surface of facial bones (at the bottom). Small fragments of surfaces before and after reconstruction are presented in rectangles

For the basic parameters of surface reconstruction, the same values (the voxel size, the level of the subvolume reconstruction process, geodesic weighting, the number of Volume Laplacian iterations, widening, the number of smoothing iterations) were used for all the forty cases in order to obtain comparable results of reconstruction.

Results. The mean RMS value of the intersurface distance in preoperative cases was 0.559 (SD ± 0.099) mm, whereas, in the postoperative cases, this value

was 0.647 (SD ± 0.175) mm. The calculated RMS values of the intersurface distance for all the cases are presented by a boxplot in Figure 5.6.

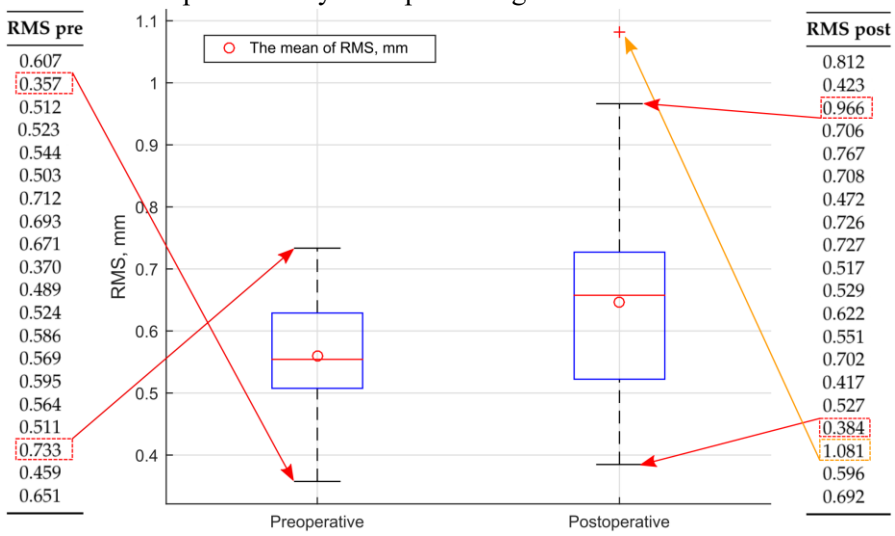

Fig. 5.6. Distributions of RMS values of preoperative and postoperative segmentation data

The interquartile range of the boxplot is narrower for preoperative RMS values. The bigger distribution of RMS values is seen in the postoperative cases. This could have been caused by a better quality of the preoperative CBCT datasets.

Also, for geometrical differences, HD values were calculated for each group: preoperative and postoperative. The mean value of HD was 0.239 (SD ± 0.049) mm in the preoperative cases, and 0.312 (SD ± 0.148) mm in the postoperative cases. The results of the calculated HD values in each group are presented by the boxplot function (Fig. 5.7).

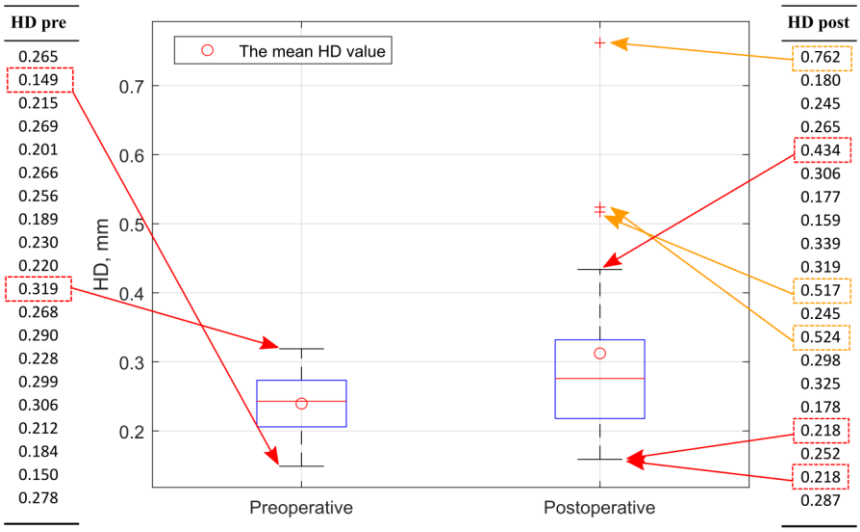

Fig. 5.7. Distribution of HD values of preoperative and postoperative segmentation data

Three values of HD are out of the HD range in the postoperative cases; they are marked as outliers.

The calculated different MSD values are presented in Table 5.2.

Table. 5.2. Calculated positive (+MSD), negative (–MSD), and mean MSD values in each group

Preoperative			*Postoperative*		
+**MSD**, mm	**MSD**, mm	–**MSD**, mm	+**MSD**, mm	**MSD**, mm	– **MSD**, mm
0.102	0.043	– 0.960	0.139	0.057	– 0.065

The achieved results showed very small discrepancies between the surfaces segmented by a surgeon and segmented with the proposed method. The bigger MSD values are calculated in the postoperative cases.

The mean value of DSC was 0.921 (SD ± 0.015) in the preoperative cases. In the postoperative cases, the mean value of DSC was 0.911 (SD ± 0.021). The calculated DSC values are similar and are very high – they are more than 0.9. The results of DSC in the preoperative and postoperative segmentation data are presented by using the boxplot function in Figure 5.8. The narrower range of the interquartile is found in the postoperative cases. Two DSC values are out of the DSC range in the postoperative cases and are marked as outliers.

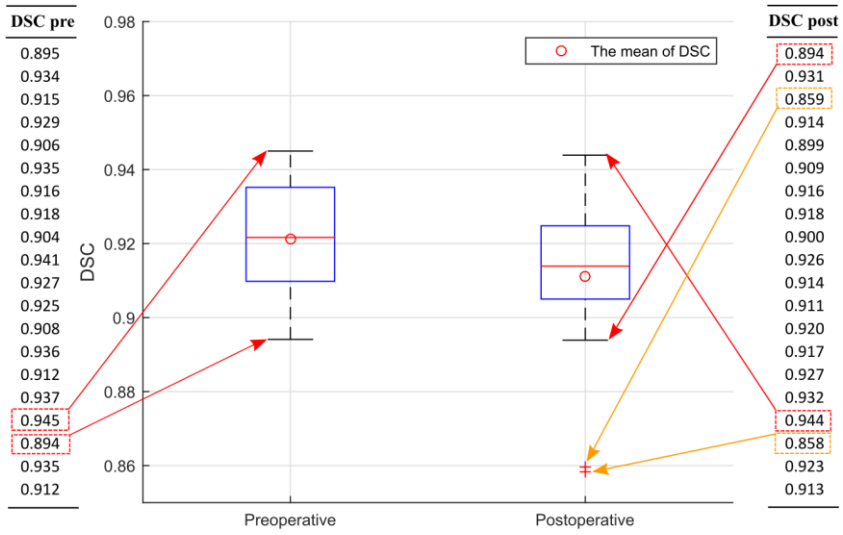

Fig. 5.8. Distribution of DSC values of preoperative and postoperative segmentation data

The applied paired *t-tests* were calculated in order to evaluate the differences between the volumes of the segmented facial bones by a surgeon and the volumes obtained by the proposed automatic segmentation method in each group. The differences of each group were insignificant ($p = 0.76$ in the preoperative cases, $p = 0.82$ in the postoperative cases).

The measured computing time in order to perform automatic segmentation is presented in Figure 5.9.

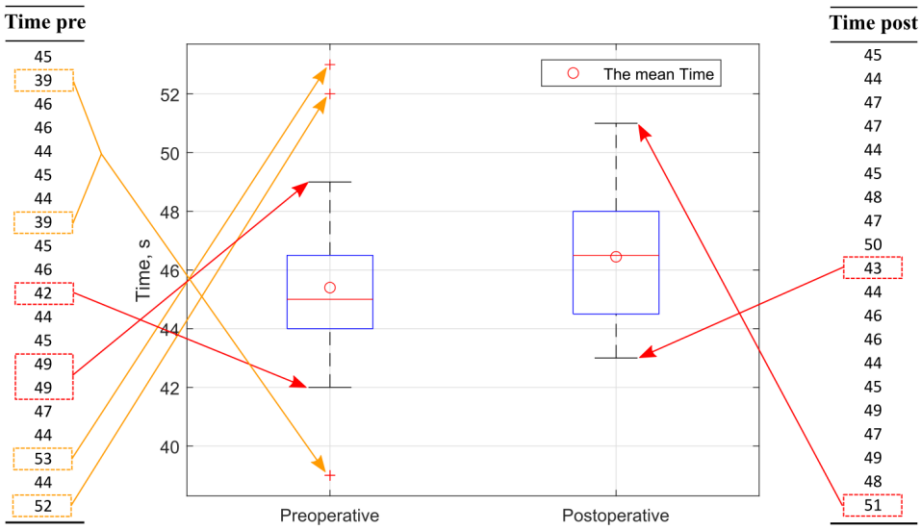

Fig. 5.9. Distribution of computing time values in order to perform automatic segmentation in different cases

The interquartile range of the boxplot is narrower for the preoperative cases. The mean value of the computing time in the preoperative cases is 45 (SD ± 3.43) s, in the postoperative cases, it is 47 (SD ± 2.18) s.

The achieved results of segmentation by the proposed method are presented in Table 5.3.

Table. 5.3. The calculated metrics to evaluate segmentation results by the proposed method

Metric	Proposed
RMS, mm	$(0.559 \pm 0.099)^{a} \mid (0.647 \pm 0.176)^{b}$
HD, mm	$(0.239 \pm 0.049)^{a} \mid (0.312 \pm 0.148)^{b}$
MSD, mm	$(0.043 \pm 0.106)^{1a} \mid (0.102 \pm 0.048)^{2a} \mid (-0.096 \pm 0.064)^{3a}$ $(0.057 \pm 0.134)^{1b} \mid (0.139 \pm 0.013)^{2b} \mid (-0.065 \pm 0.061)^{3b}$
DSC	$(0.921 \pm 0.015)^{a} \mid (0.911 \pm 0.021)^{b}$
Time, s	$(45 \pm 3.43)^{a} \mid (46 \pm 2.18)^{b}$

a – preoperative CBCT, b – postoperative CBCT, 1 – MSD, 2 – positive MSD, 3 – negative MSD

RMS, HD, MSD, DSC, and the speed of segmentation (Time) were the most popular metrics to prove the accuracy of automatic segmentation while using different methods. The achieved values of DSC were similar (the values were close to 0.9) compared to other studies (6, 15, 16). The calculated HD values were lower compared to other studies. Moreover, the calculated HD values in other studies were for mandibles. In the proposed study, HD values were calculated for all the facial bones. MSD was also a common metric serving to evaluate the segmentation results in all the studies. In our study, MSD was calculated and divided into three groups. The results between the MSD values in different groups (preoperative and postoperative) were compared. It was found that the differences were similar. In

comparison to the other studies, when using the proposed method, significantly lower MSD values were found in this study. Finally, the proposed method showed a very short computational time required to perform automatic segmentation for the facial bones.

The results of segmentation by the proposed method showed that low density bones were not completely segmented. However, the areas of condyles and sinuses with fewer holes were segmented by using the proposed method compared to the surgeon's segmentation results (Fig. 5.10 and Fig. 5.11).

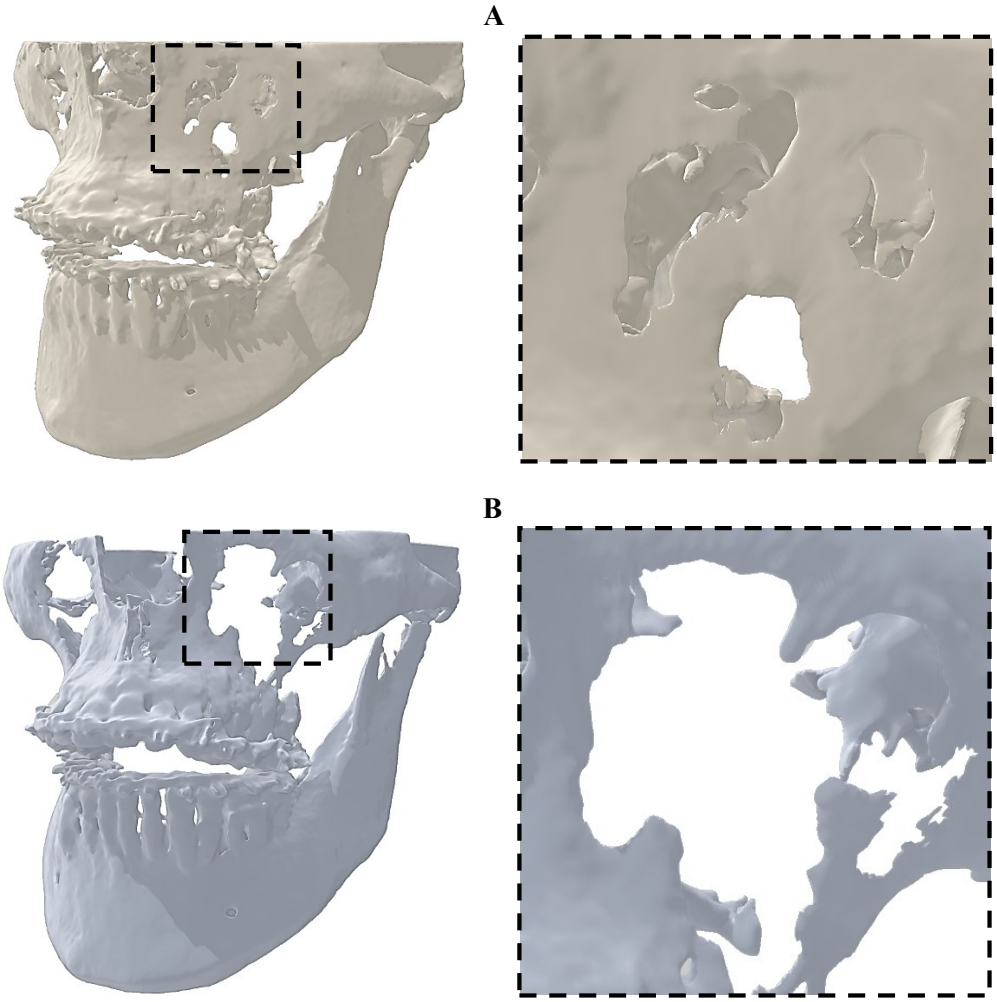

Fig. 5.10. Visual evaluation of two randomly selected 3D models by using different segmentation methods. **A** – segmented with the proposed method, **B** – represents 3D models segmented by using the global threshold method by the surgeon

The presented results showed more accurate segmentation in the area of sinuses by using the proposed method. In clinical practice, this is important for the

surgeon preparing more accurate VSP, or for more accurate fabrication of the patient-specific guide.

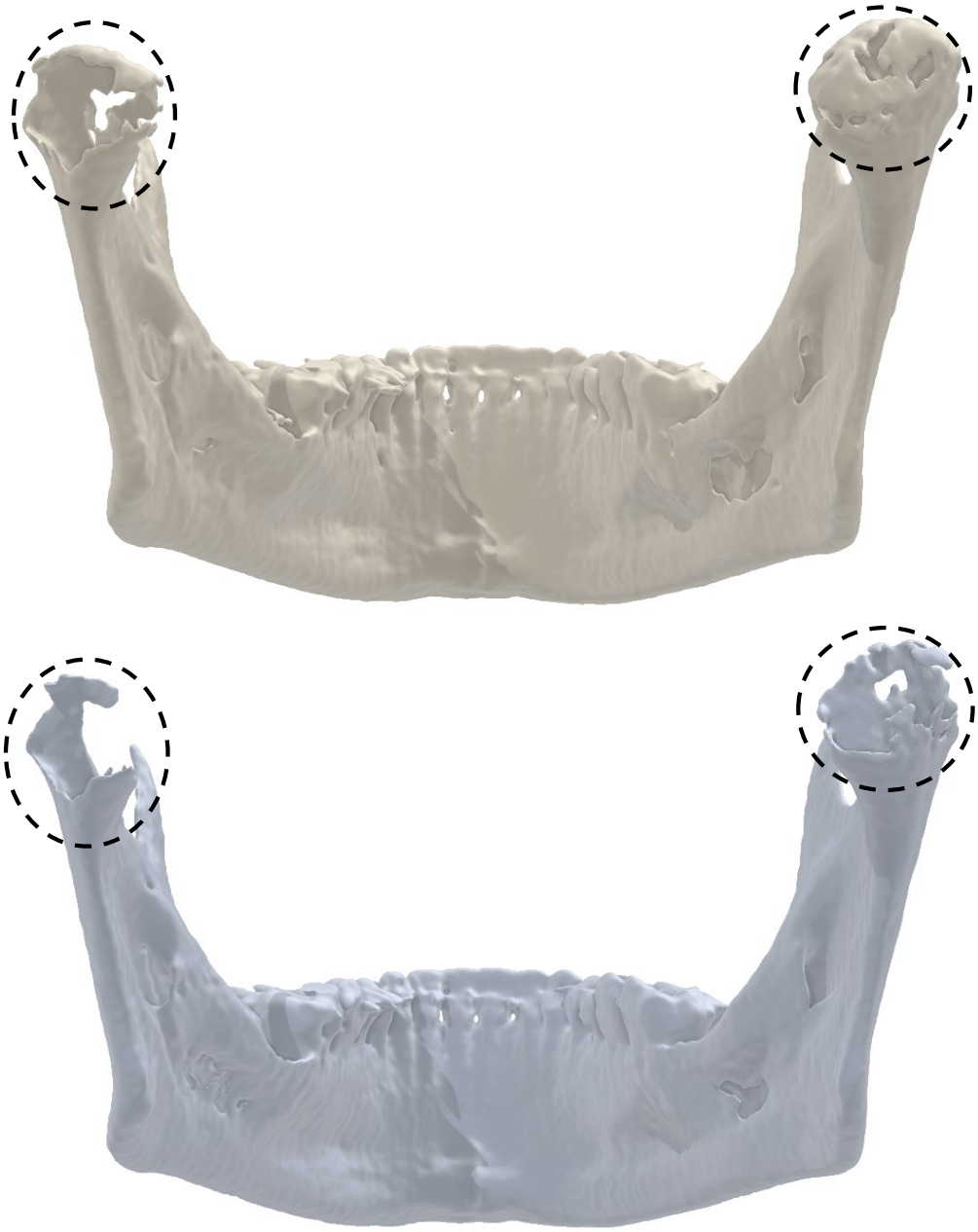

Fig. 5.11. Visual evaluation of 3D models segmented by using the proposed method and the global threshold method by the surgeon

In the mandibular region, the segmentation accuracy of the condyles is higher with the proposed method. The better quality of condyles segmentation can help to

accurately and objectively evaluate the changes after the performed surgery or after orthodontic treatment. Most commonly, condyles segmentation is complicated because the density of the condyles is similar to the soft tissue. Therefore, manual segmentation is used to obtain the complete surface of the condyles.

Discussion. Automatic methods for bone segmentation are very important in medicine. They can help surgeons make correct diagnoses, prepare accurate VSP, and evaluate the postoperative follow-up without the influence of the surgeon's experience (3 – 5, 95, 103). The aim of this research was to develop and investigate the automatic method for facial bones segmentation in CBCT datasets. The method is based on the histogram filter, the 3D sliding window, and Otsu's thresholding. The results of automatic segmentation revealed sufficient clinical/practical accuracy of facial bones segmentation.

In this study, three metrics were used for the evaluation of the reconstructed 3D surface distance – RMS, HD, and MSD, for the evaluation of volumetric overlap evaluation, DSC was used (2, 156, 157). An additional metric based on the time to perform segmentation – the speed of segmentation – was measured. The mean DSC values of the two groups (preoperative and postoperative) were greater than 0.9, which demonstrates the complete volumetric overlap between the automatically segmented volume and the volume segmented by a surgeon. The mean RMS values of the intersurface distance for the preoperative (0.559 mm) and the postoperative (0.647 mm) cases were about two times bigger than the voxel size (0.3 mm). The calculated HD, MSD values showed small discrepancies between the surfaces. This indicates that the segmentation result is accurate. We succeeded to avoid the superimposition step because both automatic and global segmentations were made by using the same source datasets. In this way, surface superimposition did not yield any additional errors. Compared to the other studies (6, 15, 16, 19, 100), the proposed method performed the segmentation very rapidly (46 s/case). The obtained results showed that the proposed automatic method worked accurately.

Further studies may concentrate on evaluating the proposed method with a higher amount and different kind(s) of CT/CBCT datasets. The next direction of further study may be to increase the quality of the segmentation for anatomical regions with a low bone's density. Fully automatic segmentation of the selected anatomical areas, especially those of condyles, would be an important tool to increase the evaluation of the treatment or the postoperative follow-up (45, 158).

5.4 Limitations of the study

The main limitation of this study was that the evaluation of the automatic method based on the segmentation results was performed by only one expert (an orthognathic surgeon) who performs 3D segmentations of facial bones on the daily basis. Accurate evaluation of segmentation can be performed by using software or a hardware phantom (159 – 162) or a cadaver with the soft tissue (100, 153). However, this was not possible in this study due to financial and technical constraints. 3D segmentations will be updated in further studies by other experts with the expectation of reducing inter- and intra-observer variability and ensuring

accurate evaluation of 3D segmentation by the proposed method. It is important to emphasize that the CBCT datasets were obtained with the acquisition parameters used in the routine clinical practice to scan the patient's head before and after the orthognathic surgery. CBCT datasets with higher resolution could not be obtained due to the scanning limitations of the CBCT device. In addition, the CBCT images were not filtered for metal artefacts (brackets, metal plates, and mini-implants) before or after segmentation. For this reason, metal artefacts were seen in the 3D models. These artefacts hide important areas of the bone. Therefore, the assessment of the bone near these artefacts became complicated and inaccurate. This is especially important when postoperative follow-ups are performed (163, 164). Another limitation of the proposed method is the difficulty in segmenting low density anatomical regions (thin anatomical regions, e.g., the alveolar part of the mandible, mandibular condyles, or maxillary sinuses) in CBCT images (165). This is also valid for other threshold-based segmentation methods. Problematic areas could be segmented by including more sensitive techniques (165 – 168).

5.5 Conclusions of the chapter

1. The statistically significant difference between the preoperative and postoperative CBCT datasets was found only by comparing the distribution of HU values in the soft tissue ($p < 0.05$). The voxels distribution of the facial bones is not evident when comparing the preoperative and postoperative CBCT datasets.
2. A fast and efficient automatic method for the segmentation of the facial bones in the CBCT dataset was developed. The volumetric differences between the automatically segmented facial bones and the surgeon segmentation were not statistically significant ($p > 0.05$).
3. The best segmentation results by the calculated metrics were obtained when preoperative CBCT datasets were used. Postoperative CBCT datasets were obtained approximately one week after the surgery. A more swollen soft tissue, as well as additional metal artefacts (metal plates and screws) had a significant impact on the quality of CBCT images. For these reasons, lower segmentation accuracy was obtained in the postoperative cases.
4. The most important feature of the proposed segmentation method is its ease and speed of implementation. The method does not require access to a computer with high computing power. It can be integrated with the most common medical 3D image processing software using an ordinary computer.

6 GENERAL CONCLUSIONS

1. The distribution of voxels HU values was investigated in the histograms of preoperative and postoperative CBCT datasets. The research showed that a significant difference was observed in the soft tissue area when comparing preoperative and postoperative CBCT datasets. It was found that the reason for it was the fact that the soft tissue was swollen after the performed orthognathic surgery. The results of the research showed that the voxels distribution of the facial bones could not be clearly identified. Determining the threshold between the soft tissue and the bone is complicated. For this reason, more accurate and sensitive methods are needed than the global thresholding method which is most commonly used in the clinical practice. Also, in order to reduce the time required to perform accurate evaluation of the patient's condition (during different phases of treatment) and to exclude the user's experience (in performing an accurate virtual surgical plan), an automatic segmentation method is required.

2. An automatic method for facial bones segmentation in the CBCT dataset was developed. Three basic parts were used in the developed method: a Histogram filter, a 3D sliding window, and Otsu's thresholding method. The histogram filter was chosen to maintain the conditions in order to leave two useful anatomical regions from the histogram which were defined between the soft tissue and the facial bones. The 3D sliding window made the segmentation local by the determined volume and the shift of the 3D window.

3. The investigation of the 3D sliding window was performed to evaluate its influence on the segmentation results. The best repeatability of the two 3D model outer surfaces is achieved when the volume of the 3D window is 191 cm^3, and the shift of the 3D window is 29 mm. This selection was based on the aggregate estimation of the segmentation time and the 3D deviation by calculating RMS between the automatically segmented and optically scanned (reference) outer surfaces.

4. The proposed automatic method for the facial bones segmentation was investigated and evaluated against the results of reference segmentations performed by an experienced surgeon. Forty CBCT datasets were used. The calculated performance metrics (RMS, HD, DSC, MSD, and the segmentation time) showed high clinical accuracy of segmentation. The proposed automatic method could be applied in the clinical practice (especially in orthognathic surgery). The implementation of the proposed method is simple and fast; it does not require access to a computer with high computing power.

LIST OF PUBLICATIONS

Publications indexed in the Web of Science with impact factor

1. Rutkūnas, V; Gečiauskaitė, A; Jegelevičius, D; Vaitiekūnas, M. (2017). Accuracy of digital implant impressions with intraoral scanners. A systematic review. *European Journal of Oral Implantology*. Volume: 10 Pages: 101-120 Supplement: 1. [IF: 2.809]
2. Vaitiekūnas, M; Jegelevičius, D; Sakalauskas, A; Grybauskas, S. (2020). Automatic Method for Bone Segmentation in Cone Beam Computed Tomography Data Set. *Applied Sciences-Basel*. Volume: 10 Issue: 1. [IF: 2.217]

Publications in proceedings of the international scientific conferences

1. Vaitiekūnas, M; Jegelevičius, D; Sakalauskas, A; Grybauskas, S. Method for Automatic 3D Bone Segmentation in CBCT Data. *Abstract book at EMBEC'17 & NBC'17: the joint conference of the European medical and biological engineering conference (EMBEC) and the Nordic-Baltic conference on biomedical engineering and medical physics (NBC)*, June 11-15, 2017, Tampere, Finland / organized by BioMediTech, Finnish Society for Medical Physics and Medical Engineering. [S.l.]: [s.n.]. 2017, 471, p. 184.
2. Vaitiekūnas, M. Evaluation of short and long-term surgical outcomes and morphological changes by means of superimposition. Oral presentation. *BSCOSO (Baltic Sea Community on Orthognathic Surgery and Orthodontics) Winter Course*. Lithuania, Vilnius. 2018.
3. Vaitiekūnas, M. Automatinė veidinės dalies kaulų segmentacija kompiuterinės tomografijos vaizduose. *Fizinių ir technologijos mokslų tarpdalykiniai tyrimai: 10-oji jaunųjų mokslininkų konferencija: pranešimų santraukos*. Vilnius: [Lietuvos mokslų akademija]. 2020. p. 27.

REFERENCES

1. WALLNER, Jürgen, et al. Computed tomography data collection of the complete human mandible and valid clinical ground truth models. *Scientific data*. 2019, (6): 190003.
2. TAHA, A. A. and A. HANBURY. Metrics for evaluating 3D medical image segmentation: analysis, selection, and tool. *BMC medical imaging*. 2015, 15(29).
3. LEBRE, Marie-Ange, et al. Automatic segmentation methods for liver and hepatic vessels from CT and MRI volumes, applied to the Couinaud scheme. *Computers in biology and medicine*. 2019, 110, 42-51.
4. SAKINIS, Tomas, et al. Interactive segmentation of medical images through fully convolutional neural networks. *arXiv preprint arXiv:1903.08205*, 2019.
5. FRIPP, Jurgen, et al. Automatic segmentation of the bone and extraction of the bone–cartilage interface from magnetic resonance images of the knee. *Physics in Medicine & Biology*. 2007, 52(6), 1617-1631.
6. WANG, Li, et al. Automated segmentation of CBCT image using spiral CT atlases and convex optimization. In: *International Conference on Medical Image Computing and Computer-Assisted Intervention*. Springer, Berlin, Heidelberg, 2013. pp. 251-258.
7. DESPOTOVIĆ, Ivana, et al. MRI segmentation of the human brain: challenges, methods, and applications. *Computational and mathematical methods in medicine.* 2015, 2015.
8. HWANG, Shik, et al. Maxillofacial 3-dimensional image analysis for the diagnosis of facial asymmetry. *American journal of orthodontics and dentofacial orthopaedics*. 2006, 130(6) 779-785.
9. STOKBRO, K., et al. Virtual planning in orthognathic surgery. *International journal of oral and maxillofacial surgery*. 2014, 43(8), 957-965.
10. FAN, Yi, et al. 3D assessment of mandibular skeletal effects produced by the Herbst appliance. *BMC Oral Health*. 2020, 20, 1-9.
11. SHAHEEN, E., et al. Three-dimensional planning accuracy and follow-up protocol in orthognathic surgery: a validation study. *International journal of oral and maxillofacial surgery*. 2019, 48(1), 71-76.
12. PAUWELS, Ruben, et al. CBCT-based bone quality assessment: are Hounsfield units applicable? *Dentomaxillofacial Radiology*. 2015, 44(1).
13. PAUWELS, Ruben, et al. Variability of dental cone beam CT grey values for density estimations. *The British journal of radiology*. 2013, 86(1021).
14. KATSUMATA, Akitoshi, et al. Image artifact in dental cone-beam CT. *Oral Surgery, Oral Medicine, Oral Pathology, Oral Radiology, and Endodontology*. 2006, 101(5), 652-657.
15. WANG, Li, et al. Automated bone segmentation from dental CBCT images using patch-based sparse representation and convex optimization. *Medical physics*. 2014, 41(4), 1-14.

16. WANG, Li, et al. Automated segmentation of dental CBCT image with prior-guided sequential random forests. *Medical physics*. 2016, 43(1), 336-346.
17. MINNEMA, Jordi, et al. CT image segmentation of bone for medical additive manufacturing using a convolutional neural network. *Computers in biology and medicine*. 2018, 103, 130-139.
18. GOLLMER, S., T., and T., M., BUZUG. Fully automatic shape constrained mandible segmentation from cone-beam CT data. In: *2012 9th IEEE International Symposium on Biomedical Imaging (ISBI),* May *2-5, 2012, Barcelona*, Spain. IEEE, 2012. pp. 1272-1275.
19. FAN, Yi, et al. Marker-based watershed transform method for fully automatic mandibular segmentation from CBCT images. *Dentomaxillofacial Radiology*. 2019, 48(2).
20. VAN EIJNATTEN, Maureen, et al. CT image segmentation methods for bone used in medical additive manufacturing. *Medical engineering & physics*. 2018, 51, 6-16.
21. JINKINS, J. Randy (ed.). *Atlas of neuroradiologic embryology, anatomy, and variants*. Lippincott Williams & Wilkins, 2000.
22. MARDIA, Kanti, et al. Statistical assessment of bilateral symmetry of shapes. *Biometrika*. 2000, 87(2), 285-300.
23. CHEONG, Y., W., and L. LUN-JOU. Facial asymmetry: etiology, evaluation, and management. *Chang Gung Medical Journal*. 2011, 34(4), 341-351.
24. LUNDSTRÖM, Anders. Some asymmetries of the dental arches, jaws, and skull, and their etiological significance. *American Journal of Orthodontics*. 1961, 47(2), 81-106.
25. BISHARA, S., E., et al. Dental and facial asymmetries: a review. *The Angle Orthodontist*. 1994, 64(2), 89-98.
26. ANISON, Job Jacob et al. Understanding Asymmetry–A Review. *Biomedical and Pharmacology Journal*. 2015, 8(October Spl Edition), 659-668.
27. SRIVASTAVA, Dhirendra, et al. Facial asymmetry revisited: Part I-diagnosis and treatment planning. *Journal of oral biology and craniofacial research*. 2018, 8(1), 7-14.
28. WANG, Tim T., et al. Discriminative thresholds in facial asymmetry: a review of the literature. *Aesthetic surgery journal*. 2017, 37(4), 375-385.
29. SHACKELFORD, T., K., and R., J., LARSEN. Facial asymmetry as an indicator of psychological, emotional, and physiological distress. *Journal of personality and social psychology*. 1997, 72(2), 456-466.
30. THORNHILL, R., and A., P., MØLLER. Developmental stability, disease and medicine. *Biological Reviews*. 1997, 72(4), 497-548.
31. BUSS, David M. Sex differences in human mate selection criteria: An evolutionary perspective. *Sociobiology and psychology: Ideas, issues, and applications*. 1987, 335-352.

32. RHODES, Gillian, et al. Facial symmetry and the perception of beauty. *Psychonomic Bulletin & Review*. 1998, 5(4), 659-669.
33. SAMMAN, Nabil, et al. Analysis of 300 dentofacial deformities in Hong Kong. *The International journal of adult orthodontics and orthognathic surgery*. 1992, 7(3), 181-185.
34. SEVERT, T., R., and W., R., PROFFIT. The prevalence of facial asymmetry in the dentofacial deformities population at the University of North Carolina. *The International journal of adult orthodontics and orthognathic surgery*. 1997, 12(3), 171-176.
35. HARAGUCHI, Seiji, et al. Facial asymmetry in subjects with skeletal Class III deformity. *The Angle Orthodontist*. 2002, 72(1), 28-35.
36. KATSUMATA, Akitoshi, et al. 3D-CT evaluation of facial asymmetry. *Oral Surgery, Oral Medicine, Oral Pathology, Oral Radiology, and Endodontology*. 2005, 99(2), 212-220.
37. CHEW, Ming Tak. Spectrum and management of dentofacial deformities in a multiethnic Asian population. *The Angle Orthodontist*. 2006, 76(5), 806-809.
38. LITJENS, Geert, et al. A survey on deep learning in medical image analysis. *Medical Image Analysis*. 2017, 42, 60-88.
39. PHAM, D., L., et al. Current methods in medical image segmentation. *Annual review of biomedical engineering*, 2000, 2(1), 315-337.
40. HO, Cheng-Ting, et al. Three-dimensional surgical simulation improves the planning for correction of facial prognathism and asymmetry: A qualitative and quantitative study. *Scientific reports*. 2017, 7(1), 1-10.
41. SANTANDER, Petra, et al. Comprehensive 3D analysis of condylar morphology in adults with different skeletal patterns – a cross-sectional study. *Head & Face Medicine*. 2020, 16(1), 1-10.
42. LIN, Hsiu-Hsia, et al. 3D printing in orthognathic surgery − A literature review. *Journal of the Formosan Medical Association*. 2018, 117(7), 547-558.
43. LOUBELE, Miet, et al. Assessment of bone segmentation quality of CT scanners using laser scanning. *International Journal of Computer Assisted Radiology and Surgery*. 2006, 1(7), 400-402.
44. POLETI, M., L., et al. Analysis of linear measurements on 3D surface models using CBCT data segmentation obtained by automatic standard pre-set thresholds in two segmentation software programs: an in vitro study. *Clinical oral investigations*. 2016, 20(1), 179-185.
45. ENGELBRECHT, W., P., et al. The influence of the segmentation process on 3D measurements from cone beam computed tomography-derived surface models. *Clinical oral investigations*. 2013, 17(8), 1919-1927.
46. AKHIL, Gopi, et al. Three-dimensional assessment of facial asymmetry: A systematic review. *Journal of pharmacy & bioallied sciences*. 2015, 7.Suppl 2: S433.

47. BENGTSSON, Martin, et al. Treatment outcome in orthognathic surgery – A prospective comparison of accuracy in computer assisted two and three-dimensional prediction techniques. *Journal of Cranio-Maxillofacial Surgery*. 2018, 46(11), 1867-1874.
48. LO, Lun-Jou, et al. Computer-assisted orthognathic surgery for patients with cleft lip/palate: from traditional planning to three-dimensional virtual surgery simulation. *The Cleft Palate-craniofacial Journal*. 2016, 53(4), e0152014.
49. CUI, Z., et al. Automatic tooth instance segmentation and identification from cone beam CT images. In *Proceedings of the IEEE Conference on Computer Vision and Pattern Recognition*. 2019. pp. 6368-6377.
50. LEE, R., J., et al. Monitoring of typodont root movement via crown superimposition of single cone-beam computed tomography and consecutive intraoral scans. *American Journal of Orthodontics and Dentofacial Orthopedics*. 2014, 145(3), 399-409.
51. JUNG, W., et al. Combining volumetric dental CT and optical scan data for teeth modeling. *Computer-Aided Design*. 2015, 67, 24-37.
52. MORCOS, S., S., and P., K., PATEL. The vocabulary of dentofacial deformities. *Clinics in plastic surgery*. 2007, 34(3), 589-599.
53. BAI, Shizhu, et al. Computer-aided design and computer-aided manufacturing locating guides accompanied with prebent titanium plates in orthognathic surgery. *Journal of oral and maxillofacial surgery*. 2012, 70(10), 2419-2426.
54. ISSA S., A. and H., A. ABDULNABI. Outcomes of using pre-bent reconstruction plates in mandibular reconstruction. *European Journal of oral and Maxillofacial Surgery*. 2020, 4(1), 1-7.
55. HU, YiHui, et al. Simultaneous treatment of temporomandibular joint ankylosis with severe mandibular deficiency by standard TMJ prosthesis. *Scientific Reports*. 2017, 7, 45271.
56. KIM, Jung-Hoon, et al. Accuracy of 3-dimensional virtual surgical simulation combined with digital teeth alignment: a pilot study. *Journal of Oral and Maxillofacial Surgery*. 2017, 75(11), 2441.e1-2441.e13.
57. HWANG, Hyeon-Shik, et al. Maxillofacial 3-dimensional image analysis for the diagnosis of facial asymmetry. *American journal of orthodontics and dentofacial orthopedics*. 2006, 130(6), 779-785.
58. JI, H., et al. Computer-assisted osteotomy guides and pre-bent titanium plates improve the planning for correction of facial asymmetry. *International journal of oral and maxillofacial surgery*. 2019, 48(8), 1043-1050.
59. SWENNEN, Gwen RJ, et al. Three-dimensional treatment planning of orthognathic surgery in the era of virtual imaging. *Journal of oral and maxillofacial surgery*. 2009, 67(10), 2080-2092.
60. CEVIDANES, Lucia HC, et al. Clinical application of 3D imaging for assessment of treatment outcomes. *Seminars in orthodontics*. 2011, 17(1), 72-80.

61. CHEN, Hui, et al. Accuracy of MDCT and CBCT in three-dimensional evaluation of the oropharynx morphology. *European Journal of Orthodontics*. 2018, 40(1), 58-64.
62. HAMMOUDEH, J., A., et al. Current status of surgical planning for orthognathic surgery: traditional methods versus 3D surgical planning. *Plastic and reconstructive surgery Global open*. 2015, 3(2), e307.
63. Materialise Mimics. Available online: https://www.materialise.com/en/medical/mimics-innovation-suite/mimics (accessed on 5 May 2017).
64. Dolphin imaging. Available online: https://www.dolphinimaging.com/ (accessed on 15 December 2015).
65. NemoFab. Available online: https://www.nemotec.com/en/software/nemofab (accessed on 4 July 2017).
66. MARDINI, Samir, et al. Three-dimensional preoperative virtual planning and template use for surgical correction of craniosynostosis. *Journal of Plastic, Reconstructive & Aesthetic Surgery*. 2014, 67(3), 336-343.
67. GARCÍA-MATO, D., et al. Craniosynostosis surgery: workflow based on virtual surgical planning, intraoperative navigation and 3D printed patient-specific guides and templates. *Scientific reports*. 2019, 9(1), 1-10.
68. CAITI, Giuliana, et al. Positioning error of custom 3D-printed surgical guides for the radius: influence of fitting location and guide design. *International journal of computer assisted radiology and surgery*. 2018, 13(4), 507-518.
69. LI, Biao, et al. A new approach of splint-less orthognathic surgery using a personalized orthognathic surgical guide system: a preliminary study. *International journal of oral and maxillofacial surgery*. 2017, 46(10), 1298-1305.
70. GIOVANNI, Badiali, et al. Validation of a patient-specific system for mandible-first bimaxillary surgery: ramus and implant positioning precision assessment and guide design comparison. *Scientific Reports*. 2020, 10(1).
71. STEINBACHER, D., M. Three-dimensional analysis and surgical planning in craniomaxillofacial surgery. *Journal of Oral and Maxillofacial Surgery*. 2015, 73(12), S40-S56.
72. YANG, Wei-fa, et al. Three-dimensional printing of patient-specific surgical plates in head and neck reconstruction: a prospective pilot study. *Oral oncology*. 2018, 78, 31-36.
73. KRAEIMA, J., et al. Splintless surgery: does patient-specific CAD-CAM osteosynthesis improve accuracy of Le Fort I osteotomy?. *British Journal of Oral and Maxillofacial Surgery*. 2016, 54(10), 1085-1089.
74. CEVIDANES, Lucia HS, et al. Superimposition of 3D cone-beam CT models of orthognathic surgery patients. *Dentomaxillofacial Radiology*. 2005, 34(6), 369-375.

75. WEISSHEIMER, André, et al. Fast three-dimensional superimposition of cone beam computed tomography for orthopaedics and orthognathic surgery evaluation. *International journal of oral and maxillofacial surgery*. 2015, 44(9), 1188-1196.
76. SHAHEN, Shereef, et al. United Reference Method for three-dimensional treatment evaluation. *Progress in orthodontics*. 2018, 19(1), 1-8.
77. GKANTIDIS, Nikolaos, et al. Evaluation of 3-dimensional superimposition techniques on various skeletal structures of the head using surface models. *PLoS One*. 2015, 10(2), e0118810.
78. PERIAGO, Danielle R., et al. Linear accuracy and reliability of cone beam CT derived 3-dimensional images constructed using an orthodontic volumetric rendering program. *The Angle Orthodontist*. 2008, 78(3), 387-395.
79. SUOMALAINEN, Anni, et al. Accuracy of linear measurements using dental cone beam and conventional multislice computed tomography. *Dentomaxillofacial Radiology*. 2008, 37(1), 10-17.
80. LIANG, Xin, et al. A comparative evaluation of cone beam computed tomography (CBCT) and multi-slice CT (MSCT). Part II: On 3D model accuracy. *European journal of radiology*. 2010, 75(2), 270-274.
81. KOERICH, Leonardo, et al. Rapid 3D mandibular superimposition for growing patients. *The Angle Orthodontist*. 2017, 87(3), 473-479.
82. ALMUKHTAR, Anas, et al. Comparison of the accuracy of voxel based registration and surface based registration for 3D assessment of surgical change following orthognathic surgery. *PloS One*. 2014, 9(4), e93402.
83. HÄNER, Simeon T., et al. Voxel-based superimposition of serial craniofacial CBCTs: Reliability, reproducibility and segmentation effect on hard-tissue outcomes. *Orthodontics & craniofacial research*. 2020, 23(1), 92-101.
84. GARIB, Daniela, et al. Superimposition of maxillary digital models using the palatal rugae: Does ageing affect the reliability? *Orthodontics & craniofacial research*. 2019, 22(3), 183-193.
85. PARK, Tae-Joon, et al. A method for mandibular dental arch superimposition using 3D cone beam CT and orthodontic 3D digital model. *The Korean Journal of Orthodontics*, 2012, 42(4), 169-181.
86. PONCE-GARCIA, Cecilia, et al. Measurement error and reliability of three available 3D superimposition methods in growing patients. *Head & Face Medicine*, 2020, 16(1), 1.
87. CEVIDANES, Lucia HC, et al. Superimposition of 3-dimensional cone-beam computed tomography models of growing patients. *American Journal of Orthodontics and Dentofacial Orthopedics*. 2009, 136(1), 94-99.
88. NGUYEN, Tung, et al. Three-dimensional mandibular regional superimposition in growing patients. *American Journal of Orthodontics and Dentofacial Orthopedics*. 2018, 153(5), 747-754.

89. RUELLAS, Antonio Carlos de Oliveira, et al. 3D mandibular superimposition: comparison of regions of reference for voxel-based registration. *PLoS One*. 2016, 11(6), e0157625.
90. LIEBREGTS, Jeroen, et al. One-year postoperative skeletal stability of 3D planned bimaxillary osteotomies: maxilla-first versus mandible-first surgery. *Scientific reports*. 2019, 9(1), 1-9.
91. TONIN, Renata Hernandes, et al. Accuracy of 3D virtual surgical planning for maxillary positioning and orientation in orthognathic surgery. *Orthodontics & Craniofacial Research.* 2020, 23(2), 229-236.
92. WEISSHEIMER, A., et al. Fast three-dimensional superimposition of cone beam computed tomography for orthopaedics and orthognathic surgery evaluation. *International journal of oral and maxillofacial surgery*. 2015, 44(9), 1188-1196.
93. CHANG, Yu-Jen, et al. Accuracy assessment of computer-aided three-dimensional simulation and navigation in orthognathic surgery (CASNOS). *Journal of the Formosan Medical Association*. 2020, 119(3), 701-711.
94. JAYARATNE, Yasas SN, et al. Three-dimensional color maps: a novel tool for assessing craniofacial changes. *Surgical innovation*. 2010, 17(3), 198-205.
95. WALLNER, Jürgen, et al. Clinical evaluation of semi-automatic open-source algorithmic software segmentation of the mandibular bone: Practical feasibility and assessment of a new course of action. *PLoS One*. 2018, 13(5), e0196378.
96. KRČAH, Marcel, et al. Fully automatic and fast segmentation of the femur bone from 3D-CT images with no shape prior. In *2011 IEEE international symposium on biomedical imaging: from nano to macro*. *March 30 – April 2*, 2012, Chicago, IL, USA. IEEE, 2011. pp. 2087-2090.
97. LINARES, Oscar Cuadros, et al. Mandible and skull segmentation in cone beam computed tomography using super-voxels and graph clustering. *The Visual Computer*. 2019, 35(10), 1461-1474.
98. WANG, L., I., et al. Validation of bone segmentation and improved 3-D registration using contour coherency in CT data. *IEEE transactions on medical imaging*. 2006, 25(3), 324-334.
99. CHANG, Yu-Bing, et al. 3D segmentation of maxilla in cone-beam computed tomography imaging using base invariant wavelet active shape model on customized two-manifold topology. *Journal of X-ray science and technology*. 2013, 21(2), 251-282.
100. VAN EIJNATTEN, Maureen, et al. The impact of manual threshold selection in medical additive manufacturing. *International Journal of Computer Assisted Radiology and Surgery*. 2017, 12(4), 607-615.
101. OTSU, Nobuyuki. A threshold selection method from gray-level histograms. *IEEE transactions on systems, man, and cybernetics*. 1979, 9(1), 62-66.

102. BARANDIARAN, Iñigo, et al. An automatic segmentation and reconstruction of mandibular structures from CT-data. In: *International Conference on Intelligent Data Engineering and Automated Learning*. Springer, Berlin, Heidelberg, 2009. p. 649-655.
103. INDRASWARI, Rarasmaya, et al. Automatic segmentation of mandibular cortical bone on cone-beam CT images based on histogram thresholding and polynomial fitting. *International Journal of Intelligent Engineering and Systems*. 2019, 12(4), 130-141.
104. ARIFIN, A., Z., and A. ASANO. Image segmentation by histogram thresholding using hierarchical cluster analysis. *Pattern recognition letters*. 2006, 27(13), 1515-1521.
105. HOJJATOLESLAMI, S., A. and J., KITTLER. Region growing: a new approach. *IEEE Transactions on Image processing*. 1998, 7(7), 1079-1084.
106. XI, Tong, et al. A novel region-growing based semi-automatic segmentation protocol for three-dimensional condylar reconstruction using cone beam computed tomography (CBCT). *PloS One*. 2014, 9(11), e111126.
107. CHEN, Xiaojun, et al. A semi-automatic computer-aided method for surgical template design. *Scientific reports*. 2016, 6(1), 1-18.
108. DUTAILLY, Bruno, et al. 3D surface reconstruction using HMH algorithm. In: *2009 16th IEEE International Conference on Image Processing (ICIP)*. IEEE, 2009. p. 2505-2508.
109. LORENSEN, W., E. and H., E., CLINE. Marching cubes: A high resolution 3D surface construction algorithm. *ACM siggraph computer graphics*. 1987, 21(4), 163-169.
110. JIN, Jing, et al. An improved marching cubes method for surface reconstruction of volume data. In: *2006 6th World Congress on Intelligent Control and Automation*. IEEE, 2006. p. 10454-10457.
111. CIRNE, M., V., M. and H., PEDRINI. Marching cubes technique for volumetric visualization accelerated with graphics processing units. *Journal of the Brazilian Computer Society*. 2013, 19(3), 223-233.
112. CUSTODIO, Lis, et al. An extended triangulation to the Marching Cubes 33 algorithm. *Journal of the Brazilian Computer Society*. 2019, 25(1), 1-18.
113. Curless, B. and M., A., Levoy. A volumetric method for building complex models from range images. In: *Proceedings of the 23rd Annual Conference on Computer Graphics and Interactive Techniques—SIGGRAPH '96, New York, NY, USA*. 11–15 June 1996; pp. 303–312
114. Meshlab. Available online: www.meshlab.net (accessed on 5 May 2015).
115. HANS, Mark G., et al. History of imaging in orthodontics from Broadbent to cone-beam computed tomography. *American Journal of Orthodontics and Dentofacial Orthopedics*. 2015, 148(6), 914-921.
116. ABRAMOVITCH, K., and D., D., RICE. Basic principles of cone beam computed tomography. *Dental Clinics*. 2014, 58(3) 463-484.

117. DE VOS, W., et al. Cone-beam computerized tomography (CBCT) imaging of the oral and maxillofacial region: a systematic review of the literature. *International journal of oral and maxillofacial surgery*. 2009, 38(6), 609-625.
118. SCARFE, William C., et al. Clinical applications of cone-beam computed tomography in dental practice. *Journal-Canadian Dental Association*. 2006, 72(1), 75.
119. ZHANG, G., et al. Bowtie filtration for dedicated cone beam CT of the head and neck: a simulation study. *The British journal of radiology*. 2013, 86(1028).
120. Hendee, William R. Cone Beam Computed Tomography. Taylor & Francis Group, 2014.
121. MIRACLE, A., C., and S., K., MUKHERJI. Conebeam CT of the head and neck, part 1: physical principles. *American Journal of Neuroradiology*. 2009, 30(6), 1088-1095.
122. i-CAT™ FLX V-SERIES. Available online: https://www.kavo.com/en-us/imaging-solutions/i-cat-flx-v-series-cone-beam-3d-imaging (accessed on 19 September 2019).
123. WATANABE, H., et al. Modulation transfer function evaluation of cone beam computed tomography for dental use with the oversampling method. *Dentomaxillofacial Radiology*. 2010, 39(1), 28-32.
124. PINEDA, Angel R., et al. Analysis of image noise in 3D cone-beam CT: spatial and Fourier domain approaches under conditions of varying stationarity. *Medical Imaging 2008: Physics of Medical Imaging*. 2008, 6913, 69131Q.
125. MARTIN, C., J., et al. Balancing patient dose and image quality. *Applied radiation and isotopes*. 1999, 50(1), 1-19.
126. FARMAN, Allan G. ALARA still applies. *Oral Surgery, Oral Medicine, Oral Pathology, Oral Radiology and Endodontology*. 2005, 4(100), 395-397.
127. LUDLOW, J. B., et al. Effective dose of dental CBCT—a meta analysis of published data and additional data for nine CBCT units. *Dentomaxillofacial Radiology*. 2015, 44(1) 20140197.
128. NARDI, Cosimo, et al. Head and neck effective dose and quantitative assessment of image quality: a study to compare cone beam CT and multislice spiral CT. *Dentomaxillofacial Radiology*. 2017, 46(7), 20170030.
129. MEN, K., and J., DAI. A Projection Quality-Driven Tube Current Modulation Method in Cone-Beam CT for IGRT: Proof of Concept. *Technology in cancer research & treatment*. 2017, 16(6), 1179-1186.
130. PAUWELS, Ruben, et al. A pragmatic approach to determine the optimal kVp in cone beam CT: balancing contrast-to-noise ratio and radiation dose. *Dentomaxillofacial Radiology*. 2014, 43(5), 20140059.

131. ALAWAJI, Yasmine, et al. Optimization of cone beam computed tomography image quality in implant dentistry. *Clinical and Experimental Dental Research*. 2018, 4(6), 268-278.
132. FELDKAMP, Lee A., et al. Practical cone-beam algorithm. *Josa a*, 1984, 1(6), 612-619.
133. MIAO, Hui, et al. Implementation of FDK reconstruction algorithm in cone-beam CT based on the 3D Shepp-Logan model. In: *2009 2nd International Conference on Biomedical Engineering and Informatics*. IEEE, 2009. p. 1-5.
134. MOLTENI, Roberto. Prospects and challenges of rendering tissue density in Hounsfield units for cone beam computed tomography. *Oral surgery, oral medicine, oral pathology and oral radiology*. 2013, 116(1), 105-119.
135. MISCH, Carl E. Contemporary implant dentistry. *Implant Dentistry*. 1999, 8(1), 90.
136. NORTON, M., R., and C., GAMBLE. Bone classification: an objective scale of bone density using the computerized tomography scan. *Clinical oral implants research*. 2001, 12(1), 79-84.
137. NAITOH, Munetaka, et al. Measurement of mandibles with microfocus x-ray computerized tomography and compact computerized tomography for dental use. *International Journal of Oral & Maxillofacial Implants*. 2004, 19(2), 239-246.
138. NAITOH, Munetaka, et al. Evaluation of voxel values in mandibular cancellous bone: relationship between cone-beam computed tomography and multislice helical computed tomography. *Clinical oral implants research*. 2009, 20(5), 503-506.
139. ARANYARACHKUL, Prasit, et al. Bone density assessments of dental implant sites: 2. Quantitative cone-beam computerized tomography. *International Journal of Oral & Maxillofacial Implants.* 2005, 20(3), 416-424.
140. LIANG, Xin, et al. A comparative evaluation of cone beam computed tomography (CBCT) and multi-slice CT (MSCT). Part II: On 3D model accuracy. *European journal of radiology*. 2010, 75(2), 270-274.
141. SILVA, Isabela Maria de Carvalho Crusoé, et al. Bone density: comparative evaluation of Hounsfield units in multislice and cone-beam computed tomography. *Brazilian oral research*. 2012, 26(6), 550-556.
142. CBCT device: i-CAT™ FLX V17. Access through link: https://www.kavo.com/en-us/imaging-solutions/i-cat-flx-v-series-cone-beam-3d-imaging.
143. PAUWELS, Ruben, et al. Technical aspects of dental CBCT: state of the art. Dentomaxillofacial Radiology, 2015, 44.1: 20140224.
144. PARINYACHAIPHUN, Sikkared, et al. Considerations for placement of mandibular buccal shelf orthodontic anchoring screw in Class III hyperdivergent and normodivergent subjects–A cone beam computed tomography study. *Orthodontic Waves*. 2018, 77(1), 44-56.

145. Mitutyo, CRYSTA-APEX S SE. Access through link: https://www.mitutoyo.com/wp-content/uploads/2013/01/2097_CRYSTA_ApexS.pdf (p. 1).
146. RYNIEWICZ, Wojciechand, et al. Geometrical parameters of the mandible in 3D CBCT imaging. Biocybernetics and Biomedical Engineering. 2019, 39(2), 301-311.
147. Creaform. Portable 3D optical scanner: HandySCAN 700. Access through link: https://www.creaform3d.com/sites/default/files/assets/brochures/files/handyscan3d_brochure_en_hq_21032017_2.pdf.
148. LOW, Kok-Lim. Linear least-squares optimization for point-to-plane icp surface registration. *Chapel Hill, University of North Carolina*. 2004, 4(10), 1-3.
149. Geomagic Control X, 3D Systems, USA, Version 2018.1.1.
150. VAITIEKŪNAS, Mantas, et al. Automatic Method for Bone Segmentation in Cone Beam Computed Tomography Data Set. *Applied Sciences.* 2020, 10(1), 236.
151. Meshlab Software. Available online: www.meshlab.net (accessed on 5 May 2019).
152. CURLESS, B., and M., LEVOY. A volumetric method for building complex models from range images. In: Proceedings of the 23rd annual conference on Computer graphics and interactive techniques. 1996. p. 303-312.
153. FOURIE, Zacharias, et al. Segmentation process significantly influences the accuracy of 3D surface models derived from cone beam computed tomography. *European journal of radiology*. 2012, 81(4), 524-530.
154. http://www.itksnap.org/
155. KOO, T., K. and M., Y., LI. A guideline of selecting and reporting intraclass correlation coefficients for reliability research. *Journal of chiropractic medicine*. 2016, 15(2), 155-163.
156. DICE, Lee R. Measures of the amount of ecologic association between species. *Ecology*. 1945, 26(3), 297-302.
157. HOSSEINI, Mohammad-Parsa, et al. Comparative performance evaluation of automated segmentation methods of hippocampus from magnetic resonance images of temporal lobe epilepsy patients. *Medical physics*. 2016, 43(1), 538-553.
158. NICOLIELO, Laura Ferreira Pinheiro, et al. Validation of a novel imaging approach using multi-slice CT and cone-beam CT to follow-up on condylar remodeling after bimaxillary surgery. International Journal of Oral Science. 2017, 9(3), 139-144.
159. KALENDER, Willi A., et al. The European Spine Phantom—a tool for standardization and quality control in spinal bone mineral measurements by DXA and QCT. *European journal of radiology*. 1995, 20(2), 83-92.

160. PREVRHAL, Sven, et al. Accuracy limits for the determination of cortical width and density: the influence of object size and CT imaging parameters. *Physics in Medicine & Biology*. 1999, 44(3), 751.
161. KANG, Yanet, et al. A new accurate and precise 3-D segmentation method for skeletal structures in volumetric CT data. *IEEE transactions on medical imaging*. 2003, 22(5), 586-598.
162. MARMULLA, R., et al. Geometric accuracy of the NewTom 9000 cone beam CT. *Dentomaxillofacial Radiology*. 2005, 34(1), 28-31.
163. SHOKRI, Abbas, et al. Effect of exposure parameters of cone beam computed tomography on metal artifact reduction around the dental implants in various bone densities. *BMC medical imaging*. 2019, 19(1), 34.
164. SCARFE, William C., et al. Clinical applications of cone-beam computed tomography in dental practice. *Journal-Canadian Dental Association*. 2006, 72(1), 75-80.
165. CHANG, Yu-Bing, et al. 3D segmentation of maxilla in cone-beam computed tomography imaging using base invariant wavelet active shape model on customized two-manifold topology. *Journal of X-ray science and technology*. 2013, 21(2), 251-282.
166. XI, Tong, et al. A novel region-growing based semi-automatic segmentation protocol for three-dimensional condylar reconstruction using cone beam computed tomography (CBCT). *PloS One*. 2014, 9(11), e111126.
167. DESCOTEAUX, Maxime, et al. Bone enhancement filtering: application to sinus bone segmentation and simulation of pituitary surgery. *Computer aided surgery*. 2006, 11(5), 247-255.
168. CHUANG, Ying Ji, et al. A novel registration-based semi-automatic mandible segmentation pipeline using computed tomography images to study mandibular development. *Journal of computer assisted tomography*. 2018, 42(2), 306-316.
169. WALLNER, Jürgen, et al. A review on multiplatform evaluations of semi-automatic open-source based image segmentation for cranio-maxillofacial surgery. *Computer methods and programs in biomedicine*. 2019, 182 (2019): 105102.